Optical Properties of $CdTe/Cd_{1-x}Zn_xTe$ Strained-Layer Single Quantum Wells

A Disertation Presented to

The Faculty of the College of Engineering and Technology

Ohio University

In Partial Fulfillment

of the Requirements for the Degree

Doctor of Philosophy

By

Tiesheng Li

March 1993

ACKNOWLEDGEMENTS

I am truly grateful to my advisor Dr. Henryk J. Lozykowski for his resourceful guidance, active involvement and constant encouragement in every stage of this study. My sincere gratitude extends to Dr. H. C. Chen, Dr. R. A. Curtis, Dr. M. Celenk and Dr. S. Ulloa for their perusal and criticism, valuable suggestions and encouraging remarks on my dissertation.

Special thanks go to Dr. John L. Reno of Sandia National Laboratories, who grew the CdTe/$Cd_{1-x}Zn_xTe$ strained-layer single quantum well samples for this study. This study research was partially supported by Ohio University CMSS program, OU ECE Stocker Fund, and OU Baker Fund.

I wish to thank Mr. Ziad I. Al-Akir for his technical assistance in preparing the drawings in this dissertation. Last but not least, I am deeply indebted to my family, whose love, understanding, and support have been a great source of motivation and encouragement.

To my grandparents Hanqiao Li and Shuhe Gao

CONTENTS

Chapter One

Introduction

Research on a synthetically modulated semiconductor structure was initiated with a proposal in 1969-1970 by Esaki and Tsu [1,2]. The scope as well as the depth of the research in this field was further stimulated by the possibility of novel physics and applications in new types of electronic devices [3,4,5], such as Bloch oscillator, modulation-doped field effect transistor, hetero junction bipolar transistor and quantum well laser diode etc. In 1974 two basic experiments were carried out: Esaki and Chang reported the oscillatory behavior of the perpendicular differential conductance due to resonant electron tunneling across potential barriers[6], and Dingle's optical measurement showed directly quantization of energy levels of electrons in quantum wells, the well known elementary example of quantization in quantum mechanics text books [7]. Studies of layered semiconductor structure have then proliferated at explosive rate.

The semiclassical equations of free motion for electrons in an energy band E(**k**) with a electric field **F** are [111]

$$V(k)=\frac{1}{\hbar}\frac{\partial E(\kappa)}{\partial k}; \qquad \hbar\frac{dk}{dt}=-eF \tag{1}$$

where **k** and **V(k)** are electron's wave vector and group velocity respectively. In a steady electric field, electron's wave vector **k**(t) is given by

$$k(t)=k(0)-\frac{eFt}{\hbar} \qquad (2)$$

For electrons in the band E(**k**), **k** therefore changes linearly with time. The energy of the electron also changes according to the dispersion curve E(**k**), and so does **V(k)**. In the reduced Brillouin zone scheme, once the electron reaches a zone boundary point $\mathbf{k}_{ZB}$, it is Bragg reflected in the opposite direction; i.e., it appears at the $-\mathbf{k}_{ZB}$ point. Thus **V(k)** is an oscillatory function of time with a period equal to the time needed for **k** to cross the Brillouin zone, $T=(2\pi/d)(eF/h)^{-1}$, where d is the lattice periodicity. The motion in real space should also be oscillatory with the same frequency, which implies that the so called Bloch oscillator could be achieved. However, the period T has to be shorter than the collision time, which is impossible in bulk semiconductor materials where d is an atomic lattice constant (for F=10kV/cm, d=3.5Å, $T\approx 10^{-11}$s), but should be possible in a superlattice with a 10 to 50 times larger d.

In digital and microwave circuit applications the most common figures of merit are the propagation delay time τ_d and the current-gain cut-off frequency f_T. In both circuit applications, one would like to have a transistor that is capable of carrying large currents. To boost the device performance one seeks the perfection of materials and structures in which charge carriers have long life times, low scattering rates, high mobilities, and

controlled densities. In conventional device structures in which carriers are introduced by incorporation of impurities, however, improvement of life times and mobilities is generally limited by the scattering from impurities necessarily incorporated in order for carriers to be present. The technique of modulation doping of semiconductor hetero-structures provides a means of creating conducting channel with high carrier concentration but low impurity content. In modulation-doped semiconductor hetero-structures carriers are influenced by both the potentials created by transfer of charge and the potentials produced by band offsets of dissimilar semiconductor layers. As shown in Figure 1, electrons tend to move to layers of greater electron affinity. Electron mobility in the conventional GaAs MESFET channel with typical donor concentration of $\sim 10^{17}/cm^3$ ranges from 4000 to 5000 $cm^2/v \cdot s$ at room temperature. In undoped GaAs, electron mobility ranges $2 \sim 3x10^5$ $cm^2/v \cdot s$. The spatial separation of dopant impurity atoms from mobile electrons in a modulation-doped field effect transistor (MODFET) substantially reduces the ionized impurity scattering, which significantly increases the two dimensional mobility.

A quantum well laser diode (QWLD) is a double-heterostructure laser diode (DHLD) whose active layer includes a quantum well structure, in contrast to a conventional DHLD whose active layer is so thick (more than 500Å) that no quantum size effect is expected. The two dimensional nature of electron motion in quantum well heterostructure produces several unique and important features in QWLDs. First, the energy levels confined in a quantum well are functions of well width (this will be shown

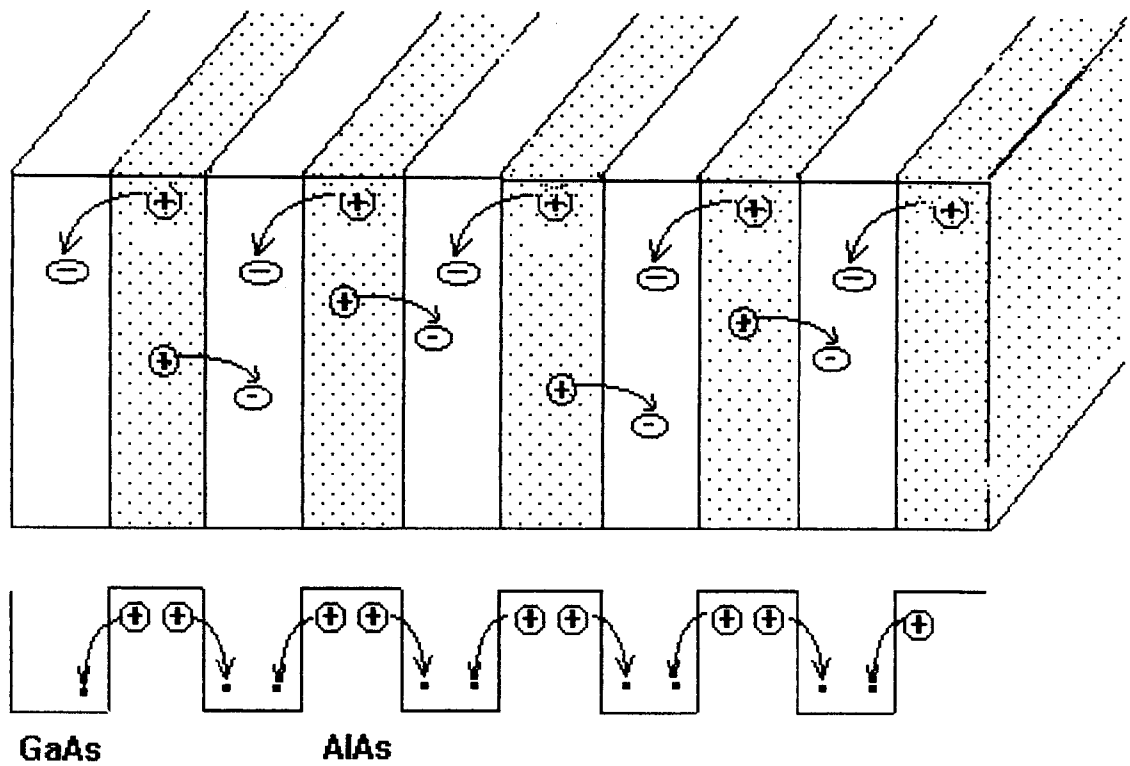

Figure.1. Spatial separation of electrons from ionized impuriy centers in a modulation-doped structure

in Chapter 4 and 5 by both theoretical and experimental results). Therefore, one advantage of QWLDs over conventional DHLDs is that the emission wavelength can be varied by simply varying the width of the quantum wells which form the active region. Second, due to the reduced dimensionality of free electron motion from three dimension to two dimension, the density of states as a function of energy is modified from a parabolic shape, as in conventional DHLDs, to the staircase shape (Figure 2 (a)) in QWLDs. As a result, the injected carrier distribution in energy and hence the gain spectra in QWLDs are different from the one in conventional DHLDs (Figure 2 (b), (c)). Even though one can always find an energy level for which the density of state of three dimensional system is equal to that of two dimensional system, the significant difference between the two dimensional and three dimensional systems should not be overlooked. The important point here is that the density of states is *finite* even at the bottom of two dimensional levels, whereas it tends towards zero in three dimensional system. This means that the gain remain *finite* at the bottom of two dimensional levels (Figure 2 (c)). Consequently, QWLDs exhibit threshold current density (J_{th}s) three times lower than the conventional DHLDs. The staircase shaped density of state makes the energy distribution of carriers less temperature sensitive. Therefore, QWLDs have higher T_0 [$T_0 \approx 160 \sim 180$ °K in expression $J_{th}=J_0\exp(T/T_0)$] than conventional DHLDs ($T_0 \approx 60$ °K).

The synthetically layered semiconductor structures offered a possibility of tailoring of association of materials in order to custom design the structure for some desired properties unattainable in homostructure. But before the advent of sophisticated

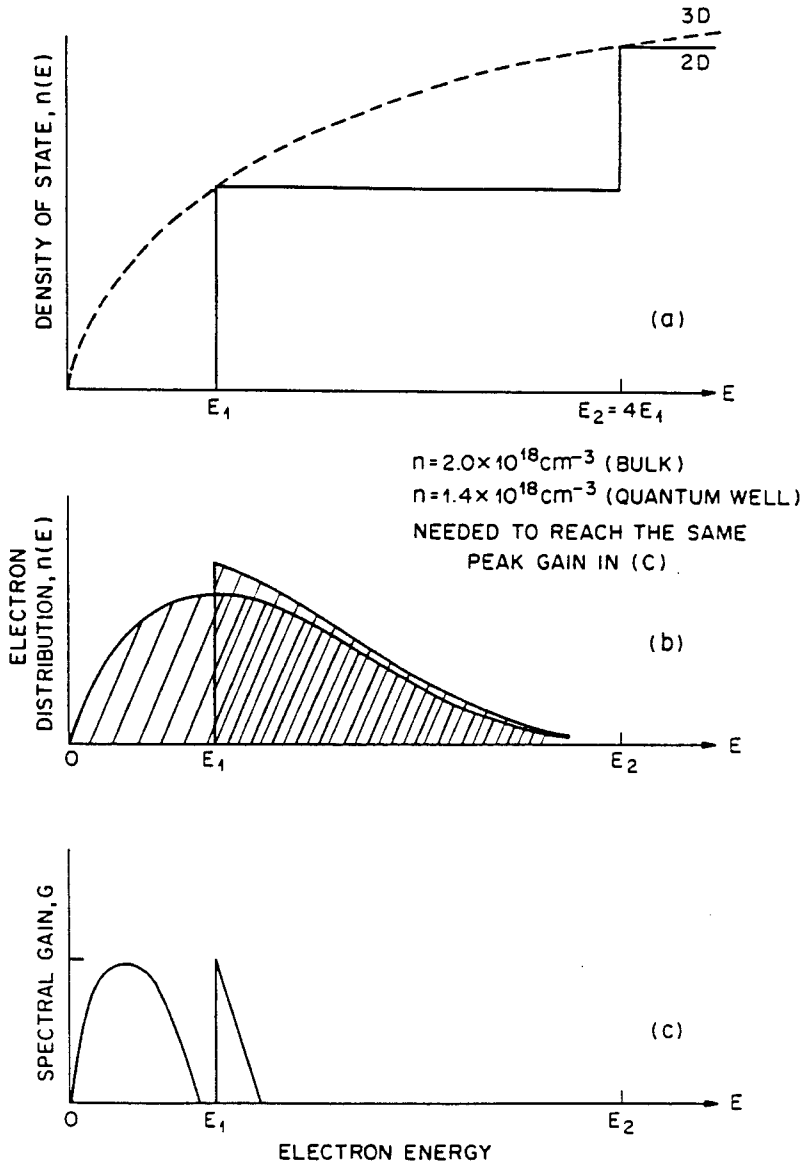

Figure.2. (a) Schematic diagrams of the density of states for bulk material and QW hetero-structures. (b) The distribution of injected carriers in bulk and QW structure needed to achieve the same peak gain spectra as shown in (c).

growth techniques such as MBE and MOCVD, most of work involving these thin-layered structures, called superlattice or quantum well, has been limited to closely lattice matched system; i.e. layered materials with lattice constants that are equal to about a tenth of a percent (for example, GaAs/AlGaAs). Recently, with the development of very well controlled MBE and MOCVD growth techniques, it is realized that interesting and useful quantum wells and superlattices can also be grown from a much larger set of material that has lattice mismatch in the percent range. This is schematically illustrated in Figure 3. This broader class of new layered semiconductor structures, called strained layer superlattice (SLSs), and strained layer quantum well (SLQW), provide a wealth of properties which allow us to study material physics and design devices.

To realize the alternated layer structure, Esaki and Tsu proposed two ideas: a) To use a single material but to dope it alternatively, n & p type. This idea was extensively developed by Dölher, Ploog and collaborators [6] and now is refereed to as "ni-pi superlattice". b) To alternate layers of material with different composition (for example, GaAs/AlGaAs, ZnSe/$Zn_{1-x}Cd_xSe$ and CdTe/$Cd_{1-x}Zn_xTe$), refereed to as compositionally modulated superlattice or quantum well. The combination of a) and b) gives the so called composition-doped structure. A variety of different growth techniques has been used to crystallize semiconductor heterostructure. **M**olecular-**B**eam **E**pitaxy (MBE) and **M**etalorganic **C**hemical **V**apor **D**eposit (MOCVD) are the two techniques best adapted for satisfying the stringent requirements of these multi-layer structures.

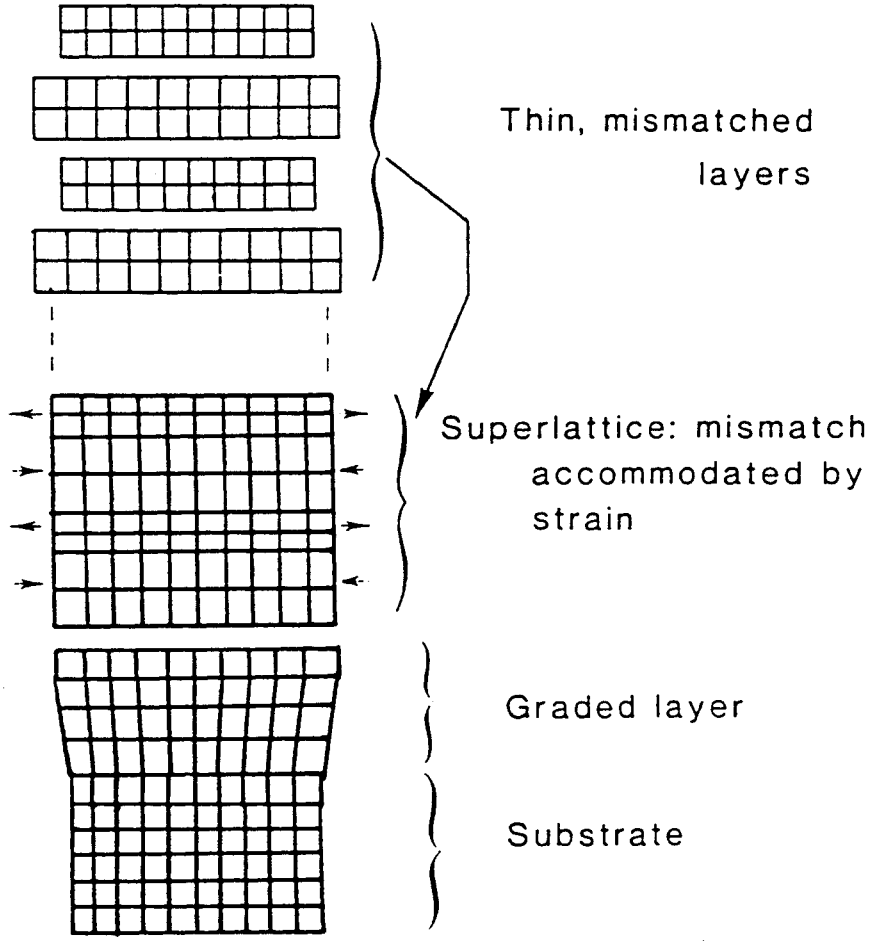

Figure.3. Schematic illustration of biaxially strained layers in an strained-layer superlattice structure. The graded layer (buffer) and the substrate are also shown.

In MBE, thin films of semiconductors, metals or insulators crystalize via chemical reactions between thermal energy molecular or atomic beams of the constituent elements (or gaseous reactants containing constituent elements) and substrate surface which is maintained at an elevated temperature in ultrahigh vacuum (UHV). The growth rate of typically 1 μm/h (1 monolayer/s) is low enough that surface migration of the impinging species on the growing surface is ensured. Consequently, the surface of the grown film is very smooth (on the macroscopic scale). Shutters are used in front of sources to interrupt the beam fluxes; i.e. to start or to stop the deposition and/ or doping. Changes in composition and doping can thus be abrupt on an atomic scale.

MOCVD is based on the thermal deposition of gaseous mixtures of alkyls and/ or hydrides. The constituent elements of the films to be grown are introduced under atmospheric-pressure (in the case of AP MOCVD) or at a pressure lowered to about 10^3 Pa (in the case of LP MOCVD) into the growth reactor in the form of gaseous reactants(for example, trimethylgallium and arsine in the case of GaAs) where they undergo thermal decomposition (pyrolysis) on the hot substrate crystal. The growth process results from chemical reactions between the constituent elements which occur on the heated substrate or in the chemical boundary layers at the substrate.

This research focuses only on compositionally modulated structures. A literature review is given in Chapter Two. Chapter Three outlines the scope of this dissertation. Theoretical calculations are derived in detail in Chapter Four. The experimental

apparatus setup, procedure and results are discussed in Chapter Five. And finally Chapter Six gives the summry and proposal for further research.

In the theoretical part of this study, a detailed interpolation scheme is derived to calculate the strain and bowing effects on each individual band edge instead of the overall band gap, which is very crucial in predicting the correct band lineups. A three-band Kane model describing biaxially strained materials is derived. This model is incorporated into the three-band envelope function approach to calculate the allowed energy states for carriers in strained-layer heterostructures. The confined energy levels and the transition energies in CdTe/$Cd_{0.79}Zn_{0.21}Te$ strained-layer single quantum wells are calculated.

In the experimental part of this study, a new digital technique for optical polarization measurement is presented. Photoluminescence (PL) measurement at different temperatures, PL excitation spectra, and circular polarization measurement are performed on CdTe/$Cd_{0.79}Zn_{0.21}Te$ strained-layer single quantum wells. A free exciton state and an exciton state bound to neutral acceptors are identified. Binding energies of free excitons are estimated from the difference between the calculated optical gap and the observed exciton transition energy. A broad band is identified as related to the defects states at the interface between the buffer layer and substrate. The broadening mechanism is shown to be dominated by interaction between the excitons and the polar optical phonons. The band lineup configuration is confirmed to be type I for heavy hole and type II for light hole. The LO phonon energy in the well is estimated from PL excitation spectra.

Chapter Two

Overview

§ 2-1 Theoretical works

Electronic-structure theory has a unique role to play in superlattice (quantum well) research because of the rich variety of possible material systems. Theory can be used to invent structures that exhibit new physical phenomena. In some cases these phenomena may have technical applications. Theory can also be used to tailor superlattice (quantum well) electronic structures to either to enhance the observation of particular effect or to optimize the material structure for a technical purpose. There is an essential difference between the role of electronic structure theory in superlattice (quantum well) research and its counterpart in conventional semiconductor material studies. For conventional semiconductor material studies, theory can be used to describe the electronic structures and to interpret experimental results that depend on electronic structure. There are, however, few parameters available with which to design new materials. The large number of potential superlattice (quantum well) system allow great freedom in material design. Theory has a very important part to play in this designing process.

Energy offsets between corresponding bands in constituent materials of a superlattice (quantum well) system are typically on the order of a few hundred meV. Modifications in the electronic structure due to these offsets are on the same energy scale, a few hundred meV. Thus a theoretical description of the electronic structure in such a system must deal with questions on this energy scale. Those electronic states in which the electrons' mean free paths are comparable to or longer than the thickness of constituent material layers are significantly influenced by the spatial modulation of the structure. Therefore, electronic states relatively close in energy to band edges, in which electrons have relatively longer life time and mean free path, are of great interest in superlattice (quantum well). As a result, theories of electronic structures in superlattice (quantum well) are band-edge theories in which one cares about a detailed description of band edges. Perturbations such as the spin-orbit interaction, strain, and electric field are very influential on the energy scale of interest. These considerations are important in choosing a theoretical approach for the electronic structure in superlattices (quantum wells). For example, a theory that neglected spin-orbit interaction could not be expected to give a meaningful description of superlattice (quantum well) valence states on the energy scale of interest.

A very wide range of theoretical techniques have been applied to superlattice (quantum well) electronic structure calculations. The degree of complexity ranges from scaled Kronig-Penney models to self-consistent many-electron calculations. Which theoretical approach is most appropriate depends on the material system studied and the

question asked about that system. For example, the GaAs/$Al_xGa_{1-x}As$ systems are relatively easier to describe theoretically if we care only about the electronic states in the conduction band. Both constituent materials have direct band gaps; they are relatively wide-band-gap semiconductors; the band lineups are type I; and the constituent materials are closely lattice-matched. As a result of these simplifying features, there is little mixing constituent material bands with different bulk symmetry in the superlattice (quantum well) wave functions, and Kronig-Penney model scaled by appropriate effective mass and with barrier height given by the band offsets will provide a fairly good zone-center energy levels. For more complex material system (for instance, small gap materials or type II lineups, in which band mixing can be significant) or more complex questions asked (for example, detailed dispersion relations in the whole Brillouin zone), more sophisticated theoretical treatment become necessary.

1 Supercell Approach

Except for the Kronig-Penney type models, the first superlattice electronic structure calculations were carried in supercell approaches. The primary advantage of these approaches is their straightforward concept. A principal disadvantage of these approaches is that the dimension of matrices that has to be diagonalized increase rapidly with the thickness of superlattice period. Therefore, they are limited to rather thin layered superlattices. Many researchers have explored empirical pseudopotential and tight-binding models using supercell approaches.

Empirical pseudopotential calculations were performed on thin-layer GaAs/ $Al_xGa_{1-x}As$ superlattices using the supercell approach by Carruthers and Lin-Chung [8,9,10] and Adreoni, Baldereschi, and Car [11]. In both calculations, screened atomic pseudopotentials were expressed as form factors, which were empirically determined, and wave functions were expanded in terms of plane waves. The number of plane waves increases linearly with the thickness of superlattice period. Carruthers and Lin-Chung used about 190 plane waves for a superlattice consisting of one layer each of GaAs and AlAs. Because of the rapid increase in computing cost, they went up only to the superlattice with three molecular layers of each constituent material.

Tight-binding calculations were performed on $GaAs/Al_xGa_{1-x}As$ superlattices by Schulman and McGill [12,13]; on InAs/GaSb superlattices by Nucho and Madhukar [14], Madhukar, Dandekar and Nucho [15], and Madhukar and Nucho [16]; on CdTe/HgTe superlattice by Schulman and McGill [17,18,19]; on Si/GaP superlattice by Madhukar and Delgado [20]; and on $GaAs/GaAs_{1-x}P_x$ superlattice by Osbourn [21,22] using supercell approach. In these calculations, a tight-binding basis, typically one s-type function and three p-type functions centered at each atom, was chosen, and Hamiltonian matrix elements between these functions were parametrized. The basis functions were usually taken to be orthonormal and matrix elements out to second-nearest neighbors were included. The tight-binding parameters are typically fixed by fitting to a bulk band structure.

After the superlattice tight-binding models have been specified by these parameters, the Hamiltonian matrix is constructed [23]. If spin-orbit interaction is ignored, the dimension of the Hamiltonian matrix is (M+N)n, where M and N are the number of molecular layers of each of two constituent materials in the superlattice period and n is the number of the basis functions, typically eight, in a bulk unit cell. If spin-orbit interaction is included, the dimension of Hamiltonian is doubled. Again, due to the fact that the dimension of the Hamiltonian gets very large for thick-period superlattices, this approach has been restricted to period of about 20 molecular layers or less.

2 Boundary-Condition Approaches

The superlattice electronic-structure problem has a number of simplifying features. One usually cares only about results in a small energy region near the band edges; the electronic structure of the bulk constituent materials is well understood; the size of perturbing superlattice potential is not large on the scale of bonding and antibonding bandwidths. The supercell approach has not taken advantage of these simplifying features. They lead to large-dimensional Hamiltonians that describe a much larger energy region than is of interest. A great deal of computer time is required to diagonalize these large-dimensional matrices. Only a small fraction of eigenvalues and eigenfunctions are of any interest.

Boundary-condition approaches attempt to take advantage of the simplifying features of the problem. In these approaches, eigenfunctions of the constituent materials are matched at the superlattice interfaces to construct a superlattice eigenfunction. They generally lead a Hamiltonian matrix with a smaller dimensionality than those in the supercell approaches. The Hamiltonian matrices in boundary-condition approaches generally do not increase in dimension with increasing superlattice period, which is the principal advantage of this approach.

Tight-binding calculations using a boundary-condition approach have been applied to superlattice electronic-structure calculations by Schulman and Chang [24,25]. The complex band structure is calculated using a transfer matrix method [26,27]. The Bloch and evanescent states in the constituent materials are used to construct a reduced Hamiltonian. This Hamiltonian matrix is diagonalized for a given superlattice wave vector to determine the corresponding energy eigenvalue and wave function. The basis set, constituent-material Bloch and evanescent states, is energy dependent. For consistency, the scheme is to be iterated until the output and input energy agree. Spin-orbit interaction and strain have been included [25,28]. The dimension of the matrix that must be diagonalized is independent of superlattice period and is of modest size. For the Four-orbital-atom and second-nearest-neighbor tight-binding model (including spin-orbit interaction), 64x64 matrices are required to describe a $<001>$ interface. The approach has several advantages: it has modest matrix size that does not depend on superlattice period; it has the ability to treat spin-orbit and strain interactions; it can be adapted to

optical calculations. The disadvantages of this approach are of those common to tight-binding methods: a large number of input parameters are required; the relation between various input parameters and the result is complex; the bulk tight-binding parameters are not uniquely specified by the bulk energy band structure; and the bulk conduction-band dispersion is usually too flat.

As mentioned before, it is the band-edge states of superlattices that are of primary interest. In bulk semiconductors, **k·p** theory is exceptionally effective at describing states near the conduction- and valence-band edges [29,30,31]. So it is natural to consider **k·p** method to describe these states in superlattices (quantum well). First theoretical efforts to describe electronic structure in superlattices were based on Kronig-Penney models scaled by bulk effective masses with barrier height given by the energy band offsets [32,33]. Because the effective-mass picture is based on **k·p** theory, the scaled Kronig-Penney models can be viewed as a simple **k·p** method. Modifications of the scaled Kronig-Penney model, within a one-band framework, to include nonparabolicity were made by Mukherji and Nag [34].

The scaled Kronig-Penney models do not include coupling between different bulk bands by the superlattice potential. In type-I superlattice made from relatively wide-band-gap constituent materials, such as GaAs/$Al_xGa_{1-x}As$, these models can give zone center energies fairly well. They are not appropriate for superlattice in which there is extensive band mixing, such as type-II superlattice InAs/GaSb. A two-band model, which can

account for coupling between conduction- and valence-band (light hole) was developed by Bastard [35,36] and White and Sham [37]. This model, which is usually refereed to as the two-band envelope-function model, has had considerable success in predicting zone-center energies and has been used extensively for interpreting experimental data. This model can be derived by writing the superlattice wave function as a sum of products of zone-center Bloch functions in each constituent material and slowly varying envelope functions. The Bloch functions in constituent materials are known from bulk calculations. Coupled equations for the envelope functions are found from bulk $\mathbf{k}\cdot\mathbf{p}$ equations and boundary conditions at interfaces. The envelope-function model obtained this way is capable of describing the dispersion relation along the superlattice growth direction. When deriving the two-band envelope- function model Bastard et al. took k_z along the superlattice growth axis and forced $\mathbf{k}_{\pm}=\mathbf{k}_x\pm\mathbf{k}_y=0$. Therefore this model can not describe dispersion relation for a wave vector normal to the superlattice growth axis. By letting $\mathbf{k}_{\pm}=0$, the heavy-hole band is decoupled in the Kane matrix [38] and can only be treated in a one- band model. The $\mathbf{k}\cdot\mathbf{p}$ interaction from remote bands are partially restored for the heavy-hole band in Löwdin perturbation theory [39]. The spin-orbit splittings are assumed to be very large and the split-off band is neglected. The envelope-function method has been generalized by Altarelli and co-workers [40,41]. In this multi-band model, the split-off band is also neglected. It is capable calculating dispersion relation in any direction and, of course, the resulting coupled equations for the envelope functions in this model are more complicated than in the two-band model. These

equations are usually solved approximately by variational methods. Dimension of the matrix Alterili used is 72x72. It has been used for optical properties calculations [42,43].

Smith and Mailhiot [44,45] have developed a **k·p** theory of superlattices in which a reference Hamiltonian was defined by averaging the bulk pseudopotentials of the constituent materials. Zone-center eigenenergies and eigenstates were found for this reference Hamiltonian, which formed a common basis set for the two constituent materials. The Γ_{15} valence states and Γ_1 conduction states were coupled and treated explicitly. Other **k·p** terms and the difference between the material pseudopotentials and the reference Hamiltonian pseudopotential were treated as perturbations. The resulting eigenequation involved matrices whose dimension did not depend on the superlattice period and was rather small (16x16 or 12x12). This **k·p** theory has been used to calculate superlattice electronic structure [45] and optical properties [46].

The **k·p** approaches are the most frequently used models for superlattice electronic structure. They are relatively simple and easy to implement. The number of input parameters, which are usually well known, is quite small and the dependence of the results on these input parameters is fairly direct and easy to understand on a physical basis.

3 Ab initio Methods

All the theoretical approaches discussed in group 1 and 2 above used empirical methods in which the parameters of bulk model are assumed not to change when constituent materials are combined to form the superlattice (quantum well). To date, most theoretical information on superlattices has been obtained through empirical methods. Since all empirical methods are based on a knowledge of the bulk electronic structure of the constituent materials, they become somewhat questionable when dealing with extremely-thin-layer or heavily strained superlattices (quantum wells). A few *ab initio* pseudopotentials have been used to for superlattice-geometry studies of interfaces [47,48,49]. These calculations concentrated on valence-band offsets and stability conditions for very-thin-layer superlattice. The *ab initio* methods are much more complex and expensive to implement than empirical methods. So far, *ab initio* methods have been restricted to ground-state-interface studies and electronic-structure studies of very-thin-layer superlattices. The ground-state-interface studies are particularly useful in giving information on valence-band offsets. This information can be usefully applied in empirical electronic-structure calculations. *Ab initio* electronic-structure calculations on heavily strained Si/Ge superlattices [50] have suggested that empirical methods can adequately describe such systems though it is not initially obvious that this was the case.

§ 2-2 Experimental works

1 Crystal Growth and Characterization

The techniques of metal-organic chemical vapor deposition (MOCVD) and molecular-beam epitaxy (MBE) are the two most favorite procedures to fabricate strained-layer superlattice (quantum well) because of their demonstrated capability for growing very thin (<50 Å) layers. Both techniques are capable of producing abrupt interfaces and layers which are uniform in composition and thickness and contain few defects. Abrupt doping (including δ-doping) can also be obtained using these techniques. Due to the attractive features offered by superlattices (quantum wells), tremendous amount of superlattices (quantum wells) has been grown all over the world. The number of papers published is countless, or at least, beyond the scope of this dissertation to review. The important work I have to mention here is the strained-layer supperlattices (quantum wells) involving ZnSe, CdSe, $Zn_{1-x}Cd_xSe$ and $Cd_{1-x}Mn_xSe$ grown by N.Samarth and co-workers [51]. In bulk, both CdSe and $Cd_{1-x}Mn_xSe$ crystallize exclusively in the *wurtzite* structure. For the first time, N.Samarth and co-workers have grown ZnSe/$Zn_{1-x}Cd_xSe$ and ZnSe/Cd_{1-x} Mn_xSe systems in which lattice mismatch is accommodated by strain and, more importantly, $Zn_{1-x}Cd_xSe$ and $Cd_{1-x}Mn_xSe$ crystallize in *zinc-blend* structure. This has opened the door to new flexibility for sample designing and at same time proposed new studies in this field. The growing surfaces were monitored by reflection high energy electron diffraction (RHEED) at 10 keV. The RHEED signal from

a growing wafer changes its intensity in oscillatory manner due to recurrent atomic patterns in the layer-after-layer growth mode. The period of the oscillation is exactly equal to the growth of one monolayer. This phenomenon is used not only for *in-situ* measurements of accurate growth rate but also for accurate timing to open and close the effusion cell shutters according to the design of the sample structure.

After the samples were withdrawn from MBE system, both transmission electron microscopy (TEM) and x-ray diffraction were used for characterization. TME, requires the tedious procedure of sample thinning for a cross-section view, offers very good resolution and is capable of providing information about crystal perfection (presence of defects). X-ray diffraction is more frequently used because it is non-destructive and convenient. In the X-ray diffraction pattern, many diffraction peaks appear, one being from the substrate and others being the fundamental and the higher order diffractions from the superlattice layer. If scanned in general direction in reciprocal space, analysis of the positions, line shapes and intensities of the Bragg reflections yields information such as average lattice constants, composition and strain wave profile.

Photoluminescence (PL) measurement is also non-destructive and can be used to gain more insight into the smoothness of the hetero-interface between a quantum well layer and a barrier layer. Consider the electronic energy levels in a very deep rectangular shaped potential well:

$$E_n = \left[\frac{\hbar^2\pi^2}{2m_e^*}\right]\left[\frac{n}{L_z}\right]^2 \quad (3)$$

where n=1, 2, 3, ..., is index number of confined energy levels and L_z is the width of the quantum well. From equation (3) one can see that an uncertainty ΔL_z in the width of the quantum well will cause an uncertainty ΔE_1 in the energy of n=1 level:

$$\Delta E_1 = -\Delta L_z\left[\frac{\hbar^2\pi^2}{m_e^* L_z^3}\right] \quad (4)$$

If one assumes now that the positions of the hetero-inter-face in the z direction vary statistically along x and y, the distribution of well widths is statistical and can be described by a Gaussian distribution. Thus, there is no longer one single sharp n=1 energy level but a Gaussian distribution according to equation (4). The photon energy of the n=1 heavy hole exciton recombination is

$$E_{(e,hh)1} = h\nu = E_g^w(3D) + E_{el} + E_{hhl} - E_x(2D) \quad (5)$$

Where E_g^w(3D) is three dimensional band gap of well layer material, E_{e1} and E_{hh1} are the n=1 energy levels of electron and heavy hole respectively, E_x(2D) is the binding energy of the 2D exciton. Since E_x(2D) is typically of the order of 1% of the band gap, its broadening due to a distribution of well widths can be neglected in a first approximation. At low temperature and low excitation intensity the exciton density of states is occupied

over an energy range much smaller than the magnitude of the energy uncertainties given by equation (4) and the line shape of exciton recombination will have a Gaussian character. The half width of the recombination line is related to the half-width of the L_z distribution via

$$\Delta L_z = \Delta h\nu \left(\frac{\mu L_z^3}{\hbar^2 \pi^2} \right) \tag{6}$$

where μ is the reduced mass of the exciton.

Recently, there are reports on characterization of superlattice (quantum well) by scanning tunneling nanoscope (STN) and the associated luminescence [52].

2 *Electronic Properties*

The two major probing for electronic properties in semiconductors are transport measurement and optical measurement. For better resolution, the electron system can be further quantized in a strong magnetic field, which leads us to magneto-transport and magneto-optical measurement. While transport measurements usually deal with electrons because of their high mobilities, optical measurements provide a means to study transition involving states in both the conduction band and valence bands. GaAs/$Al_{1-x}Ga_xAs$ and InAs/GaSb are the two superlattice systems most extensively studied by transport and

magneto-transport measurement. S.E.Ulloa and J.Zhang have developed a model [53,54] which thoroughly explains the magneto-transport experiment in superlattice systems.

That luminescence properties bear directly on lasers has provided a strong stimulus for their extensive investigation. The phenomenon of luminescence, i.e., the emission of light by excited atoms, molecules, or condensed matter, is caused by radiative transitions between energy levels of excited species and is characteristics of the species for its close relation to the structure of energy levels of this species. Each feature of the luminescence spectrum of the physical system is connected with a definite electronic transition which originates on some excited electronic energy level, and after the emission of a photon (one single or multiple phonon may be involved) terminates when the electron reaches a lower energy level. Depending on the way in which the excited levels become populated, i.e., on how the physical system becomes energetically excited, different luminescence processes may occur. If the physical system is excited with electromagnetic radiation, photoluminescence (PL) occurs. When the physical system is excited by applying an electric field (a voltage) to the system, electroluminescence (EL) results. X-ray luminescence is excited by X-ray radiations while cathodo-luminescence (CL) is excited by bombardment with energetic electrons.

In semiconductors, luminescence is caused by radiative recombination of individual or coupled charge carriers. These may be: (1) free electrons or holes

occupying energy levels in the conduction and valence bands respectively, (2) electrons or holes bound to ionized impurities, and (3) excitons (electrons-hole pairs coupled by Coulomb interaction) which can move throughout the crystal lattice of the semiconductor (free excitons), or become localized by interaction with an active point defect of the lattice or an impurity center (bound excitons). Luminescence spectroscopy has the advantage of the ability to discriminate between species involved in different recombination processes and can provide simultaneous information on many types of centers in the crystal lattice. It is, therefore, capable of providing a great deal of information about electronic processes in semiconductor hetero-structure.

In searching for application candidates in visible range, more and more photoluminescence studies have been done on II-VI compound strained-layer superlattices (quantum wells). ZnTe/CdTe systems were studied by R.H.Miles [55]; ZnSe/ZnS by Yochi [56]; $Cd_{1-x}Mn_xTe$/ CdTe by J.Warnock [57]; $ZnSe/ZnS_xSe_{1-x}$ by K.Shahzad [58] and K.Mohammed [59]; and ZnTe/ZnSe by M.Averous et al [60]. These II-VI compound heterostructures are considered promising for the applications in the field of integrated optics and optical computing systems [60].

Chapter Three

Proposed Study

§ 3-1 Calculation

Theoretical task of proposed study is to extend Bastard's *envelope-function model* to include the spin-orbit and strain interactions. To implement this calculation for ZnSe/$Zn_{1-x}Cd_xSe$ and $Cd_{1-x}Zn_xTe$/CdTe systems (which will be studied experimentally in this research), the following problems are to be solved:

1. CdSe in bulk form, as mentioned before, crystallizes exclusively in the wurtzite structure. So all the available experimental data on bulk CdSe are from wurtzite structure CdSe. But in the SLS studied in this research $Zn_{1-x}Cd_xSe$ is in the zinc-blend structure. All the bulk parameters needed (band structure at Γ point, elastic constant tensor elements, etc.) must be transformed from what is available into the one for zinc-blend structure CdSe.

2. The parameters for $Cd_xZn_{1-x}Te$ and $Zn_{1-x}Cd_xSe$ in zinc-blend structure are to be interpolated. To get a more precise band offsets between different layers (band lineups), bowing effects on each individual band (conduction band and valence band), as well as

the bowing effect on the band gap are to be taken into account. This gives the band lineups before the effect of strain between different layers is considered.

3. Using deformation potential theory, strain effects on the energy bands in constituent materials are to be calculated and final band lineups will be set. Since we can experimentally determine only the energy difference between two energy bands, the deformation potential data (experimental) available so far are the relative deformation potential between conduction and valence bands. For conventional material study this might be good enough. For the proposed study here, however, the final band lineups can not be determined from these data. It is necessary to define the "absolute" or, at least relative to a common reference, deformation potentials for conduction band and valence band respectively. The "absolute" deformation potentials derived from model solid theory [61] is going to be used.

4. After the final band lineups are set, Bastard's procedure is to be followed without neglecting the spin-orbit split-off band to derive a three-band envelope function model, incorporating the strain effects. The $\mathbf{k}\cdot\mathbf{p}$ interaction from remote bands will be partially restored for heavy hole band in Löwdin's perturbation theory [39].

5. Computer programs implementing above calculations are to be written in FORTRAN language.

§ 3-2 Experiment

The strained-layer single quantum wells $Cd_{1-x}Zn_xTe/CdTe$ (x=0.21) grown by John Reno [81] will be experimentally studied in our laboratory by following means:

1. Photoluminescence (PL). PL is predominantly intrinsic in semiconductor quantum wells and its intensity reflects the quality of the samples because the quantum efficiency crucially depends on the samples quality. A PL spectrum provides information about radiative transitions between different electronic states. Temperature dependence of PL spectra reveals information about quenching and broadening mechanism.

2. PL excitation spectropy (PLE). PLE is done by setting the detecting device at a fixed wavelength while scaning the wavelength of excitation light. The straightforward PL spectra alone do not always give sufficient information on parameters of semiconductor heterostructure samples. PLE spectra are often required to be employed in a complementary fashion in order to gain more information on higher excited levels and the energy transferring process between these excited levels and the emitting level we are looking at. PLE spectra can also provide information on phonon assisted processes.

3. Combination of PL or PLE with circular polarization technique, ie. excite the sample with circularly polarized light and use circular polarization discrimination on the

detecting side. In the dipole approximation there is a correspondence between a quantum transition from state A to state B and a classical dipole with frequency $\omega = | (E_A - E_B)/\hbar |$ the amplitude of the dipole moment being equal to the transition matrix element

$$D_{AB} = \langle A | \hat{D} | B \rangle \tag{7}$$

where $\hat{\mathbf{D}}$ is the dipole moment operator. Intensity and polarization of light emitted or absorbed in quantum transitions are the same as for emission or absorption of light by the classical dipole. If we describe the Γ-point band structure by Kane model [see Chapter Four], keeping in mind that (1) the spin functions are normalized and orthogonal for different spin directions, and (2) the quasi-momentum is conserved in the transition, the only matrix elements not equal to zero are

$$\langle S | D_x | X \rangle = \langle S | D_y | Y \rangle = \langle S | D_z | Z \rangle \tag{8}$$

As shown in the next chapter, the band energies at Γ point ($\mathbf{k}=\mathbf{0}$) are diagonal in $| \mathbf{J}, m_J \rangle$ representation and are labeled as heavy hole, light hole, and spin-orbit split bands respectively. The matrix elements of the dipole moment in $| \mathbf{J}, m_J \rangle$ representation are listed in table 1. Selection rules shown in Figure 4 can be deduced from this table. From this polarization spectroscopy, or as often referred as optical pumping study, we can gain more insight into the electronic structure of the SLQW system due the selection rules.

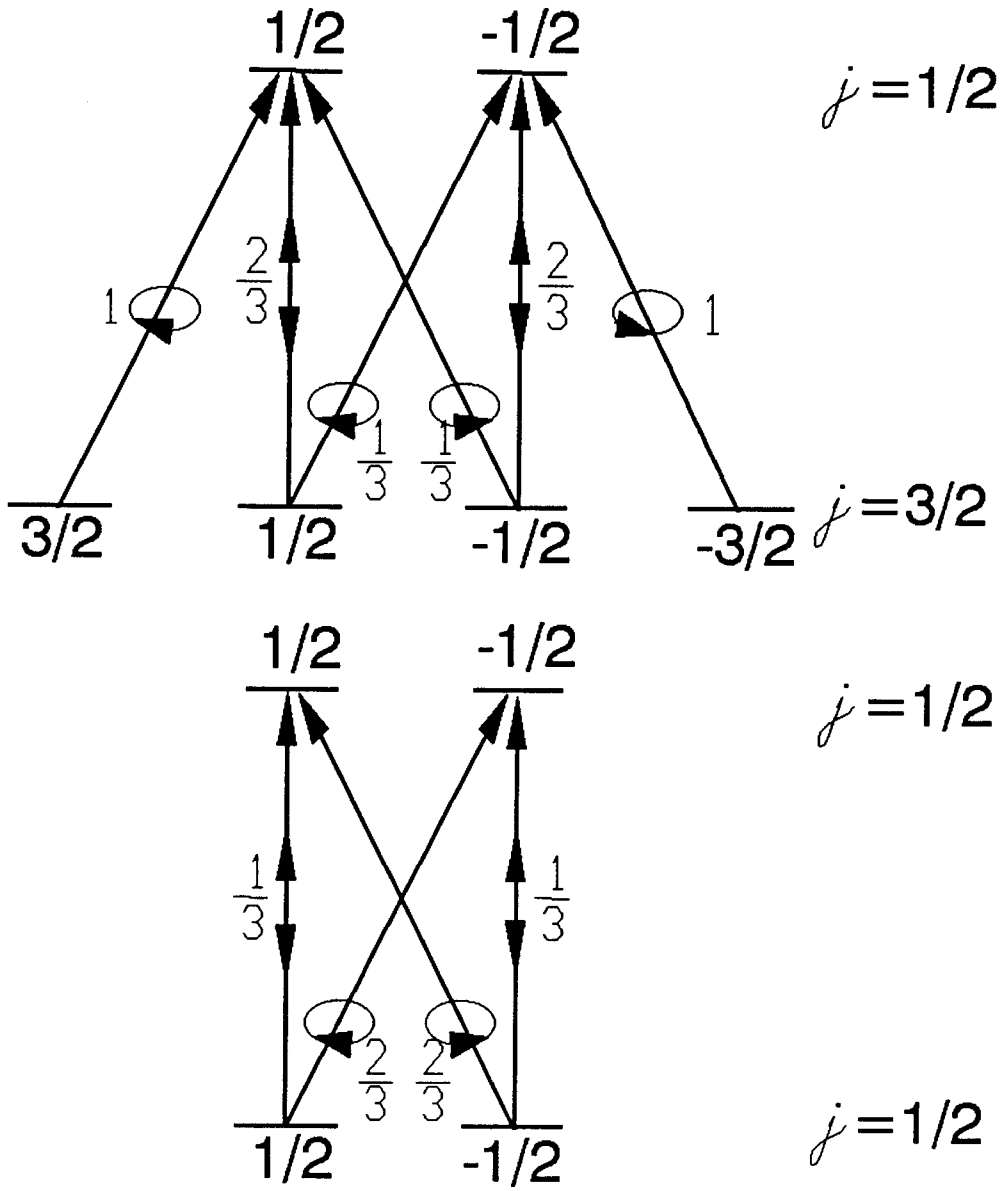

Figure. 4. Selection rules deduced from Table 1. The numbers near the arrows representing the dipoles indicate the relative transition intensities.

4. Time-Resolved-Spectropy (TRS). Using TRS technique we can learn about the kinetic processes in the electronic system, ie. energy transfer process and life time of different electronic states and excitons at certain temperature. The process of collecting the photogenerated carriers into the quantum well can also be studied by TRS technique.

Table 1. Matrix elements of dipole moment D_{vc}/D for different interband transitions*

Band	v	c	
		1/2	-1/2
heavy hole	+3/2	$-(1/2)^{1/2}(\mathbf{n}_1+i\mathbf{n}_2)$	0
	-3/2	0	$(1/2)^{1/2}(\mathbf{n}_1-i\mathbf{n}_2)$
light hole	+1/2	$(2/3)^{1/2}\mathbf{n}_3$	$-(1/6)^{1/2}(\mathbf{n}_1+i\mathbf{n}_2)$
	-1/2	$(1/6)^{1/2}(\mathbf{n}_1-i\mathbf{n}_2)$	$(2/3)^{1/2}\mathbf{n}_3$
s-o split	+1/2	$-(1/3)^{1/2}\mathbf{n}_3$	$-(1/3)^{1/2}(\mathbf{n}_1+i\mathbf{n}_2)$
	-1/2	$-(1/3)^{1/2}(\mathbf{n}_1-i\mathbf{n}_2)$	$(1/3)^{1/2}\mathbf{n}_3$

* $\mathbf{n}_1$ and $\mathbf{n}_2$ are unit vectors in a plane perpendicular to the momentum, $\mathbf{n}_3$ is a unit vector along the momentum. (from [86])

From the proposed study we will gain more understanding of the electronic structure and the optical properties of strained layer superlattices and single quantum wells, especially, ZnSe/$Zn_{1-x}Cd_xSe$ and $Cd_{1-x}Zn_xTe$/CdTe systems.

Chapter Four

Theory

§ 4-1 The **k·p** method

The so called **k·p** method was originally a device for exploring the properties of the energy bands and wave functions in the vicinity of some important point in **k** space with the aid of perturbation theory. Dresselhaus et al [61] established the importance of the **k·p** approach as a rigorous basis for the empirical determination of band structure. Coupled with the use of symmetry, the **k·p** method gives that the band structure in the vicinity of a point in **k** space depends on a small number of parameters (gaps and masses) which can be determined accurately by experiment.

Consider the one-electron problem of a electron moving in a periodic potential V(**r**). The Schrödinger Equation is

$$\hat{H}\psi=\left\{\frac{\hat{p}^2}{2m}+V(r)\right\}\psi=E\psi \qquad (9)$$

Bloch showed that Ψ may be written [62]

$$\psi = e^{ik\cdot r} u_{nk}(r) \tag{10}$$

where u_{nk}, the Bloch function, has the periodicity of $V(\mathbf{r})$ and $\mathbf{k}$ lies in the first Brillouin Zone and n is a band index running over a complete set of bands. Substituting (10) into equation (9), we have

$$\left\{ \frac{\hat{p}^2}{2m} + \frac{\hbar}{m} k\cdot\hat{p} + \frac{\hbar^2 k^2}{2m} + V(r) \right\} u_{nk}(r) = E_n(k) u_{nk}(r) \tag{11}$$

For any given $\mathbf{k}$, the set of all u_{nk} is complete for functions having the periodicity of $V(\mathbf{r})$. Therefore, any u_{nk} can be expressed in term of u_{nk0}, the wave function for $\mathbf{k}_0$

$$u_{nk}(r) = \sum_{n'} C_{n'n}(k-k_0) u_{n'k_0}(r) \tag{12}$$

We can call this $\mathbf{k}_0$ representation.

If we define $\hat{H}_{k0}$ to be

$$\hat{H}_{k_0} = \frac{\hat{p}^2}{2m} + \frac{\hbar}{m} k_0\cdot\hat{p} + \frac{\hbar^2 k_0^{\,2}}{2m} + V(r) \tag{13}$$

then we have

$$\hat{H}_{k_0} u_{nk_0} = E_n(k_0) u_{nk_0}(r) \tag{14}$$

$$\left\{\hat{H}_{k_0}+\frac{\hbar}{m}(k-k_0)\cdot\hat{p}+\frac{\hbar^2k^2}{2m}(k^2-k_0^2)\right\}u_{nk}(r)=E_n(k)u_{nk}(r) \tag{15}$$

As we have known that u_{nk}'s are orthogonal, equation (15) can be easily converted into a matrix eigenvalue equation by substituting equation (12) into equation (15), multiplying both sides by $u_{nk0}(\mathbf{r})$ [from left], and integrating over the unit cell in which u_{nk0}'s are normalized

$$\sum_{n'}\left\{\left[E_n(k_0)+\frac{\hbar^2k^2}{2m}(k^2-k_0^2)\right]\delta_{nn'}+\frac{\hbar}{m}(k-k_0)\cdot p_{nn'}\right\}C_{n'n}=E_n(k)C_{nn} \tag{16}$$

where

$$p_{nn'}=\int_{cell}u^*_{nk_0}(r)\hat{p}\,u_{n'k_0}(r)dr^3 \tag{17}$$

Equation (16) is the eigenvalue equation for point $\mathbf{k}$ written in the $\mathbf{k}_0$ representation and it stands correct for any $\mathbf{k}$. But it is most useful for the $\mathbf{k}$ very near $\mathbf{k}_0$ so that the non-diagonal part of the Hamiltonian

$$\frac{\hbar}{m}(k-k_0)\cdot p_{nn'}$$

is small enough to be treated as perturbation.

In ordinary perturbation theory an attempt is made to diagonalize the Hamiltonian completely by an interactive process which works well when all off diagonal elements h_{ij} are small compared to the unperturbed energy separations (E_i-E_j) of the interacting levels. As stated before, index n, n' in equation (16) run over a complete set of bands. But in practice, we are interested in only a few band [ie S & P states: in most cases E_c and E_v]. So we are not going to diagonalize the whole H matrix in equation (16). Instead, we use a type of perturbation theory described by Löwdin [39] in which he divides all states into two classes A and B. States in category A interact weakly with any state in category B. The interaction connecting states in A with states in B is then removed in lowest order just as in the ordinary perturbation theory, but no attempt is made in this first step to remove the matrix elements connecting states in A. After removal of the interaction between A and B, the states in A are left with "renormalized" interaction with one another.

Löwdin has shown that

$$h'_{ij} = h_{ij} + \sum_{\beta}^{B} \frac{h_{i\beta} h_{\beta j}}{E_i - E_j} \qquad \textbf{(18)}$$

Where h_{ij} is initial matrix element, h'_{ij} is the renormalized matrix element, i, j are in A and ß is in B. E_i is the eigenvalue of state i, which is determined self-consistently by the eigenvalue equation

$$\sum_{j}^{A}(h'_{ij}-E_i\delta_{ij})C_{ji}=0 \qquad i,j \in A \tag{19}$$

The coefficients C_{ji} refer to the expansion of perturbed wave function Ψ'_i in terms of unperturbed wave function Ψ_j

$$\psi'_i=\sum_{j}^{A,B} C_{ji}\psi_j \tag{20}$$

Equation (19) gives the coefficients for states i, j in A. When i is in A but j is in B the coefficients are

$$C_{ji}=\sum_{k}^{A}\frac{h_{jk}}{E_i-h_{jj}}C_{ki} \qquad j \in B, \quad i,k \in A \tag{21}$$

The eigenvalue E_i in equation (18) and (21) may usually be replaced by unperturbed value h_{ii}.

Now the renormalized subspace spanned by A should be diagonalized exactly. According to Löwdin set A is selected such that

$$|h_{ij}| << |E_i-E_j| \qquad i \in A, j \in B \tag{22}$$

In a extreme particular case of single band in A class, it turns out to be like normal perturbation to second order. Equation (16) reads

$$E_n(k)=E_n(k_0)+\frac{\hbar}{m}(k-k_0)\cdot p_{nn}+\frac{\hbar^2}{2m}(k^2-k_0^2)+\frac{\hbar^2}{m}\sum_{n'}\frac{|(k-k_0)\cdot p_{nn'}|^2}{E_n(k_0)-E_{n'}(k_0)} \tag{23}$$

Usually the expansion point $\mathbf{k}_0$ is an extremum, so that $\mathbf{p}_{nn}+\hbar\mathbf{k}_0=0$ and axes can always be chosen such that the quadratic terms in equation (23) have no cross product. Assuming k_0 is an extremum point and use principal axes, equation (23) becomes

$$E_n(k)=E_n(k_0)+\frac{\hbar^2}{2}\sum_{i}^{3}\frac{(k_i-k_{i_0})^2}{m_i} \tag{24}$$

Where

$$\frac{1}{m_i}=\frac{1}{m}+\frac{2}{m^2}\sum_{n'}\frac{|i\cdot p_{nn'}|^2}{E_n(k_0)-E_{n'}(k_0)} \tag{25}$$

i stand for the unit vector in i'th principal axes' direction.

1. *k·p Representation without Spin-Orbit terms at* Γ*: k=0*

It is appropriate to lump the conduction band and valence bands in Löwdin's class A and all other states in B.

The valence band maxima of all interested semiconductors occur at k=0, if we neglect the small linear-k term due to spin-orbit interaction. The symmetry type is given by bonding p-function in the tight-binding picture, namely, Γ_{15} in zinc blend structure and Γ_{25} in diamond structure. For direct gap materials the lowest conduction band corresponds to an antibonding s-state with a symmetry type of Γ_1.

Without spin-orbit interaction, the "renormalized" $\mathbf{k}\cdot\mathbf{p}$ interaction matrix for class A may be given as in Table 2.

Table 2

	S	X	Y	Z
S	$\mathbf{A'}k^2+E_c+\hbar^2k^2/2m_0$	$\mathbf{B}k_yk_z+i\mathbf{P}k_x$	$\mathbf{B}k_xk_z+i\mathbf{P}k_y$	$\mathbf{B}k_xk_y+i\mathbf{P}k_z$
X	$\mathbf{B}k_yk_z-i\mathbf{P}k_x$	$\mathbf{L'}k_x^2+\mathbf{M}(k_y^2+k_z^2)+E_v+\hbar^2k^2/2m_0$	$\mathbf{N'}k_xk_y$	$\mathbf{N'}k_xk_z$
Y	$\mathbf{B}k_xk_z-i\mathbf{P}k_y$	$\mathbf{N'}k_xk_y$	$\mathbf{L'}k_y^2+\mathbf{M}(k_x^2+k_z^2)+E_v+\hbar^2k^2/2m_0$	$\mathbf{N'}k_yk_z$
Z	$\mathbf{B}k_xk_y-i\mathbf{P}k_z$	$\mathbf{N'}k_xk_z$	$\mathbf{N'}k_yk_z$	$\mathbf{L'}k_z^2+\mathbf{M}(k_x^2+k_y^2)+E_v+\hbar^2k^2/2m_0$

Where

$$L' \equiv F' + 2G \tag{26}$$

$$M \equiv H_1 + H_2 \tag{27}$$

$$N' \equiv F' - G + H_1 - H_2 \tag{28}$$

$$F' \equiv \frac{\hbar^2}{m^2}\sum_{j}^{\Gamma_1{}'} \frac{|<X|\hat{p}_x|u_j>|^2}{E_v - E_j} \tag{29}$$

$$G \equiv \frac{\hbar^2}{2m^2}\sum_{j}^{\Gamma_{12}} \frac{|<X|\hat{p}_x|u_j>|^2}{E_v - E_j} \tag{30}$$

$$H_1 = \frac{\hbar^2}{m^2}\sum_{j}^{\Gamma_{15}} \frac{|<X|\hat{p}_y|u_j>|^2}{E_v - E_j} \tag{31}$$

$$H_2 = \frac{\hbar^2}{m^2}\sum_{j}^{\Gamma_{25}} \frac{|<X|\hat{p}_y|u_j>|^2}{E_v - E_j} \tag{32}$$

$$A' = \frac{\hbar^2}{m^2}\sum_{j}^{\Gamma_{15}{}'} \frac{|<X|\hat{p}_x|u_j>|^2}{E_c - E_j} \tag{33}$$

$$B = \frac{2\hbar^2}{m^2}\sum_{j}^{\Gamma_{15}{}'} \frac{<s|\hat{p}_x|u_j><u_j|\hat{p}_y|Z>}{(E_c - E_v)/2 - E_j} \tag{34}$$

$$P = -i\frac{\hbar}{m}<s|\hat{p}_x|X> \tag{35}$$

The sums in equations (29) through (34) are over all states u_j transforming like Γ_i as indicated above the summation signs. The prime on the summation in equations (29), (33), and (34) means that states in our four-dimensional subspace spanned by class A are not to be summed over.

2. *Spin-Orbit Interaction*

When approaching the non-relativistic limit from Dirac equation, one additional term shows up in the Hamiltonian of equation (9), namely [63],

$$\hat{H}_{so}=\frac{\hbar}{4m^2c^2}(\nabla V\times\hat{p})\cdot\boldsymbol{\sigma} \tag{36}$$

which is known as spin-orbit interaction term or Thomas term. This $\hat{H}_{so}$, when added to Equation (9), generates two terms in equations (11) and (13)

$$\begin{aligned}\hat{H}_{kso}&=\eta_1+\eta_2\\ S&\equiv\frac{\hbar}{4m^2c^2}(\nabla V\times\hat{p})\\ \eta_1&\equiv S\cdot\boldsymbol{\sigma}\\ \eta_2&\equiv\frac{\hbar^2}{4m^2c^2}(\nabla V\times k)\cdot\boldsymbol{\sigma}\end{aligned} \tag{37}$$

3. *Three band approximation for finite spin-orbit coupling*

When we consider spin, our four-dimensional s-p subspace becomes eight-dimensional in principle. If we transform them to the $|J,m_j>$ representation, the energies at k=0 are diagonal

$$
\begin{array}{lll}
u_i \quad |J,m_J>; & \psi_{Jm_J} & H(k=0) \\
u_1 \quad |\frac{1}{2},\frac{1}{2}>; & s\uparrow & E_c \\
u_2 \quad |\frac{1}{2},-\frac{1}{2}>; & s\downarrow & E_c \\
u_5 \quad |\frac{3}{2},\frac{3}{2}>; & +\left[\frac{x+iy}{\sqrt{2}}\right]\uparrow & E_{v'}+\Delta/3 \\
u_3 \quad |\frac{3}{2},\frac{1}{2}>; & -\sqrt{\frac{2}{3}}\,z\uparrow+\frac{1}{\sqrt{6}}(x+iy)\downarrow & E_{v'}+\Delta/3 \\
u_4 \quad |\frac{3}{2},-\frac{1}{2}>; & -\frac{1}{\sqrt{6}}(x-iy)\uparrow-\sqrt{\frac{2}{3}}\,z\downarrow & E_{v'}+\Delta/3 \\
u_6 \quad |\frac{3}{2},-\frac{3}{2}>; & -\left[\frac{x-iy}{\sqrt{2}}\right]\downarrow & E_{v'}+\Delta/3 \\
u_7 \quad |\frac{1}{2},\frac{1}{2}>; & \frac{1}{\sqrt{3}}(x+iy)\downarrow+\frac{1}{\sqrt{3}}z\uparrow & E_{v'}-2\Delta/3 \\
u_8 \quad |\frac{1}{2},-\frac{1}{2}>; & -\frac{1}{\sqrt{3}}z\downarrow+\frac{1}{\sqrt{3}}(x-iy)\uparrow & E_{v'}-2\Delta/3
\end{array}
\qquad (38)
$$

the quantity Δ is the spin-orbit coupling splitting

$$\Delta \equiv -3i\left[\frac{\hbar}{4m^2c^2}\right]<x|(\nabla\times p)_y|z> \tag{39}$$

which arises from η_1 in equation (37) and we have ignored η_2 term and any "renormalized" η_1 term. The quantity $E_{v'}$ is the valence band energy at k=0 in absence of spin-orbit interaction and we'll use the notation

$$E_v = E_{v'} + \frac{\Delta}{3} \tag{40}$$

Combining Table 2 and equation (38) will lead to a 8x8 interaction matrix or an eighth-order secular equation which can be easily handled by a computer numerically. But for analytic purposes, we have to simplify the resulting matrix. A good approximation is to first ignore all the **k·p** interaction except the **P** term

$$P = \frac{1}{m}<s|\hat{p}_x|X> \tag{35'}$$

and this will result in

$$
\begin{array}{c|cccccccc}
 & u_1 & u_3 & u_5 & u_7 & u_2 & u_4 & u_6 & u_8 \\
u_1 & E_c & -\sqrt{\frac{2}{3}}P\hbar k_z & P\hbar k_+ & \frac{1}{\sqrt{3}}P\hbar k_z & 0 & -\frac{1}{\sqrt{3}}P\hbar k_- & 0 & -\sqrt{\frac{2}{3}}P\hbar k_- \\
u_3 & -\sqrt{\frac{2}{3}}P\hbar k_z & E_v & 0 & 0 & \frac{1}{\sqrt{3}}P\hbar k_- & 0 & 0 & 0 \\
u_5 & P\hbar k_- & 0 & E_v & 0 & 0 & 0 & 0 & 0 \\
u_7 & \frac{1}{\sqrt{3}}P\hbar k_z & 0 & 0 & E_v-\Delta & \sqrt{\frac{2}{3}}P\hbar k_- & 0 & 0 & 0 \\
u_2 & 0 & \frac{1}{\sqrt{3}}P\hbar k_+ & 0 & \sqrt{\frac{2}{3}}P\hbar k_+ & E_c & -\sqrt{\frac{2}{3}}P\hbar k_z & P\hbar k_- & \frac{1}{\sqrt{3}}P\hbar k_z \\
u_4 & -\frac{1}{\sqrt{3}}P\hbar k_+ & 0 & 0 & 0 & -\sqrt{\frac{2}{3}}P\hbar k_z & E_v & 0 & 0 \\
u_6 & 0 & 0 & 0 & 0 & P\hbar k_+ & 0 & E_v & 0 \\
u_8 & -\sqrt{\frac{2}{3}}P\hbar k_+ & 0 & 0 & 0 & \frac{1}{\sqrt{3}}P\hbar k_z & 0 & 0 & E_v-\Delta
\end{array}
\tag{41}
$$

Where

$$k_{\pm}=\left[\frac{k_x \pm ik_y}{\sqrt{2}}\right] \tag{42}$$

It is not difficult to see that the P interaction between a conduction state S and a valence state

$$\psi_v=\alpha_x X+\alpha_y Y+\alpha_z Z \tag{43}$$

may be written

$$<s|\frac{\hbar}{m}k\cdot\hat{p}|\psi_v>=iP\alpha\cdot k \tag{44}$$

where α is the vector with components α_x, α_y and α_z.

The $\mathbf{k}\cdot\mathbf{p}$ interaction polarizes the valence state entirely along the $\mathbf{k}$ vector.

The spin-orbit interaction is also completely isotropic. The $\mathbf{k}$ vector determines the orbital wave function and can be used as the axis of spin quantization due to the above isotropy. Therefore, we can choose $\mathbf{k} \parallel z$ so that $k_{\pm}=0$ in Table 2 and we obtain

$$(E-E_c)(E-E_v)(E-E_v+\Delta)=P^2k^2(E-E_v+\frac{2}{3}\Delta) \tag{45}$$

$$E=E_v \tag{46}$$

Each solution of equations (45) and (46) is twice degenerate. The solutions of equation (46) do not exhibit any dispersion relation. They correspond to the heavy hole bands whose k-curvature can only be obtained through the inclusion of the $\mathbf{k}\cdot\mathbf{p}$ interaction from remote bands. We know that for $\mathbf{k} \parallel z$ the heavy hole states correspond to $m_j=\pm 3/2$ whereas the solutions of equation (45) correspond to $m_j=\pm 1/2$. In all what follows the eigenstates corresponding to equation (45) will be referred as light particles and the solutions of equation (46) [modified by a partial inclusion of remote band interaction] will be referred as heavy particles.

At $\mathbf{k}=0$ we can find the light particles' effective mass of S and P bands. From equation (45) we have

$$\frac{1}{m_c^*}=\frac{2P^2(E_g+2\Delta/3)}{E_g(E_g+\Delta)} \tag{47}$$

$$\frac{1}{m_v^*}=-\frac{4P^2}{3E_g} \tag{48}$$

Where $E_g=E_c-E_v$ is the forbidden gap between conduction band and valence band. Figure 5 shows the plot of E_i *vs.* k for light particles. As we see that both S and P light particles exhibit non-parabolicity. i.e. m^*_c, m^*_v increase when energy states of interest move away from the band edges.

For the heavy hole bands we must consider the $\mathbf{k}\cdot\mathbf{p}$ interaction from remote bands δ, to restore a finite effective mass. The matrix δ, at zero magnetic field, depends on three Luttinger parameters [64]. They are i) γ_1, γ_2 which take into account P-P interaction via virtual jump to remote bands and ii) F, which takes into account S-S interaction in the same way. The parameter F is not so important for us now since S bands have already significant curvature without δ. δ is diagonal at $k_{\pm}=0$. For our purpose we need only

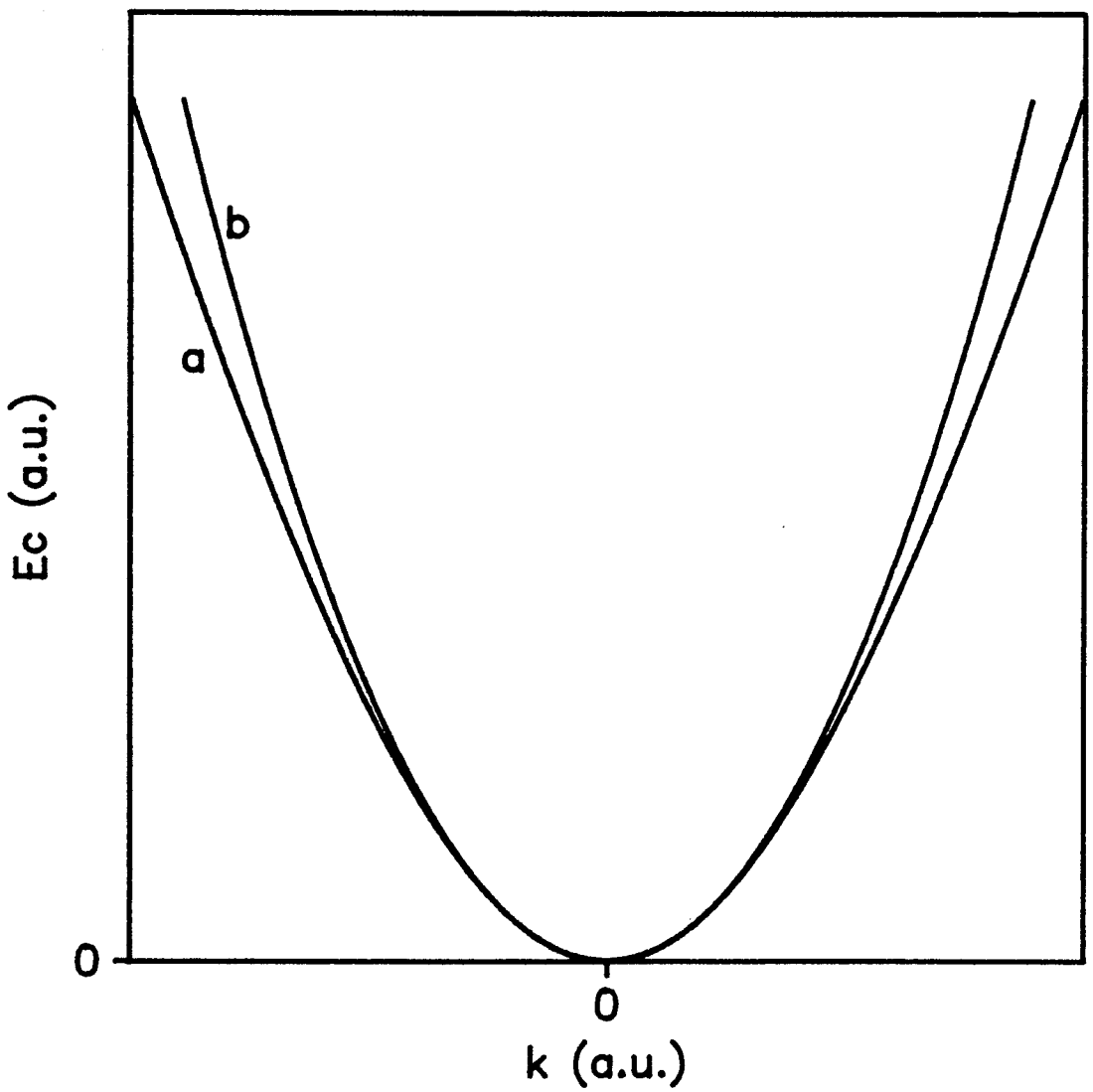

Figure. 5A. Comparison between the conduction band dispersion relations of 3-band model (curve a) and 1-band model (curve b)

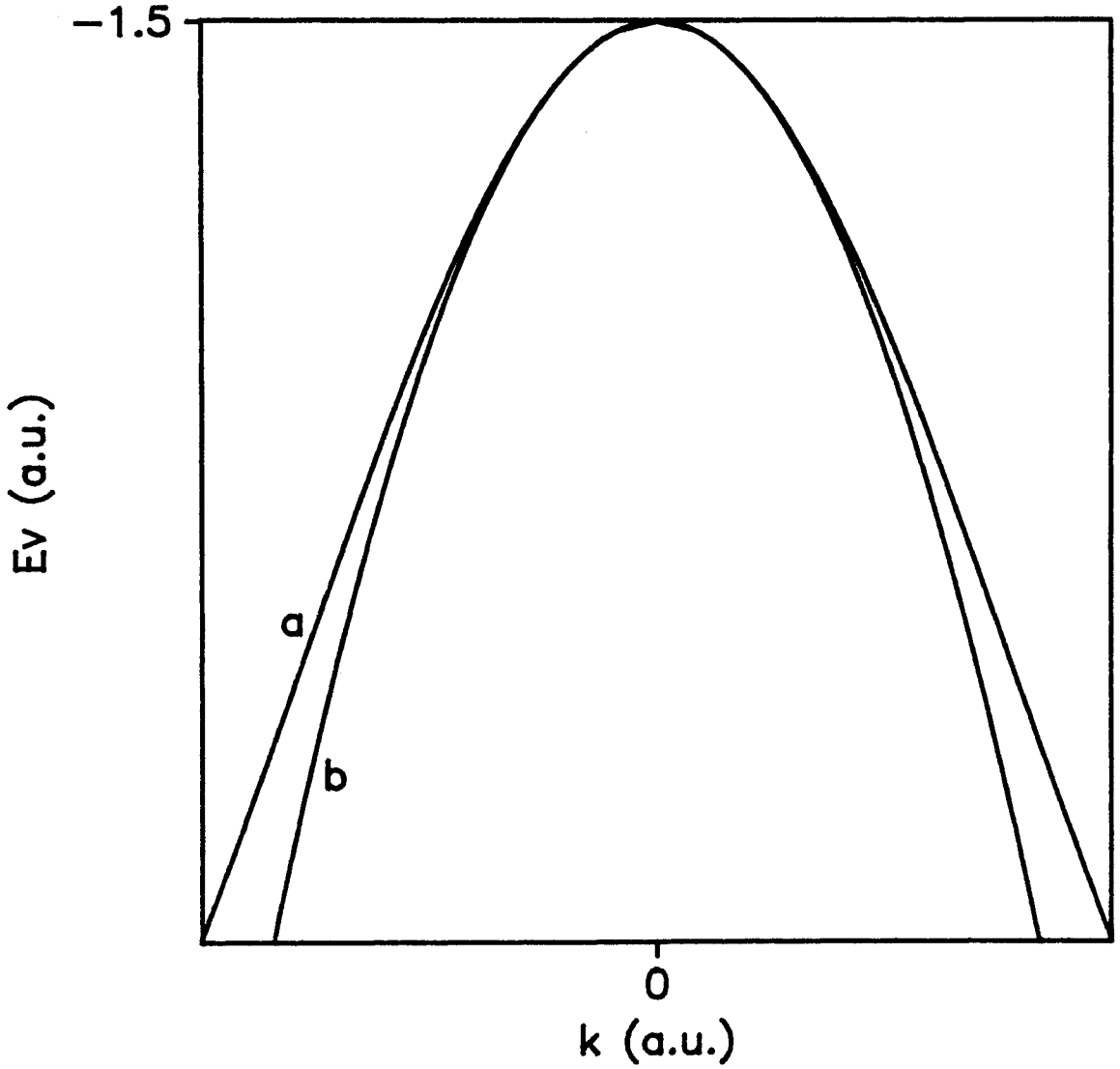

Figure. 5B. Comparison between the light hole band dispersion relations of 3-band model (curve a) and 1-band model (curve b).

$$<\frac{3}{2},\pm\frac{3}{2}|\delta|\frac{3}{2},\pm\frac{3}{2}>=-\frac{\hbar^2k^2}{2m_{hh}^*}=(-\gamma_1+2\gamma_2)\frac{\hbar^2k^2}{2m} \quad (49)$$

$$<\frac{3}{2},\pm\frac{1}{2}|\delta|\frac{3}{2},\pm\frac{1}{2}>=-\frac{\hbar^2k^2}{2\mu}=(-\gamma_1-2\gamma_2)\frac{\hbar^2k^2}{2m} \quad (50)$$

The remote bands' contribution to light hole effective mass $1/\mu$ is also negligible compared to what already exists.

§ 4-2 Three-band envelope function model for heterostructures without strain

In this section I will discuss the electronic states in the heterostructures constituted from lattice-matched semiconductors. The strained-layer heterostructures will be discussed in section § 4-6 after the strain effect on bulk materials' band edges and the interpolation scheme are discussed in § 4-3, § 4-4, § 4-5 respectively.

Envelope function models are based on two principal remarks. First, the band offsets are normally a small fraction of the host band widths and second, the band structures of constituent layers are usually very similar. The first remark suggests that within a fraction of 1 eV around a certain band edge of one constituent material the same band edge of the other material is likely to be found. The second remark means that these edges are of same symmetry (say, Γ_6 for conduction band). This favorable situation

occurs in all the samples studied in our laboratory so far. The heterostructure states are built out of bulk states of Γ edges in both constituent materials. These bulk states can be described in terms of the **k·p** expansion around Γ point as discussed in the section § 4-1. Our task now is to generalize the **k·p** hamiltonian so that it will account for the band offsets. If, on the other hand, the band edges involved are of different symmetry, like the conduction bands in Si/Ge heterostructures, no simple treatment is possible.

Under flat band condition, the wave function of an electron in a heterostructure with unidirectional (z-axis) composition modulation can be written

$$\psi(r)=\sum_{l=1}^{8}\left\{[u_{l0}^{(A)}(r)a_l(k_l^{(A)})e^{ik_l^{(A)}\cdot r}]Y(z\in A)\right. \\ \left.+[u_{l0}^{(B)}(r)b_l(k_l^{(B)})e^{ik_l^{(B)}\cdot r}]Y(z\in B)\right\} \tag{51}$$

within the framework of the Kane model [30, 38]. In above equation $\mathbf{k}_l^{(A)}$ and $\mathbf{k}_l^{(B)}$ are the wave vectors given by the implicit equations

$$\varepsilon_l^{(A)}(k_l^{(A)})=\varepsilon \qquad \varepsilon_l^{(B)}(k_l^{(B)})=\varepsilon \tag{52}$$

and $u_{l0}^{(A)}(\mathbf{r})$, $u_{l0}^{(B)}(\mathbf{r})$ are the Bloch function for *l*th band edges at Γ point. Finally Y(z ∈ A) denotes the step function which is equal to 1 in A layer and 0 elsewhere. Imposing the boundary conditions at the interfaces and demanding a certain asymptotic behavior of $\Psi(\mathbf{r})$ will lead us to a set of linear homogenous equations for $a_l(\mathbf{k}_l^{(A)})$ and $b_l(\mathbf{k}_l^{(B)})$. The condition under which non-zero solution for $a_l(\mathbf{k}_l^{(A)})$ and $b_l(\mathbf{k}_l^{(B)})$ exists will determine the

allowed energy levels (mini bands) in the hetero-structure. What asymptotic behavior $\psi(\mathbf{r})$ should have depends on the problem at hand. For instance, in a superlattice structure we require $\psi(\mathbf{r})$ to satisfy Bloch's theorem

$$\psi(r+dn_z)=e^{iqd}\psi(r) \tag{53}$$

where d is the superlattice periodicity and $\mathbf{n}_z$ is the unit vector along z (growth) axis. In a single quantum well or a small number of coupled quantum well structure we require that $\psi(\mathbf{r})\to 0$ far away from the wells. The translational invariance in the layer plane suggests that the in-plane projection of the electron wave vector

$$k_\perp=(k_x,k_y) \tag{54}$$

is a good quantum number. Therefore

$$k_l^{(A)}=(k_\perp,k_{zl}^{(A)}) \qquad\qquad k_l^{(B)}=(k_\perp,k_{zl}^{(B)}) \tag{55}$$

This allow us to rewrite equation (51) in the form

$$\psi(r)=e^{ik_\perp\cdot r_\perp}\sum_{l=1}^{8}\left\{\left[u_{l0}^{(A)}(r)f_l^{(A)}(z)\right]Y(z\in A)\left[u_{l0}^{(B)}(r)f_l^{(B)}(z)\right]Y(z\in B)\right\} \tag{56}$$

Where $f_l^{(A)}(z)$, $f_l^{(A)}(z)$ are the envelope function that vary slowly on the scale of the host lattice periodicity.

To construct the effective $\mathbf{k}\cdot\mathbf{p}$ hamiltonian acting on the envelope functions, we follow the procedure as discussed in § 4-1 starting with the hamiltonian in the form

$$\hat{H}=\frac{\hat{p}^2}{2m_0}+V_A(r)Y(z\in A)+V_B(r)Y(z\in B) \tag{57}$$

By definition, $u_{l0}^{(A)}$ and $u_{l0}^{(A)}$ are the solution of

$$\begin{cases}\left[\dfrac{\hat{p}^2}{2m_0}+V_A(r)\right]u_{l0}^{(A)}(r)=\varepsilon_l^{(A)}u_{l0}^{(A)}(r) & z\in A\\ \left[\dfrac{\hat{p}^2}{2m_0}+V_B(r)\right]u_{l0}^{(B)}(r)=\varepsilon_l^{(B)}u_{l0}^{(B)}(r) & z\in B\end{cases} \tag{58}$$

Letting $\hat{H}$ in equation (57) act on equation (56), multiplying by $u_{m0}^{*}(\mathbf{r})$ [from left], integrating over a unit cell, substituting in equation (58), and making use of the different scale of variation of envelope function f_l and the cell periodic part u_{l0}, we end up with

$$\begin{cases}D^{(A)}f^{(A)}=\varepsilon f^{(A)} & z\in A\\ D^{(B)}f^{(B)}=\varepsilon f^{(B)} & z\in B\end{cases} \tag{59}$$

where $\mathbf{f}^{(A)}$ and $\mathbf{f}^{(B)}$ are 8x1 column vector whose components $f_l^{(A)}$ and $f_l^{(B)}$ are solutions of the coupled differential systems

$$\left[\varepsilon_l^{(A)}+\frac{\hbar^2 k_\perp^2}{2m_0}-\frac{\hbar^2}{2m_0}\frac{\partial^2}{\partial z^2}\right]f_m^{(A)}(z)+$$

$$\sum_{l=1}^{8}\left[\frac{\hbar k_\perp}{m_0}\left\langle u_{m0}^{(A)}\middle|p_\perp\middle|u_{l0}^{(A)}\right\rangle+\frac{1}{m_0}\left\langle u_{m0}^{(A)}\middle|p_z\middle|u_{l0}^{(A)}\right\rangle\frac{\hbar}{i}\frac{\partial}{\partial z}\right]f_l^{(A)}(z)=\varepsilon f_m^{(A)}(z)\qquad z\in A$$

$$\left[\varepsilon_l^{(B)}+\frac{\hbar^2 k_\perp^2}{2m_0}-\frac{\hbar^2}{2m_0}\frac{\partial^2}{\partial z^2}\right]f_m^{(B)}(z)+$$

$$\sum_{l=1}^{8}\left[\frac{\hbar k_\perp}{m_0}\left\langle u_{m0}^{(B)}\middle|p_\perp\middle|u_{l0}^{(B)}\right\rangle+\frac{1}{m_0}\left\langle u_{m0}^{(B)}\middle|p_z\middle|u_{l0}^{(B)}\right\rangle\frac{\hbar}{i}\frac{\partial}{\partial z}\right]f_l^{(B)}(z)=\varepsilon f_m^{(B)}(z)\qquad z\in B$$

(60)

$D^{(A,B)}$ is the effective hamiltonian we are looking for and it is almost identical to the Kane matrix given in equation (41) except that:

1) its elements are position (z) dependent.

2) the wave vector k_z, which is no longer conserved, is replaced by $-i\partial/\partial z$ like in the usual effective mass calculations.

1. *Superlattices*

A superlattice is an infinite array of layers such that we can define an elementary cell generating the whole lattice by successive translations of the fundamental period d along the growth axis. The simple case discussed here is the binary superlattice ABABAB....., whose elementary cell is composed of two undoped layers of A and B

materials with thickness of L_A and L_B respectively. The periodicity of the superlattice hamiltonian implies that the eigenstates fulfill the Bloch's theorem

$$\hat{T}_d f_q(z)=f_q(z+d)=e^{iqd}f_q(z) \tag{61}$$

where $\hat{T}_d$ is the translational operator of $d=L_A+L_B$, and q is the superlattice wave vector that belongs to the segment $[-\pi/d, \pi/d]$. As proved in textbooks, by applying Bloch's theorem and expressing the fact that inside a unit cell the general (superlattice) solution is a linear combination of the two independent solutions of the Schrödinger equation, the superlattice dispersion relation has the form [65]

$$\cos(qd)=f(\varepsilon) \tag{62}$$

where the function $f(\varepsilon)$ depends on the exact shape of the band edge profile inside the unit cell.

A significant simplification can be made when the in-plane wave vector $\mathbf{k}_{\pm}$ is set equal zero. An inspection of equations (41) and (60) reveals that:

1) the effective hamiltonian splits into two decoupled identical blocks and the eigenstates are twice (Kramers) degenerate, and

2) the states associated with heavy hole band edges $|\ 3/2,\pm 3/2>$ become decoupled from those associated with light particle band edges $|\ S,\pm 1/2>$, $|\ 3/2,\pm 1/2>$ and $|\ 1/2,\pm 1/2>$.

The decoupled heavy hole states in the heterostructure can be obtained by solving a scaled Kronig-Penney equation

$$\left[\hat{p}_z \frac{1}{2m^*_{hh}(z)} \hat{p}_z + E_v(z)\right] f_{hh}(z) = \varepsilon f_{hh}(z) \tag{63}$$

Since the effective mass jumps at the interfaces,it changes the continuity of df/dz in the Kronig-Penney model into that of $(1/m^*_{hh})df/dz$ at interfaces. This is consistent with the requirement of the conservation of the probability current. As discussed in § 4-1, the heavy hole effective mass does not originate from the direct $\mathbf{k}\cdot\mathbf{p}$ coupling between the Γ_6, Γ_7 and Γ_8 edges. Instead, it arises from the indirect (second-order) $\mathbf{k}\cdot\mathbf{p}$ interaction between these states through virtual transitions to remote band edges of the crystal. To restore finite heavy hole effective mass, Luttinger parameters can be introduced [see equations (49), (50)]. This will change equation (63) into

$$\left[-\frac{1}{2m_0} \hat{p}_z (\gamma_1(z) - 2\gamma_2(z)) \hat{p}_z + E_v(z)\right] f_{hh}(z) = \varepsilon f_{hh}(z) \tag{63'}$$

For light particles' states it is possible to express all the components of **f** in terms of a single one, say, Γ_6-related f_c. If, to be consistent with the Kane model, we neglect the free electron kinetic energy in equation (60) it can be written as

$$\left[\hat{p}_z \frac{1}{2m^*(\varepsilon,z)} \hat{p}_z + E_c(z)\right] f_c(z) = \varepsilon f_c(z) \tag{64}$$

where

$$\frac{1}{m^*(\varepsilon,z)} = \frac{2P^2(z)}{3}\left[\frac{2}{\varepsilon - E_v(z)} + \frac{1}{\varepsilon - E_v(z) + \Delta(z)}\right] \tag{65}$$

and **P**(z) is the Kane matrix element defined by equation (35'). Equation (65) has the same form as Ben-Daniel-Duke problem [66] except that in equation (65) $m^*(\varepsilon,z)$ is energy dependent. This energy dependency is due to the coupling between conduction band and valence band. As in the usual Ben-Daniel-Duke problem, f_c and $m^*(\varepsilon,z)^{-1}df_c/dz$ have to be continuous at the interfaces. Inside each A or B layer of a superlattice unit cell, f_c is a linear combination of an incoming and an outgoing plane waves characterized by wave vector $k_z^{(A)}$ and $k_z^{(B)}$ in each layer respectively. Hence we have two unknown coefficients in each layer of the superlattice unit cell. The four boundary conditions at two interfaces leave us with a set of four linear homogeneous equations for four unknowns. Non-zero solutions exist only if the determinant is equal to zero, which leads us to the equation

$$\cos(qd)=\cos(k_A L_A)\cos(k_B L_B)-\frac{1}{2}(\xi+\frac{1}{\xi})\sin(k_A L_A)\sin(k_B L_B) \tag{66}$$

where k_A, k_B and ξ are defined by

$$\begin{aligned}(\varepsilon-E_c(A))(\varepsilon-E_v(A))(\varepsilon-E_v(A)+\Delta(A))&=\hbar^2k_A^2P^2(A)\left[\varepsilon-E_v(A)+\frac{2\Delta(A)}{3}\right]\\(\varepsilon-E_c(B))(\varepsilon-E_v(B))(\varepsilon-E_v(B)+\Delta(B))&=\hbar^2k_B^2P^2(B)\left[\varepsilon-E_v(B)+\frac{2\Delta(B)}{3}\right]\end{aligned} \tag{67}$$

$$\xi=\frac{k_A m_B^*}{k_B m_A^*} \tag{68}$$

and $m^*_{A,B}$ is defined in equation (65). Equations similar to (66) ~ (68) hold for heavy hole superlattice states except that the dispersions are parabolic in k

$$\varepsilon-E_v(A)=\frac{\hbar^2k_A^2}{2m_{hh}^*(A)} \qquad \varepsilon-E_v(B)=\frac{\hbar^2k_B^2}{2m_{hh}^*(B)} \tag{69}$$

and

$$m^*\Rightarrow m_{hh}^* \tag{70}$$

The superlattice dispersion relation in equation (66) is obtained by assuming the eigenstates are propagating in both A and B layers. In practice, however, these unconfined states are not most commonly encountered in experiments since they are never the ground superlattice states. The confined states in a superlattice are the hybrid

of propagating states in one kind of layers, for definiteness say A layers, and the evanescent states in the other kind of layers (B layers). In this case the allowed energy ε is in B layers' band gap. With the change $k_B \Rightarrow i\kappa$ we obtain $\xi \Rightarrow -i\eta$ and equation (66) becomes

$$\cos(qd)=\cos(k_A L_A)\cosh(\kappa_B L_B)-\frac{1}{2}\left[\eta-\frac{1}{\eta}\right]\sin(k_A L_A)\sinh(\kappa_B L_B) \qquad (71)$$

The right hand side of equation (71) is the $f(\varepsilon)$ we wanted in equation (62). Because $|\cos(qd)| \leq 1$ the allowed superlattice states (mini bands) correspond to the energy segments where $|f(\varepsilon)| \leq 1$. The energy ranges where $|f(\varepsilon)| \geq 1$ correspond to the forbidden gaps between the mini bands.

2. *Isolated Single Quantum Wells*

For a single quantum well, the symptotic behavior of f_c is governed by the requirement that $f_c \to 0$ far away from the well instead of obeying Bloch's theorem. By imposing this requirement and the boundary conditions in solving equations (63) and (64), we end up with the equation for allowed energy states in an isolated single quantum well

$$\cos(k_A L_A)+\frac{1}{2}\left[\eta-\frac{1}{\eta}\right]\sin(k_A L_A)=0 \qquad (72)$$

where k_A, k_B and η are defined as before. Equation (72) indicates that, without in-plane dispersion, the allowed energy states in an isolated single quantum well are discrete. When the barrier layers in a superlattice become extremely thick the wells become isolated. This can be readily verified by taking the limit $L_B \to \infty$, which also lead us to equation (72).

3. *Coupled Double-Well Structure*

When two identical quantum wells are separated by a very thick barrier the interaction between them can be ignored and the allowed energy states in these wells can be seen as twice degenerate. As the thickness of the barrier between these wells is reduced the "tail" of the wave function from one well can have some finite value in the other well. In the tight-binding picture, this wave function overlap can be treated as perturbation which splits the degenerate well level into a symmetric and an antisymmetric state respectively.

The coupled double-well structure problem is also manageable within the framework of envelope function approach. By solving equations (63) and (64), imposing boundary conditions at four interfaces and demanding $f_c \to 0$ far away from the wells, we end up with a set of eight linear homogeneous equations for eight unknowns. By taking

advantage of the symmetry of the structure, the problem can be reduced to 4x4. The condition for non-zero solutions to exist leads us to following bound states equation

$$2\cos(k_A L_A)+\left[\eta-\frac{1}{\eta}\right]\sin(k_A L_A)\mp\left[\eta+\frac{1}{\eta}\right]\sin(k_A L_A)\exp(-\kappa_B L_B)=0 \qquad (73)$$

Where L_B is the thickness of the barrier between the wells and other parameters are defined as before. The minus sign refers to the symmetric (with respect to the midpoint of central barrier, z=0) states and the plus sign refers to the antisymmetric states.

§ 4-3 Strain induced effect on energy bands

In hetero-structure systems there always exists, more or less, lattice mismatch between the materials on both side of the interfaces. This will induce two dimensional strain, tensile or compression, which can be equivalently treated as a sum of a hydraulic strain and a uniaxial strain.

The hydraulic component of the strain shifts different bands while the uniaxial component removes the cubic symmetry, i.e. lowers the symmetry from T_d to D_{2d} and the J=3/2 P bands split further into a pair of Kramers' doublets. According to deformation potential theory [67], the strain hamiltonian $\hat{H}_\varepsilon$ for a p-like multiplet can be written as [68]

$$\hat{H}_\epsilon = \hat{H}_\epsilon^{(1)} + \hat{H}_\epsilon^{(2)}$$

$$\hat{H}_\epsilon^{(1)} = -a_1 Tr(\epsilon) - 3b_1 \left[\left(\hat{L}_x^2 - \frac{1}{3}\hat{L}^2 \right) \epsilon_{xx} + c.p. \right] - \sqrt{3}\, d_1 \left[\left(\hat{L}_x \hat{L}_y + \hat{L}_y \hat{L}_x \right) \epsilon_{xy} + c.p. \right] \qquad (74)$$

$$\hat{H}_\epsilon^{(2)} = -a_2 (\hat{L} \cdot \sigma) Tr(\epsilon) - 3b_2 \left[\left(\hat{L}_x \sigma_x - \frac{1}{3}\hat{L} \cdot \sigma \right) \epsilon_{xx} + c.p. \right] - \sqrt{3}\, d_2 \left[\left(\hat{L}_x \sigma_y + \hat{L}_y \sigma_x \right) \epsilon_{xy} + c.p. \right]$$

Where $\hat{H}_\varepsilon^{(1)}$ is the orbital-strain hamiltonian and $\hat{H}_\varepsilon^{(2)}$ is the strain dependent spin-orbit hamiltonian, ε and ε_{ij} denote strain tensor and its components, $\hat{L}$ is the orbital angular momentum operator, σ the Pauli matrix vector and c.p. stands for cyclic permutation with respect to the indices x, y, z. $\mathbf{a}_1$ is intraband (absolute) hydrostatic deformation potential while $\mathbf{b}_1$ and $\mathbf{d}_1$ are orbital uniaxial deformation potentials appropriate to strains of tetragonal and rhombohedral symmetries respectively. $\mathbf{a}_2$, $\mathbf{b}_2$ and $\mathbf{d}_2$ are additional deformation potentials describing the effects of a strain on the spin-orbital interaction.

The effect of a strain on conduction band edge E_c is to produce a hydrostatic shift given by

$$\hat{H}_\epsilon^{(c)} = a_c Tr(\epsilon) \qquad (75)$$

Where $\mathbf{a}_c$ is the intraband (absolute) hydrostatic deformation potential of the conduction band.

For a biaxial strain in the $<001>$ plane we have

$$\begin{aligned}
\epsilon_{xx}=\epsilon_{yy}=\epsilon&=\frac{a_{\perp}-a_0}{a_0}\\
\epsilon_{zz}&=-\frac{2C_{12}}{C_{11}}\epsilon\\
\epsilon_{xy}=\epsilon_{yz}=\epsilon_{zx}&=0
\end{aligned} \tag{76}$$

where $a_{\perp}$ is the in-plane lattice constant, a_0 the lattice constant without strain and C_{11} and C_{12} are elastic tensor elements.

Since the strain does not remove Kramer's degeneracy, at $\mathbf{k}=0$, the Kane matrix with strain considered still has two identical blocks

$$\begin{array}{c}
\begin{array}{cccc}
|S,\frac{1}{2}> & |\frac{3}{2},\frac{3}{2}> & |\frac{3}{2},\frac{1}{2}> & |\frac{1}{2},\frac{1}{2}>
\end{array}\\
\begin{bmatrix}
E_{c0}+\delta E_{H,c} & 0 & 0 & 0\\
0 & E_{vav}+\frac{\Delta}{3}-\delta E_{H,v}-\Delta E_s & 0 & 0\\
0 & 0 & E_{vav}+\frac{\Delta}{3}-\delta E_{H,v}+\delta E_s & \sqrt{2}E_s'\\
0 & 0 & \sqrt{2}\,\delta E_s' & E_{vav}-\frac{2\Delta}{3}-\delta E_{H,v}'
\end{bmatrix}
\end{array} \tag{77}$$

Where

$$\begin{aligned}
\delta E_{H,c}&=a_c(2-\lambda)\epsilon\\
\delta E_{H,v}&=(a_1+a_2)(2-\lambda)\epsilon=a(2-\lambda)\epsilon\\
\delta E_{H,v}'&=(a_1-2a_2)(2-\lambda)\epsilon=a'(2-\lambda)\epsilon\\
\delta E_s&=-(b_1+2b_2)(1+\lambda)\epsilon=-b(1+\lambda)\epsilon\\
\delta E_s'&=-(b_1-b_2)(1+\lambda)\epsilon=-b'(1+\lambda)\epsilon
\end{aligned} \tag{78}$$

$$\lambda=\frac{2C_{12}}{C_{11}}$$

E_{c0} is the conduction band edge without strain and E_{vav} is the "Center of Gravity" of the p-like multiplet given by Harrison Atomic-like Orbital (HAO) theory [69].

Normally, the strain dependence of spin-orbit interaction is not very large and can be ignored. Therefore

$$\begin{aligned} a' &\approx a \approx a_1 \\ b' &\approx b \approx b_1 \\ \delta E_{H,v} &\approx \delta E'_{H,v} \approx a_1(2-\lambda)\epsilon \\ \delta E_s &\approx \delta E'_s \approx -b_1(1+\lambda)\epsilon \end{aligned} \tag{79}$$

Under these approximations, the strain dependence of the four energy band edges of interest can be expressed as

$$\begin{aligned} E_c &= E_{vav} + \frac{\Delta}{3} + E_g + \delta E_{H,v} \\ E_{hh} &= E_{vav} + \frac{\Delta}{3} - \delta E_{H,v} - \delta E_s \\ E_{lh} &= E_{vav} - \frac{\Delta}{6} - \delta E_{H,v} + \frac{1}{2}\delta E_s + \frac{1}{2}\left[\Delta^2 + 2\Delta\delta E_s + 9(\delta E_s)^2\right]^{\frac{1}{2}} \\ E_{so} &= E_{vav} - \frac{\Delta}{6} - \delta E_{H,v} + \frac{1}{2}\delta E_s - \frac{1}{2}\left[\Delta^2 + 2\Delta\delta E_s + 9(\delta E_s)^2\right]^{\frac{1}{2}} \end{aligned} \tag{80}$$

The analysis for the biaxial strain in $<111>$ or any other plane can be carried out in the same approach. But beside the strain shift and splitting of the band edges, however, one should keep in mind that zinc-blend structure semiconductors are piezo-electric materials and the off-diagonal strain elements induce a polarization given by [70]

$$P_i^s = \sum_{jk} e_{ijk}\epsilon_{jk} \tag{81}$$

where P^s_i is the *i*th component of strain induced polarization, e_{ijk} is the piezoelectric constant tensor element. For zinc-blend structured materials, $e_{ijj}=0$. Hence a <001>-grown strained layer structure, which has only diagonal strain elements (ϵ_{xx}, ϵ_{yy}, and ϵ_{zz}), will have no strain induced piezoelectric field. But a strained-layer structure with any other growth direction, which has off diagonal strain components, will have strain-induced piezoelectric field. This complication is nowadays overwhelmed by a number of attractive features, one of the most important being the non-linear optical behavior caused by the screening of the piezoelectric field that occurs when electrons and holes are photogenerated.

§ 4-4 Interpolation Scheme for Band Lineup

In ternary alloys $A_{1-x}B_xC$, if AC and BC are lattice matched, linear interpolation is a valid procedure for material parameters with x. But in the ternary alloys constituted from lattice mismatched binaries the bowing effect should be taken into account. One material should be considered as being hydraulically compressed while the other being hydraulically expanded. For a given energy band edge E_i we have

$$E_i(x) = (1-x)E_i^{/}(AC) + xE_i^{/}(BC) \tag{82}$$

From the deformation potential theory discussed in § 4-3 we know that

$$
\begin{aligned}
E_i'(AC) &= E_i(AC) + a_i(AC)Tr(\epsilon) \\
&= E_i(AC) + 3a_i\epsilon_{AC}(x) \\
E_i'(BC) &= E_i(BC) + a_i(BC)Tr(\epsilon) \\
&= E_i'(BC) + 3a_i\epsilon_{BC}(x)
\end{aligned}
\tag{83}
$$

where

$$
\begin{aligned}
&\epsilon_{AC}(x) = x\frac{\Delta a_0}{a(x)}, \qquad \epsilon_{BC}(x) = (1-x)\frac{-\Delta a_0}{a(x)} \\
&\Delta a_0 = a_0(BC) - a_0(AC) \\
&a(x) = (1-x)a_0(AC) + x a_0(BC)
\end{aligned}
\tag{84}
$$

a_0(AC) and a_0(BC) are lattice constants. a_i(AC) and a_i(AC) are the intraband (absolute) hydrostatic deformation potentials for the band edge E_i. Substitution of equations (83) and (84) into equation (82) yields band edge E_i as a function of x

$$
E_i(x) = (1-x)E_i(AC) + xE_i(BC) + 3x(1-x)\left[a_i(AC) - a_i(BC)\right]\frac{\Delta a_0}{a(x)} \tag{85}
$$

For the variation of band gap with composition x we have

$$
\begin{aligned}
E_g(x) &= E_c(x) - E_v(x) \\
&= (1-x)E_g(AC) + xE_g(BC) + 3x(1-x)[a(AC) - a(BC)]\frac{\Delta a_0}{a(x)}
\end{aligned}
\tag{86}
$$

where a(AC) and a(BC) are the interband (relative) hydrostatic deformation potentials $a = a_c - a_v$. This leads to an approximate bowing parameter

$$b \approx 3[a(AC)-a(BC)]\frac{\Delta a_0}{a_0} \tag{87}$$

here a_0 choose the mid-composition lattice constant. Because the strain dependence of spin-orbit splitting is normally insignificant it is ignored in equations (86) and (87).

According to Hill's theory [101], the bowing parameter b can be calculated from the equation

$$b=\frac{Ze}{8\pi\epsilon_0}\left(\frac{1}{r_A}-\frac{1}{r_B}\right)^2(r_A+r_B)\exp\left(-sa\frac{\sqrt{3}}{8}\right) \tag{88}$$

where Ze is the charge of the substituting ion, a is the lattice constant of the mid-composition alloy, s is the screening factor (0.25), and r_A, r_B are the Pauling's covalent radii of elements A and B respectively.

Based on the above notation, the interpolation scheme should be: starting from HAO theory's $E_{vav}(AC)$ and $E_{vav}(BC)$ [69], adding $1/3\Delta(AC)$ and $1/3\Delta(BC)$ to get $E_v(AC)$ and $E_v(BC)$, and then interpolating $E_v(x)$ by equation (85), and adding the experimental $E_g(x)$ or the $E_g(x)$ given by the bowing equation onto $E_v(x)$ to get $E_c(x)$. To get spin-orbit splitting band $E_{so}(x)$, linearly interpolated $\Delta(x)$ is subtracted from $E_v(x)$. This gives all the band lineups before the strain between the barrier and the well layers is considered.

§ 4-5 Relation Between Parameters of Wurtzite and Zinc-Blend Structure Materials

Due to the progress in growth technique more and more materials can be grown in structures that do not crystalize in bulk (natural) form. This has lead to new flexibility for sample and device designing and at same time proposed new studies in this field. Sometimes we need to transform bulk parameters for certain material in one structure into the one for the same material in different structure. For example, bulk CdSe crystalizes exclusively in Wurtzite structure. So most of the available experimental data on bulk CdSe are from Wurtzite structure CdSe. Recently strained-layer heterostructures involving CdSe have been successively grown [51] in which CdSe crystalize in Zinc-Blend structure. The optical properties of strained-layer ZnSe/$Zn_{1-x}Cd_xSe$ single quantum wells have been studied by Lozykowski and Shastri [71, 72]. To calculate the electronic states in these heterostructures involving Zinc-Blend CdSe, all the bulk material parameters needed (band edges at Γ point and elastic tensor elements etc.) must be transformed from the available ones for Wurtzite structure into the ones for Zinc-Blend structure.

1. *Valence band splittings at Γ point in Zinc-Blend and Wurtzite structures*

The band edges for Zinc-Blend structure have been well described in § 4-1. With cubic symmetry the states P_x, P_y and P_z at Γ point($\mathbf{k}=\mathbf{0}$) are degenerate in the absence

of spin-orbit interaction. In crystals of Wurtzite structure the z axis is distinguished from x and y axes. The degeneracy at Γ point is lifted by this uniaxial interaction. It is also lifted, as in the Zinc-Blend Structure, by the spin-orbit interaction. The former splits P_z from P_x and P_y states while the later splits J=1/2 state from J=3/2 states. Both interactions taken together give rise to three energy levels. The hamiltonian is neither diagonal in $|J,m>$ basis nor in P_i basis. The wave functions for each split band may be written as a linear combination of $|J,m>$ states or P_i states and spin functions (assuming that the conduction band is far away enough to neglect the interaction from it).

Many researchers have reported theoretical works on Wurtzite and Zinc-Blend valence band splittings [73, 74 and 75], all of which fall in the frame work of the so called "quasi-cubic model". Describing the uniaxial interaction in Wurtzite structure in term of a non cubic "crystal field" perturbation δ, the quasi-cubic model gives three energy levels as [76]

$$\begin{aligned} E_{3/2,3/2} &= E_{vav} + \frac{\Delta}{3} \\ E_{+} &= E_{vav} + \frac{\Delta}{3} + A + \left(A^2 - B\right)^{\frac{1}{2}} \\ E_{-} &= E_{vav} + \frac{\Delta}{3} + A - \left(A^2 - B\right)^{\frac{1}{2}} \end{aligned} \qquad \textbf{(89)}$$

with $2A = -\Delta + \delta$ and $B = 2\Delta\delta/3$. E_{vav} is the orbital potential defined in § 4-3. Δ is spin-orbit splitting defined in § 4-1. Note that this formula reproduces the band edges for Zinc-Blend structure at the limit $\delta \to 0$. With experimental values of $E_{3/2,3/2}$ and $E_{\pm}$ [77]

equation (89) can be solved for E_{vav} and Δ so that construction of band edges for Zinc-Blend structure at Γ point is possible.

2. *Relation between elastic tensors of Wurtzite and Zinc-Blend Structure materials*

Both Wurtzite and Zinc-Blend are from the RX_4 crystal class [78] in which the structure unit has a regular tetrahedron of X atoms about a single R atom. In Zinc-Blend crystals all tetrahedra are equivalent with their corners lying along $<111>$ direction. In Wurtzite crystals there are two inequivalently oriented tetrahedra each of which can be obtained from the standard Zinc-Blend orientation by rotations given by Robinson [79]

$$R^{(1)} = \frac{1}{\sqrt{6}}\begin{bmatrix} \sqrt{3} & 0 & \sqrt{3} \\ -1 & 2 & 1 \\ -\sqrt{2} & -\sqrt{2} & \sqrt{2} \end{bmatrix}$$
$$R^{(2)} = -\frac{1}{\sqrt{6}}\begin{bmatrix} \sqrt{3} & 0 & \sqrt{3} \\ -1 & 2 & 1 \\ \sqrt{2} & \sqrt{2} & -\sqrt{2} \end{bmatrix} \qquad \textbf{(90)}$$

The tensor $T^{(n)}_{ijkl...}$ in each of these two Wurtzite system is related to $T^{ZB}_{i'j'k'l'...}$ by

$$T^{(n)}_{ijkl...} = R^{(n)}_{ii'} R^{(n)}_{jj'} R^{(n)}_{kk'} R^{(n)}_{ll'} \ldots T^{ZB}_{i'j'k'l'...} \qquad \textbf{(91)}$$

Let us define the strain and elastic tensors for the two orientations to be $\epsilon^{(1)}_{ij}$, $\epsilon^{(2)}_{ij}$, $C^{(1)}_{ijkl}$, $C^{(2)}_{ijkl}$ and eighth-rank tensors

$$P^{(n)}_{ii'jj'kk'll'}=R^{(n)}_{ii'}R^{(n)}_{jj'}R^{(n)}_{kk'}R^{(n)}_{ll'} \tag{92}$$

so that

$$C^{(1)}=P^{(1)}C^{ZB}\ , \quad C^{(2)}=P^{(2)}C^{ZB} \tag{93}$$

Since the average $\epsilon_{ij}=(\epsilon^{(1)}_{ij}+\epsilon^{(2)}_{ij})/2$ is the macroscopic strain and it is straightforward to verify that

$$\bar{C}^{WZ}=\frac{1}{2}\left(C^{(1)}+C^{(2)}\right)=\frac{1}{2}\left(P^{(1)}+P^{(2)}\right)C^{ZB} \tag{94}$$

has the correct C_{6v} symmetry, one would rashly presume that equation (94) is the relation we are looking for. However, as pointed out by R.H. Martin [80], for a elastic strain the tetrahedra can not be considered independent - the corner of neighboring tetrahedra are firmly attached so that the response of each to external force is not independent. R.H.Martin tackled this problem by adjusting the internal strain

$$\delta_{ij}=\frac{1}{2}\left(\epsilon^{(1)}_{ij}-\epsilon^{(2)}_{ij}\right) \tag{95}$$

so as to minimize the total strain energy in the crystal

$$U=\frac{1}{4}\left(\epsilon_{ij}^{(1)}C_{ijkl}^{(1)}\epsilon_{kl}^{(2)}+\epsilon_{ij}^{(2)}C_{ijkl}^{(2)}\epsilon_{kl}^{(2)}\right)$$
$$=\frac{1}{2}\left(\epsilon_{ij}\bar{C}_{ijkl}^{WZ}\epsilon_{kl}+\delta_{ij}\bar{C}_{ijkl}^{WZ}\delta_{kl}+\epsilon_{ij}\Delta_{ijkl}\delta_{kl}+\delta_{ij}\Delta_{ijkl}\epsilon_{kl}\right) \quad \textbf{(96)}$$

where Δ is the difference

$$\Delta=\frac{1}{2}\left(C^{(1)}-C^{(2)}\right)=\frac{1}{2}\left(P^{(1)}-P^{(2)}\right)C^{ZB} \quad \textbf{(97)}$$

Solution of $\partial U/\partial\delta_{ij}=0$ yields

$$\delta=-\left(\bar{C}^{ZB}\right)^{-1}\Delta\epsilon \quad \textbf{(98)}$$

and therefore

$$U=\frac{1}{2}\epsilon C^{WZ}\epsilon \quad \textbf{(99)}$$

with

$$C^{WZ}=\bar{C}^{WZ}-\Delta\left(\bar{C}^{WZ}\right)^{-1}\Delta \quad \textbf{(100)}$$

$(\overline{C}^{WZ})^{-1}$ should be understood in the sense that $\overline{C}^{WZ}$ can be viewed as a matrix with indices ij run through the row index and kl run through the column index. From equations (94) and (97) we have

$$C^{ZB}=\left(P^{+}\right)^{-1}\bar{C}^{WZ} \quad \textbf{(101)}$$

and

$$\Delta = P^{-} C^{ZB} = P^{-} (P^{+})^{-1} \bar{C}^{WZ} \tag{102}$$

where

$$P^{\pm} = \frac{1}{2}\left(P^{(1)} \pm P^{(2)}\right) \tag{103}$$

and $(P^{+})^{-1}$ should be understood in the same way as $(\bar{C}^{WZ})^{-1}$ is. Substitution of equation (102) into equation (100) yields

$$\bar{C}^{WZ} = C^{WZ} + \left[P^{-} (P^{+})^{-1} \bar{C}^{WZ}\right]^{T} (\bar{C}^{WZ})^{-1} \left[P^{-} (P^{+})^{-1} \bar{C}^{WZ}\right] \tag{104}$$

Equation (104) can be straightforwardly evaluated for $\bar{C}^{WZ}$ by iteration using the known C^{WZ} as starting value for $\bar{C}^{WZ}$. Finally the elastic tensor for Zinc-Blend Structure may be evaluated using equation (101).

§ 4-6 Three-Band Envelope Function Model for Strained-Layer Heterostructures

In the absence of strain the hamiltonian for a constituent material in a heterostructure is (see § 4-1)

$$\hat{H}_0 = \frac{\hat{p}^2}{2m_0} + V_0(r_L) \tag{105}$$

When strained, the perturbed hamiltonian is

$$\hat{H}=\frac{\hat{p}^2}{2m_0}+V(r_E) \tag{106}$$

As required by the envelope function model and perturbation theory, the perturbation $V(\mathbf{r})-V_0(\mathbf{r})$ has to be small and slowly varying on the scale of the host lattice periodicity. But in a strained layer $V(\mathbf{r})-V_0(\mathbf{r})$ is not guaranteed to vary slowly and can be very large at certain points due to the change in the atomic positions. To overcome this difficulty, Bir and Pikus [67] made a change of coordinates for the perturbed problem from Euler coordinates $\mathbf{r}_E$ to Lagrange $\mathbf{r}_L$ ones

$$r_E=(I+\epsilon)r_L \tag{107}$$

Hence the periodicity of $\hat{H}_0$ is restored for $\hat{H}$ and for a given function $f_E(\mathbf{r}_E)=f_L(\mathbf{r}_L)$, we have

$$\hat{p}_L f_L=(I+\epsilon)\hat{p}_E f_E \tag{108}$$

The $\mathbf{k}$ space coordinates should also change accordingly

$$k_L=(I+\epsilon)k_E \tag{109}$$

For a strained-layer heterostructure grown along the $<001>$ orientation the Kane matrix element $<S \mid \hat{p}_z \mid Z>$ becomes

$$P' = (1-\epsilon_{zz})P_0 \tag{110}$$

where P_0 is the Kane matrix element for the unstrained material. According to equation (109)

$$k_z' = (1-\epsilon_{zz})k_z \tag{111}$$

A three-band Kane model description of the strained layer yields the light particle dispersion relation along z direction

$$\begin{aligned}&(E-E_c-\delta E_c)\left[(E-E_v+\delta E_{H,v}-\delta E_s)(E-E_v+\Delta+\delta E_{H,v})-2(\delta E_s)^2\right]\\&=(1-\epsilon_{zz})^4 P_0^2\hbar^2 k_z^2\left[E-E_v+\frac{2}{3}\Delta+\delta E_{H,v}-\delta E_s\right]\end{aligned} \tag{112}$$

where $\delta E_{H,c}$, $\delta E_{H,v}$ and δE_s are defined as in § 4-3.

Following similar procedure to unstrained case in § 4-2 and taking into account the strain effect discussed in § 4-3 and all the considerations discussed here, we find the equations for allowed states in strained-layer superlattice and single well to be

$$\begin{aligned}&\cos(k_a L_a)\cosh(k_b L_b)+\frac{1}{2}\left[\eta-\frac{1}{\eta}\right]\sin(k_a L_a)\sinh(k_b L_b)=\cos(qd)\\&\cos(k_a L_a)+\frac{1}{2}\left[\eta-\frac{1}{\eta}\right]\sin(k_a L_a)=0\end{aligned} \tag{113}$$

which has the exact same form as the unstrained case except for the expression of η and the dispersion relation in each constituent material

$$\eta=\frac{\left(1+\epsilon_{zz}^{a}\right)k_a m_b^{*}(E)}{\left(1+\epsilon_{zz}^{b}\right)k_b m_a^{*}(E)} \tag{114}$$

$m^*_a(E)$ and $m^*_b(E)$ are defined by dispersion relation and the equation

$$E=\frac{\hbar^2 k^2}{2m^{*}}+E_i' \tag{115}$$

where E'_i is the *i*th band edge after the strain is considered. For light particles the dispersion relation is given in equation (112). Heavy hole band remains decoupled from light particles at $k_{\pm}=0$. So the only strain effect on heavy hole is the band edge shift given in § 4-3.

§ 4-7 Sample Calculations and discussion

1. *CdTe/$Cd_{1-x}Zn_xTe$ Single Quantum Wells:*

The samples I studied were grown by molecular-beam epitaxy (MBE) on <001> semi-insulating GaAs substrates [81]. The structures consist of a 4μm thick $Cd_{1-x}Zn_xTe$ ($x=0.098\sim0.64$) buffer layer; a CdTe single quantum well of 13Å ~ 75Å; and a 0.5μm thick $Cd_{1-x}Zn_xTe$ cap layer. The buffer layer is much thicker than its critical thickness so that the strain between the substrate and buffer is relaxed. The quantum well layer is

much thinner than both buffer and cap layers. Therefore it is quite reasonable to assume that only the quantum well layer is under biaxial compression strain $\epsilon(x)$

$$\epsilon(x)=\frac{a(x)-a_{CdTe}}{a_{CdTe}} \tag{116}$$

Substituting $a(x)=a_{CdTe}(1-x)+a_{ZnTe}x$ into equation (116) gives

$$\epsilon(x)=\left[\frac{a_{ZnTe}-a_{CdTe}}{a_{CdTe}}\right]x \tag{117}$$

Note that free standing lattice and minimum strain energy principle would give same numerical result as equation (117).

All the interested band edges in CdTe layer are calculated by equation (80) in § 4-3, with strain dependent of composition x in the barrier layer. Since there is no noticeable biaxial strain in the barrier layers all the band edges in the question should be interpolated according the scheme outlined in § 4-4

$$\begin{cases} E_{vav}(x)=(1-x)E_{vav}(CdTe)+xE_{vav}(x)+3x(1-x)\left[a_v(CdTe)-a_v(ZnTe)\right]\dfrac{\delta a_0}{a(x)} \\ \Delta(x)=(1-x)\Delta(CdTe)+x\Delta(ZnTe) \\ E_g(x)=(1-x)E_g(CdTe)+xE_g(ZnTe)+bx(1-x) \\ E_v(x)=E_{vav}(x)+\dfrac{\Delta(x)}{3} \\ E_c(x)=E_v(x)+E_g(x) \\ E_{so}(x)=E_{vav}(x)-\dfrac{2\Delta(x)}{3} \end{cases} \tag{118}$$

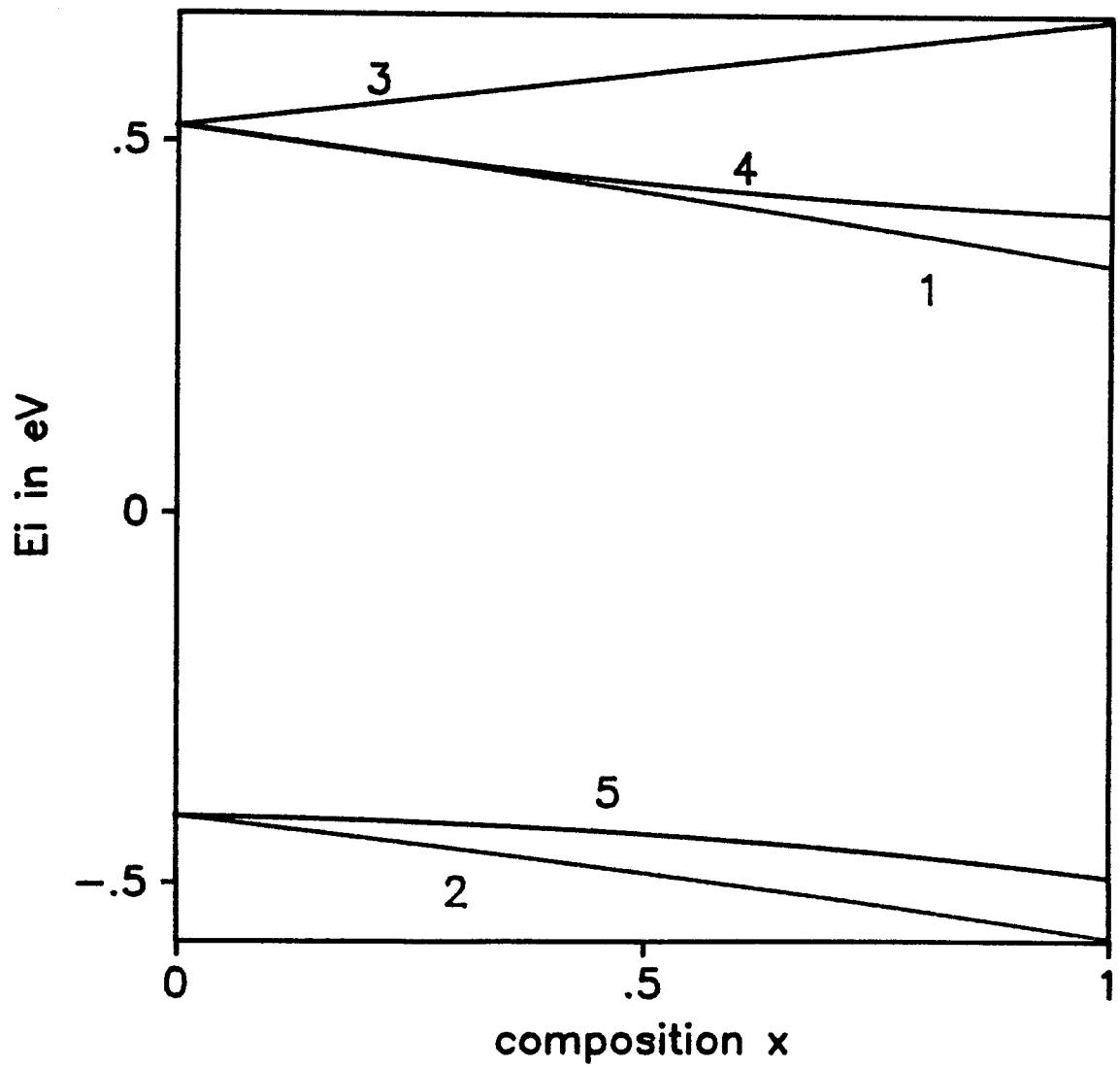

Figure. 6A. Valence band edges in $CdTe/Cd_{1-x}Zn_xTe$ strained-layer single quantum well as functions of barrier composition x. Curve 1 and 2 are the E_v and E_{so} edges in the barrier. Curve 3,4 and 5 are the E_{hh}, E_{lh} and E_{so} edges in the well.

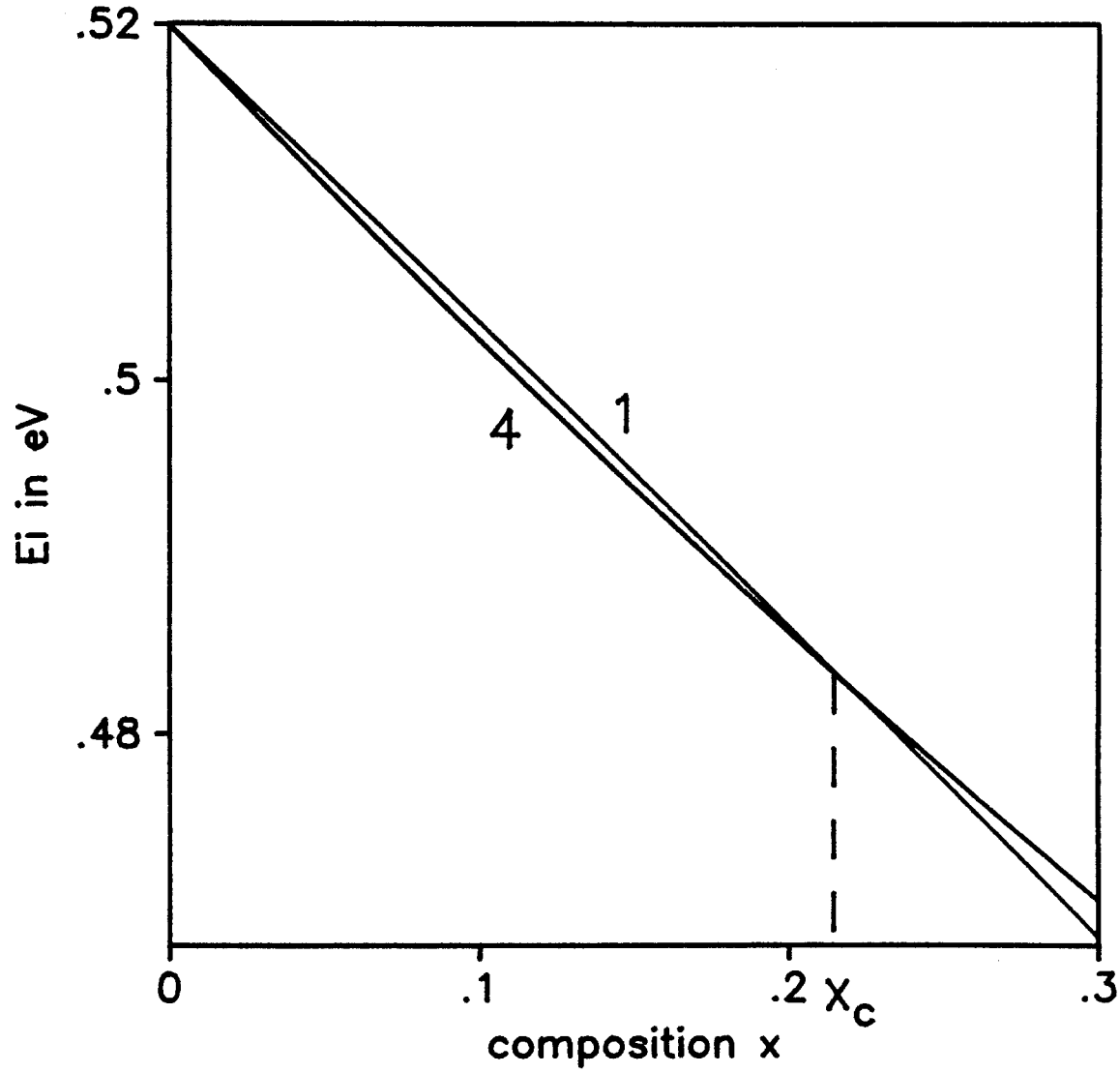

Figure. 6B. Crossing of E_{lh} in the well and E_v in the barrier at composition x_c.

Figure 6 plots the quantum well's E_{lh}, E_{hh}, E_{so} and the E_v, E_{so} in the barrier layers as functions of barrier composition x. Table 3 lists all the parameters used for calculation. Note the anti-crossing behavior of E_{lh} and E_{so}, which is due to the coupling between them by the strain hamiltonian. The valence band edge E_v in the barrier, however, does cross E_{lh} of well layer at x=Xc. Thus the band lineup for light hole is type I for x < Xc and type II for x > Xc. The simple model used before [82] would fail to predict the anti-crossing feature and the type transition of the light hole band lineup.

For the sample group with x=0.21, the strain amounts $\epsilon(x)=1.22\%$ and the band lineup calculated is shown in figure 7. As one can see in the figure light hole is not confined. The confined heavy hole and electron levels are calculated by equation (113)-(115) in § 4-6. The results for well width x=0 ~ 100Å are plotted in figure 8 and figure 9. Figure 8 plots the calculated optical gap (E_{1e} - E_{1h}) and the experimental value of the free exciton (1e - 1h) transition energy as functions of well width L_w. The differences between the calculated optical gaps and experimental points (▲) are taken as binding energies of the free excitons (E_{bx}). As predicted by theoretical calculation [101-104], E_{bx} first increases with decreasing well width well width l_w because of the tendency to a two-dimensional behavior and the beyond certain point, E_{bx} decreases due to the recovery of a three-dimensional behavior through the increasing penetration of electron and hole wave function into the barrier. This trend is schematically illustrated in figure 9.

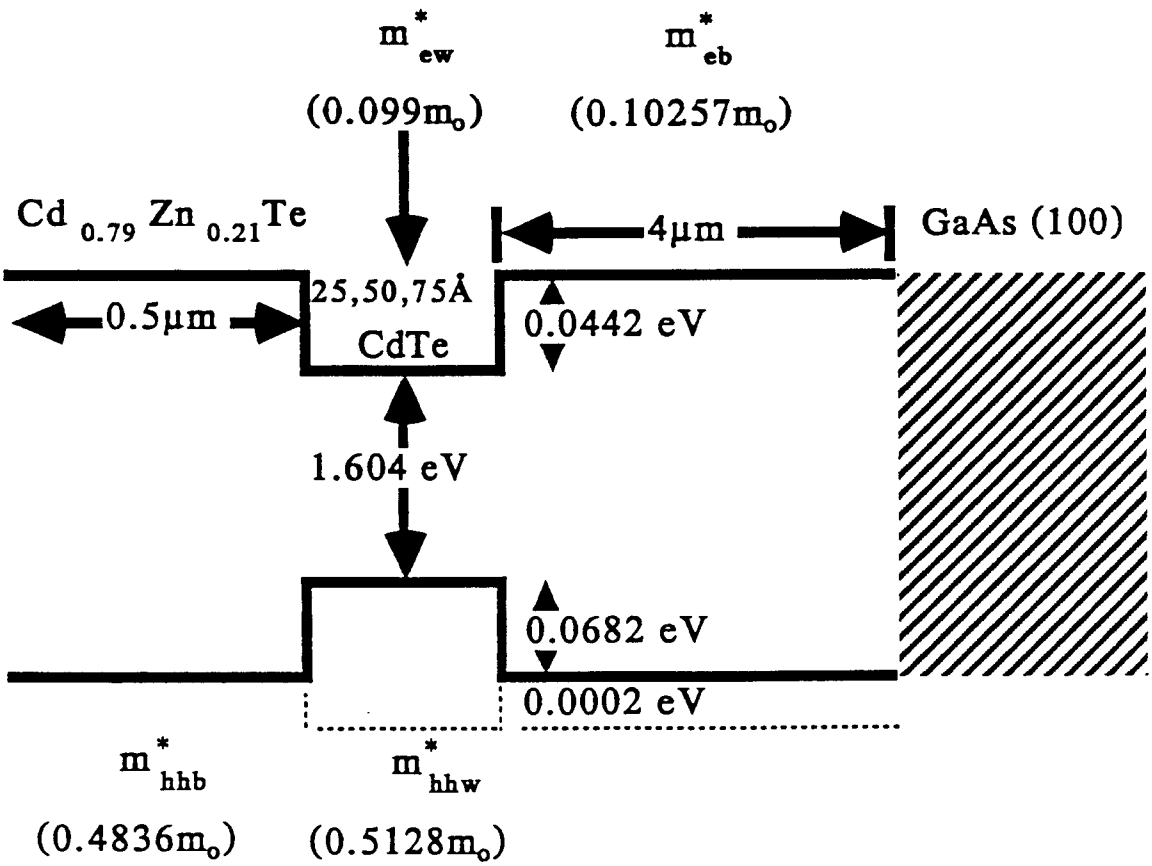

Figure. 7. The band lineup of the strained-layer CdTe/$Cd_{0.79}Zn_{0.21}Te$ single quantum well.

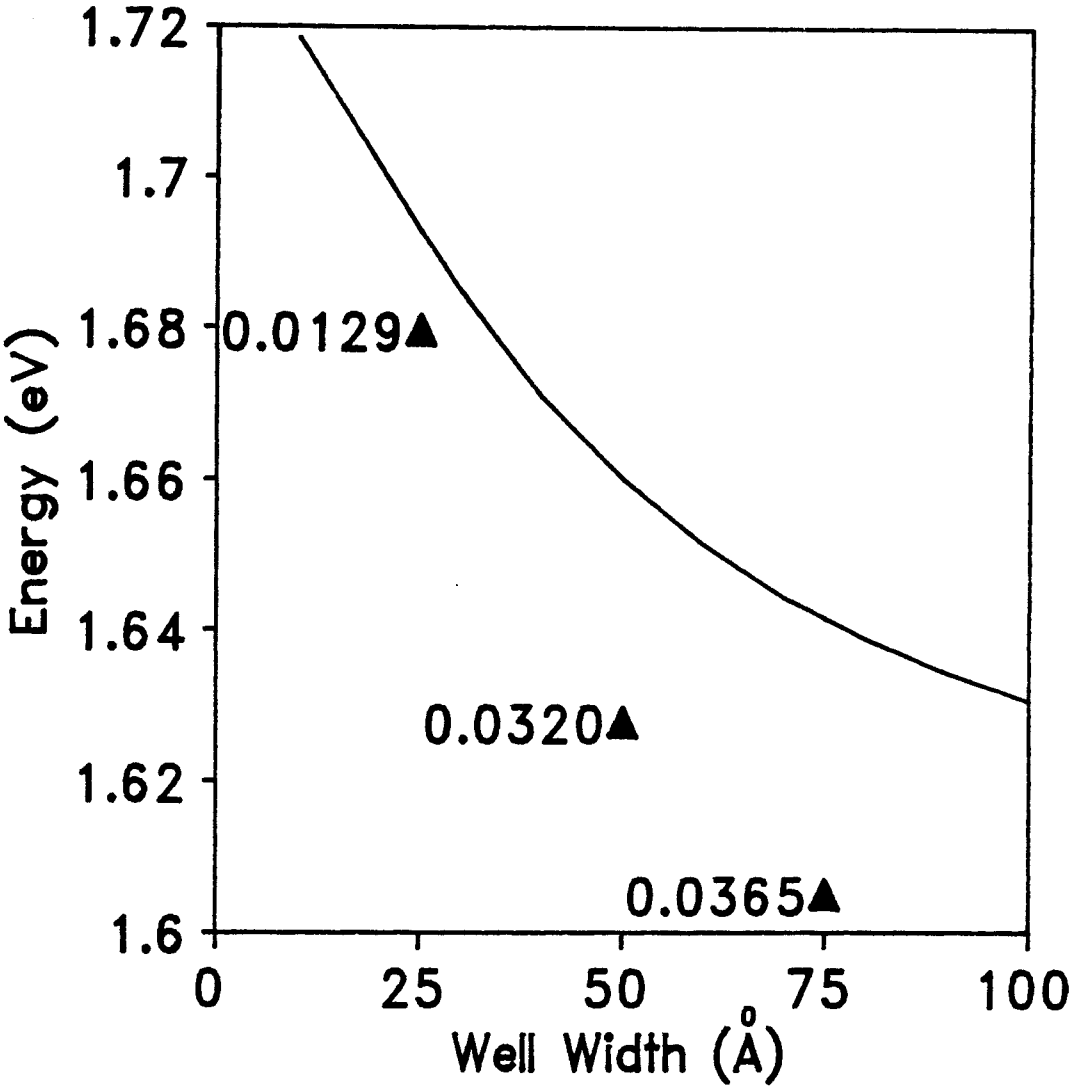

Figure. 8. The exciton transition energies as a function of well width. Solid line shows the calculated transition energies (1e-1h), and ▲ represents the experimental points. The numbers beside the experimental data are the differences between the calculated and measured data in eV.

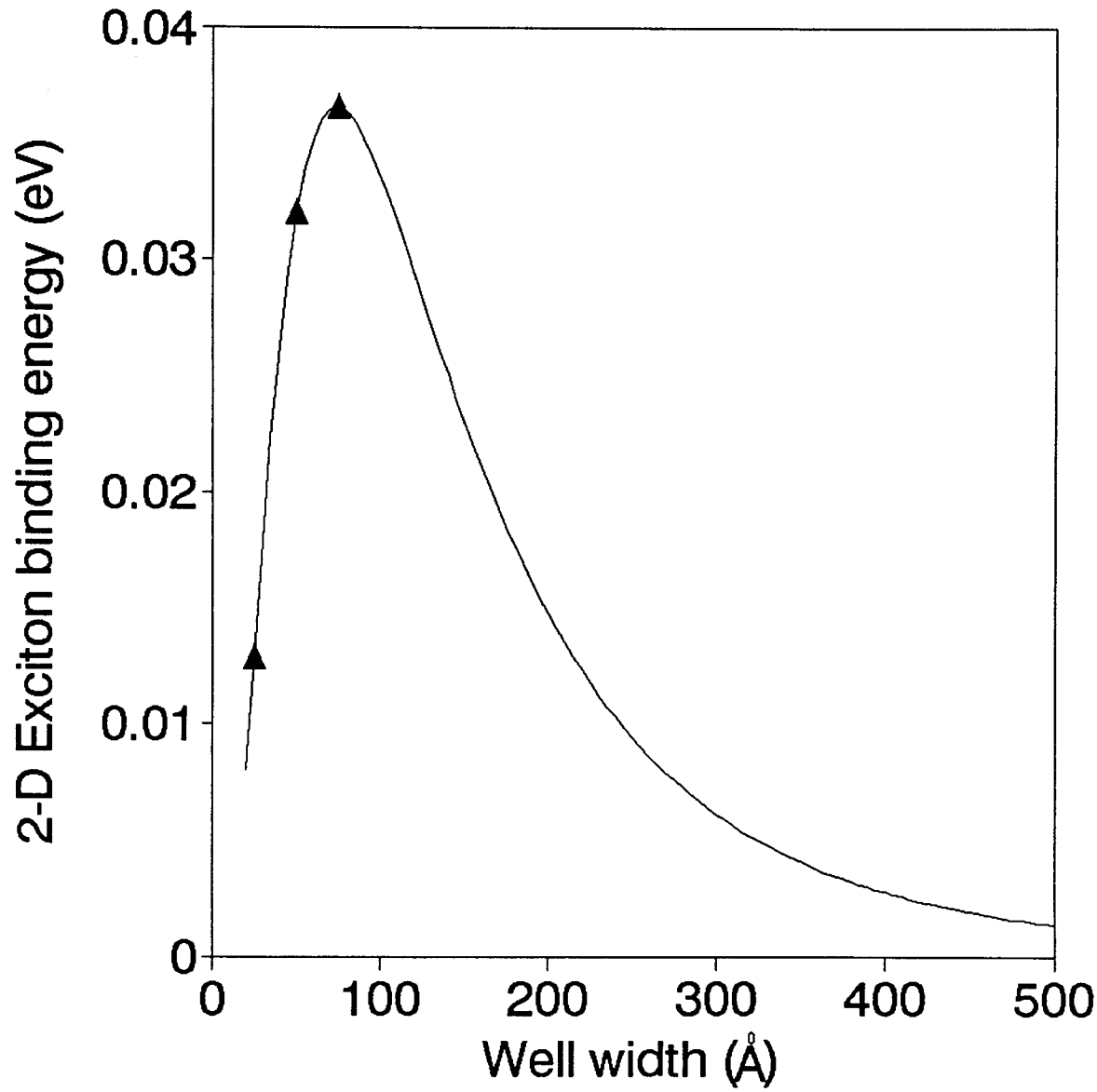

Figure.9. Exciton binding energy for $CdTe/Cd_{0.79}Zn_{0.21}Te$ strained-layer single quatum wells as a function of well width. Experimental value for well widths 25Å, 50Å and 75Å are shown by ▲. The solid line sketch the trend predicted in reference [101].

The three-dimensional (3-D) exciton binding energy given in [105] are 12 meV for CdTe and 13 meV for ZnTe. For the 75Å thick CdTe quantum well sample in this study, the value of E_{bx} is estimated to be about three times larger (36.5 meV) than that of 3-D exciton. In reference [106], the E_{bx} for a 50Å thick CdTe quantum well sample is also reported to be more than two time larger (25 meV) than that of 3-D exciton. The main difference between the samples used here and reference [106] is the barrier Zn composition x. In the samples used here, x is 0.21 while in reference [106] x is only 0.08. A larger x can have two effects. First, a larger x gives a wider band gap in the barrier layer and hence a higher potential barrier. Second, a larger x in the barrier causes larger strain in the well, pushing both electron and heavy hole well deeper. Both of these effects enhance the two-dimensional (2-D) feature of the exciton in the quantum well, enlarging the binding energy E_{bx}. The accuracy in the deduced E_{bx} value is dependent on the precision of parameters such as deformation potentials a_c, a_v, b and elastic constants C_{11}, C_{12} used for calculations. Different values for these parameters have been used in literature [107-113].

Tabl 3. Parameter values used for calculations. $E_g=1.606+0.494x+0.294x^2$(eV) (calculated using Hill's theory), $a(Cd_{1-x}Zn_xTe)=6.481-0.3773$(Å) [112], $m_c^*(Cd_{1-x}Zn_xTe)=0.099+0.017x$, $\gamma_1(Cd_{1-x}Zn_xTe)=4.11-0.04x$, $\gamma_2(Cd_{1-x}Zn_xTe)=1.08-0.3x$ [109]

	E_g [112] (eV)	Δ [113] (eV)	a_v [113] (eV)	a_c [113] (eV)	b [113] (eV)	a_0 [113] (eV)	C_{11} [113] (eV)	C_{12} [113] (eV)	E_{vav} * (eV)
ZnTe	2.394	0.91	0.79	-5.83	-1.26	6.1037	0.713	0.407	+0.03
CdTe	1.606	0.93	0.55	-3.96	-1.10	6.481	0.562	0.394	+0.21

*Relative to the top of GaAs valence band given HAO theory [69].

Chapter Five

Experimental Work

§ 5-1 Principle of Optical Orientation Measurement

Optical orientation (or optical pumping) measurements have been a very useful tool in physical, chemical and biochemical research [83,84,85] because of its sensitivity, selectivity and accuracy. In the field of semiconductor heterostructure research, due to the selection rules and conservation of angular momentum, the polarization dependence of optical transition is well established. Figure 10 shows the selection rules and relative intensities for transitions between different states [86]. With these selection rules optical orientation measurement can help to identify the states involved in optical transitions. In this section I describe a computerized setup for optical orientation measurement. This setup consists of a photo-elastic modulator (PEM) whose retardation phase can be kept constant even when the wavelength of the modulated light is scanned over a wide range, and a dual channel gated photon counter which can compensate the variation of excitation intensity with time and wavelength. Unlike conventional lock-in or other analog setups, where the difference of two perpendicularly polarized light components (AC) and the average of these components (DC) are extracted electronically and the ratio AC/DC is recorded as degree of polarization, this spectropolarimeter directly records the σ^+ and

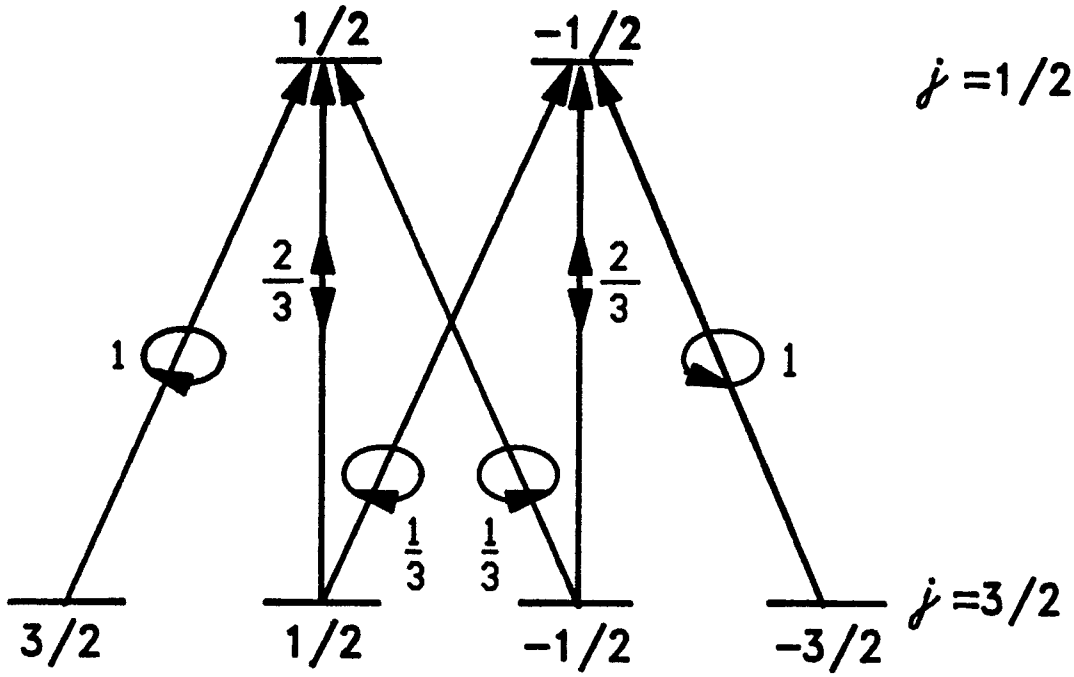

Figure. 10. Selection rules for optical transitions and relative intensities.

σ^- components (for circular polarization) or $I_\parallel$ and $I_\perp$ components (for linear polarization) of the analyzed light signal in the same run of wavelength, temperature, etc. The spectra of the two components are stored as a numerical file in a computer and can be further processed to extract the degree of polarization as a function of wavelength, temperature, etc.

The circular or linear polarization of an optical signal can be analyzed by inserting a $\lambda/4$ retarder and a linear polarizer (or, for linear polarization, simply a linear polarizer) between the source and the detector. To measure the degree of circular polarization, one alternately sets the linear polarizer +45° and -45° with the fast axis of the retarder so that σ^+ and σ^- components of the signal can be detected alternately. For linear polarization, the retarder is removed and the linear polarizer is set +45° and -45° to the horizontal so that $I_\parallel$ and $I_\perp$ can be measured alternately. The degree of polarization is defined as

$$\rho = \frac{I^+ - I^-}{I^+ + I^-} \tag{119}$$

For circular polarization, I^+ is the intensity of right-hand circular polarization (σ^+) and I^- is the intensity of left-hand circular polarization (σ^-). For linear polarization, I^+ and I^- stand for the beam polarized along the +45° and -45° axes respectively. The automatic spectropolarimeters utilizing the mechanically rotating polarizer and analog lock-in techniques are described in many publications [87,88]. There are two main drawbacks

of this technique. First, the response of devices such as the monochromator's grating and the photomultiplier depends on the polarization of the incoming light, and this can induce error in the measured degree of polarization. The second is the non-achromaticity of the retarder. To overcome these limitations, a fixed analyzer and a modulated retarder are put in series with their optical axes 45° apart. The retardation is modulated such that the retardance A is a function of time given by

$$A=A_0\sin(2\pi ft) \tag{120}$$

where A_0 is proportional to the driving voltage and f is the modulation frequency. Now that a fixed analyzer is used, the photomultiplier as well as the grating of the monochromator are exposed to only one state of linear polarization and hence the dependence of their response on the polarization of incoming light has no effect on the accuracy of the measurements. To assure a constant retardation for different wavelengths, an electronic compensation system was designed. Figure 11 illustrates the heart of this setup. In literature the transmission of optical signal through this series of components is analyzed with either Mueller [89] or Jones [90] matrix. But for the purpose here, they have no significant advantages other than an elegant mathematical form. Therefore the standard electromagnetic field complex vector analysis given in text books [91] is followed here. Without loosing generality, let's assume that the incident beam's electric (E) vector has the form

$$\boldsymbol{E}=a\boldsymbol{i}+b\boldsymbol{j} \tag{121}$$

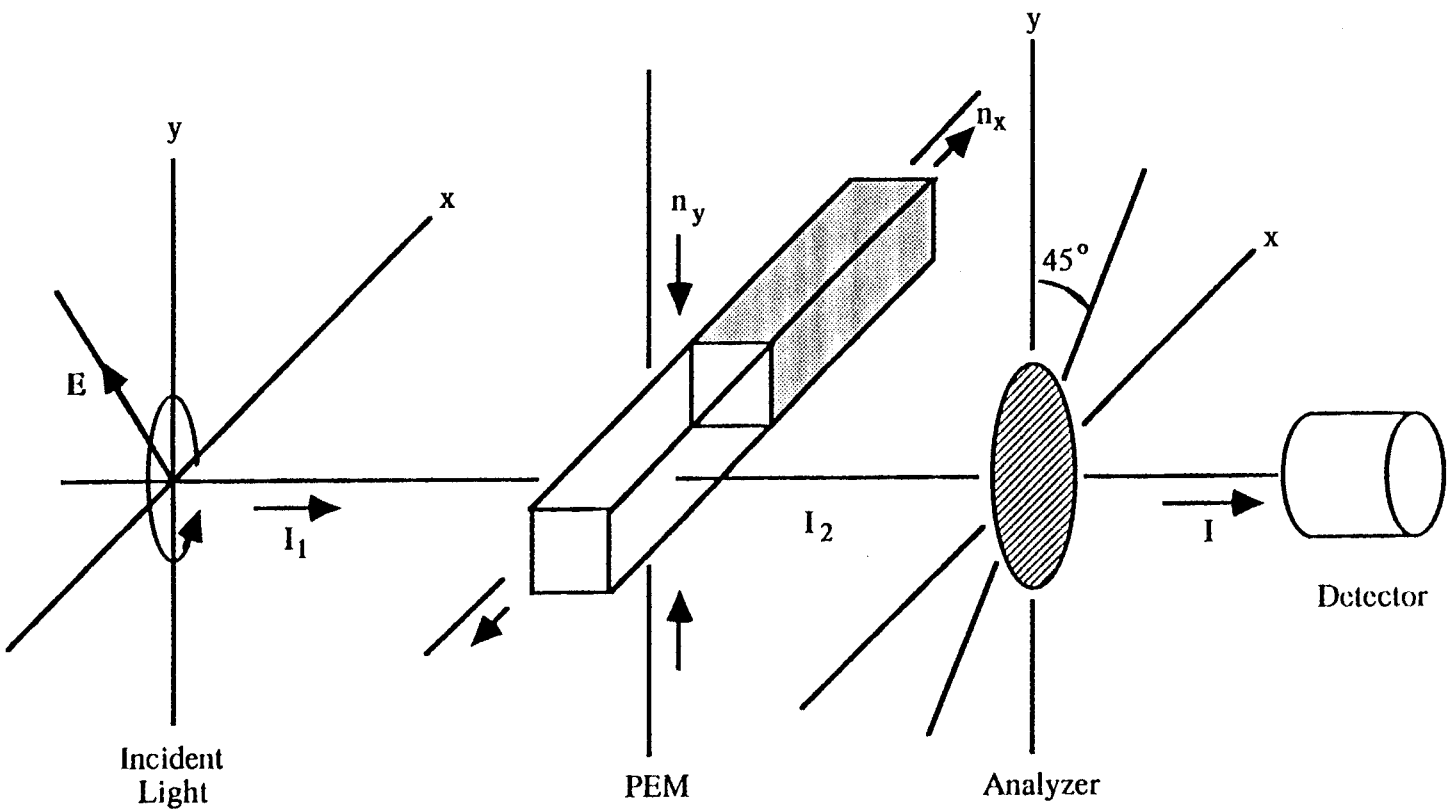

Figure. 11. Basic setup for analyzing the circular polarization of light. I_1 and I_2 are intensities of the light before and after the modulator, respectvely. I is the intensity seen by the detector. n_x and n_y are the refraction indices in the x and y directions.

where **i** and **j** are the unit vectors along the x and y axes. The factor $e^{-i\omega t}$ is dropped from equation (121). With different a and b, E can be elliptically, circularly or linearly polarized. After passing through the photo-elastic modulator (PEM), the wave becomes

$$E' = aie^{+\frac{iA}{2}} + bje^{-\frac{iA}{2}} \tag{122}$$

where A is the retardance given in equation (120). With the analyzer's passing axis at 45°, the final transmitted wave can be written as

$$E'' = \frac{1}{\sqrt{2}}(i+j)\cdot E' \frac{1}{\sqrt{2}}(i+j) \tag{123}$$

and the transmitted intensity is

$$I'' = \frac{1}{2}\left|ae^{+\frac{iA}{2}} + be^{-\frac{iA}{2}}\right|^2 \tag{124}$$

where the proportionality factor $(\epsilon/\mu)^{1/2}$ between I and E is dropped.

Circular Polarization:

For σ^+, substitution of b=ia and equation (120) into equation (124) gives

$$\begin{aligned} I^{+//} &= \frac{|a|^2}{2}\left(e^{+\frac{iA}{2}} + ie^{-\frac{iA}{2}}\right)\left(e^{-\frac{iA}{2}} - ie^{+\frac{iA}{2}}\right) \\ &= |a|^2(1+\sin A) \\ &= |a|^2\left[1+\sin(A_0 2\pi ft)\right] \end{aligned} \tag{125}$$

for σ^-, b=-ia and we have

$$I^{-//} = |a|^2 \left[1 - \sin(A_0 \sin 2\pi ft)\right] \tag{126}$$

To see I^+ and I^- alternately at a given wavelength, the driving voltage is chosen to make $A_0 = \pi/2$. Hence the PEM acts like a $+\lambda/4$ and $-\lambda/4$ plate alternately. Letting $A_0 = \pi/2$ in equations (125) and (126) we get

$$I^{+//} = |a|^2 \left[1 + \sin\left(\frac{\pi}{2}\sin 2\pi ft\right)\right] \tag{127}$$

$$I^{-//} = |a|^2 \left[1 - \sin\left(\frac{\pi}{2}\sin 2\pi ft\right)\right] \tag{128}$$

Figure 12 shows the plots of equations (127) and (128). It is clear from Figure 12 that equations (127) and (128) have symmetric features and if the photon counters A and B are gated as shown in the Figure, the degree of polarization becomes

$$\rho \approx \frac{A-B}{A+B} \tag{129}$$

Linear Polarization:

For an incident beam linearly polarized along +45° to vertical, a=b and equation (124) becomes

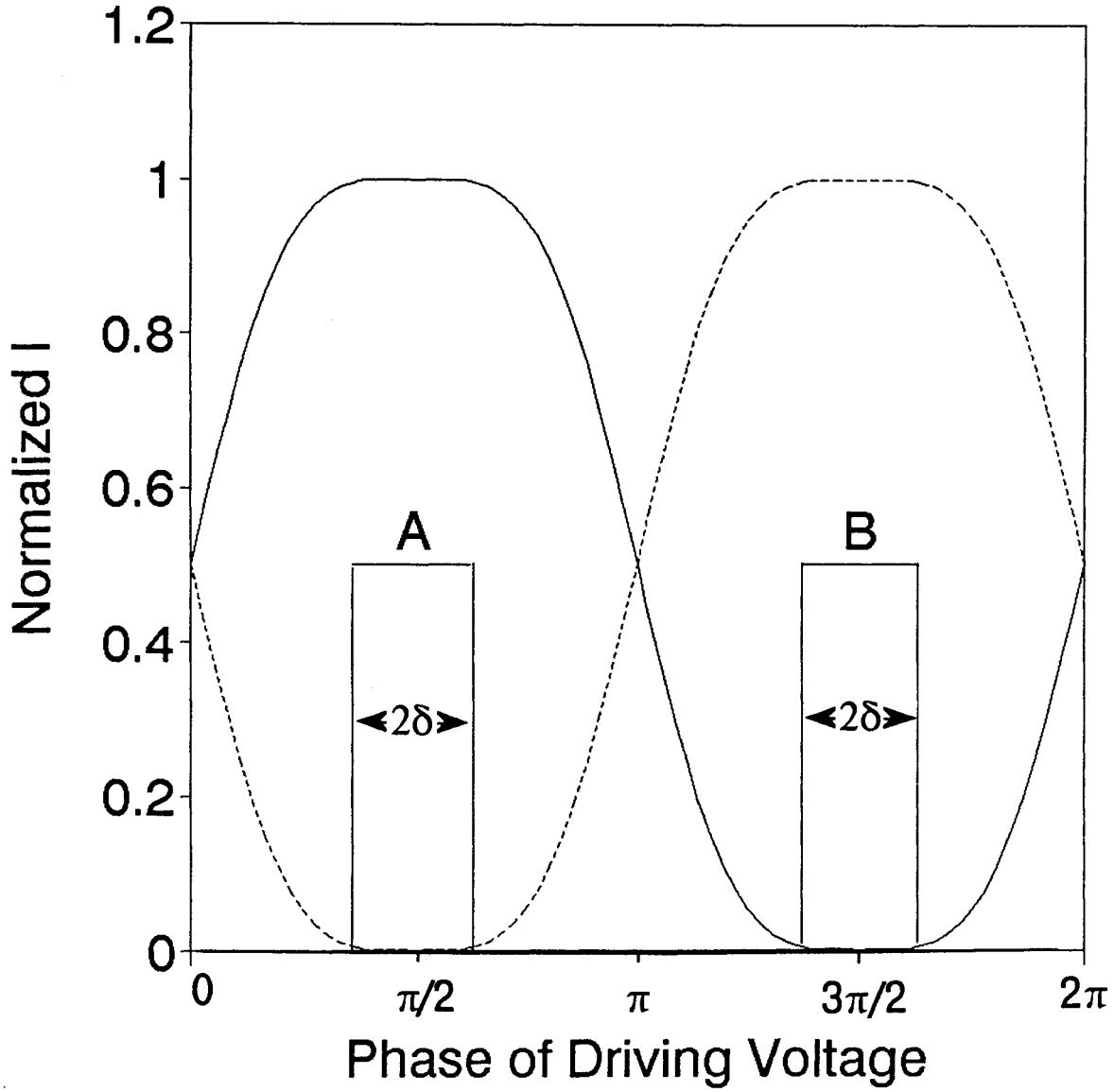

Figure. 12. The theoretical response of the PEM-analyzer system to circularly polarized light. The solid line is for σ^+ and the dashed line is for σ^-, and 2δ is the gate width for the counters A and B.

$$I^{+//} = |a|^2 \left[1+\cos(A_0 \sin 2\pi ft)\right] \tag{130}$$

similarly, for an incident beam linearly polarized along -45° to vertical, a=-b and we have

$$I^{-//} = |a|^2 \left[1-\cos(A_0 \sin 2\pi ft)\right] \tag{131}$$

As we know, a half wave retardation rotates a beam linearly polarized along +45° to an one linearly polarized along -45° and vice versa. Therefore, the driving voltage may be controlled to make $A_0=\pi$ so that the PEM acts as a $+\lambda/2$ and $-\lambda/2$ retarder alternately. Substitution of $A_0=\pi$ into equations (130) and (131) yields

$$I^{+//} = |a|^2 \left[1+\cos(\pi \sin 2\pi ft)\right] \tag{132}$$

$$I^{-//} = |a|^2 \left[1-\cos(\pi \sin 2\pi ft)\right] \tag{133}$$

The plots of equations (132) and (133) are shown in Figure 13, which clearly shows the rather asymmetric feature. In the conventional lock-in technique, additional electronic circuits are needed to process this asymmetric wave form, which also requires that the PEM be switched on and off (enabled and disabled) from time to time [85]. In the system discussed here, this marked asymmetry is dealt with numerically.

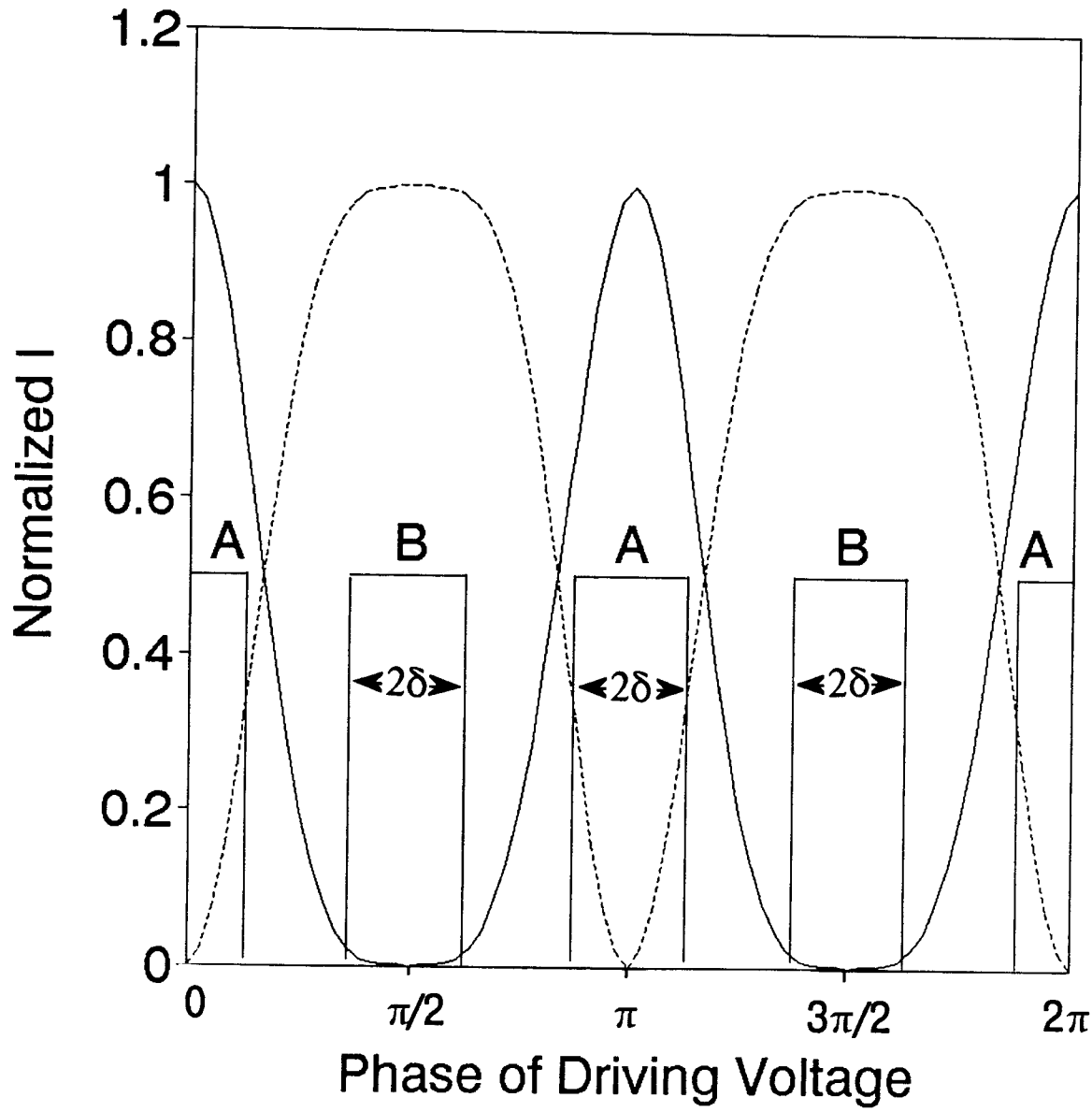

Figure. 13. The theoretical response of the PEM-analyzer system to linearly polarized light. The solid line is for I(+45°), the dashed line is for I(-45°), and 2δ is the gate width for the counters A and B.

Suppose that photon counters A and B are gated as shown in Figure 13 and the incident beam has two components I^+ (polarized along +45°) and I^- (polarized along -45°). From equations (121), (132) and (133) the counts in A and B are written as

$$A=\eta_A\left\{\frac{1}{2}I^+\int_{\pi-\delta}^{\pi+\delta}[1+\cos(\pi\sin x)]dx+\frac{1}{2}I^-\int_{\pi-\delta}^{\pi+\delta}[1-\cos(\pi\sin 2\pi ft)]dx\right\} \quad (134)$$

$$B=\eta_B\left\{\frac{1}{2}I^+\int_{\frac{\pi}{2}-\delta}^{\frac{\pi}{2}+\delta}[1+\cos(\pi\sin 2\pi ft)]dx+\frac{1}{2}I^-\int_{\frac{\pi}{2}-\delta}^{\frac{\pi}{2}+\delta}[1-\cos(\pi\sin 2\pi ft)]dx\right\} \quad (135)$$

where 2δ is the gate width, and η_A and η_B are effective system efficiencies which account for the transmissivity of the monochromator, the efficiency of the photomultiplier, the gain of preamplifier and counter's threshold. Since counters A and B count the signal from the same detecting system (monochromator, photomultiplier, and preamplifier), and if their thresholds are matched

$$\eta_A=\eta_B=\eta \quad (136)$$

Normally what we are interested in is the ratio of the signal; so in the following I am going to drop this factor η. Using the parity of the function cos(πsinx) and ignoring η, equations (134) and (133) can be written as

$$A=\delta(I^++I^-)+\alpha(I^+-I^-) \quad (137)$$

$$B=\delta(I^{+}+I^{-})+\beta(I^{+}-I^{-}) \tag{138}$$

where

$$\alpha=\int_{\pi}^{\pi+\delta}\cos(\pi\sin x)dx \tag{139}$$

$$\beta=\int_{\frac{\pi}{2}}^{\frac{\pi}{2}+\delta}\cos(\pi\sin x)dx \tag{140}$$

According to equations (139) and (140), it can be readily verified that for $0<\delta\leq\pi/4$, $\alpha>0$ and $\beta<0$. This assures that

$$\begin{vmatrix}\delta & \alpha\\ \delta & \beta\end{vmatrix}\neq 0 \tag{141}$$

Therefore, equations (137) and (138) have a definite solution which yields

$$\rho=\frac{I^{+}-I^{-}}{I^{+}+I^{-}}=\frac{\begin{vmatrix}\delta & A\\ \delta & B\end{vmatrix}}{\begin{vmatrix}A & \alpha\\ B & \beta\end{vmatrix}} \tag{142}$$

Since $A>0$, $B>0$ and $\alpha\beta<0$

$$\begin{vmatrix}A & \alpha\\ B & \beta\end{vmatrix}\neq 0 \tag{143}$$

Equations (139) and (140) can be evaluated numerically for a given δ and above treatment for a whole spectrum scales to only a few lines of computer program.

Strictly speaking, similar treatment should be given to the circularly polarized case especially when the signal is weak and a wide gate is needed. In that case we get

$$\rho=\frac{\delta}{\gamma}\left[\frac{A-B}{A+B}\right] \tag{144}$$

where

$$\gamma=\int_{\frac{\pi}{2}}^{\frac{\pi}{2}+\delta}\sin\left[\frac{\pi}{2}\sin x\right]dx \tag{145}$$

When the signal is strong and δ can be very small, $\gamma\approx\delta$, equation (144) simplifies to equation (129).

§ 5-2 Instrumentation

1. *General Description of the Setup*

Figure 14 shows the block diagram of the apparatus setup. The monochromatic light from the Ar^+ ion laser (or Ti:Sapphire laser or dye laser pumped by Ar^+ laser), which is already linearly polarized by the Brewster output window, is retarded by $\lambda/4$

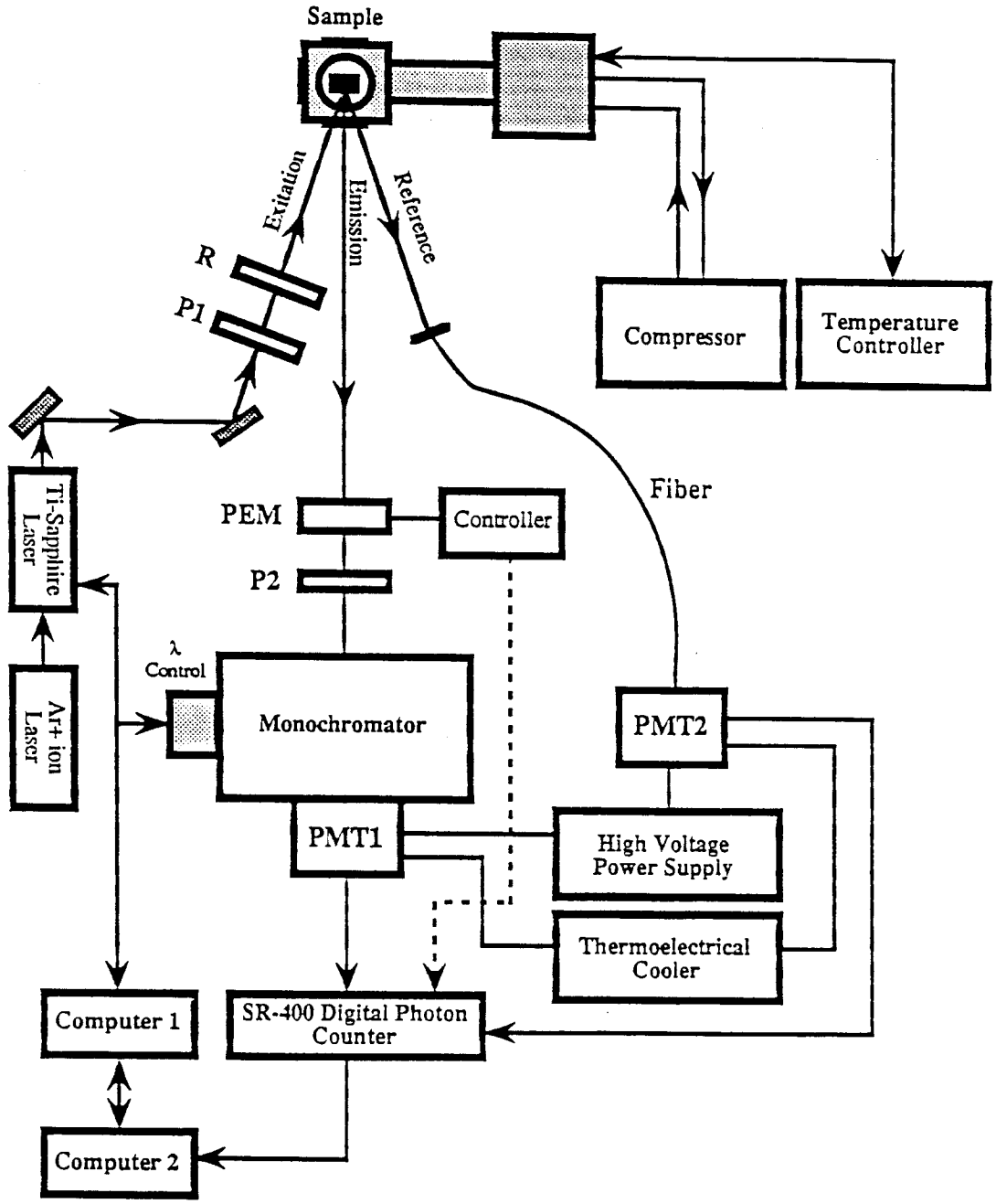

Figure. 14.Block diagram of the spectropolarimetaer. P1, P2 are linear polarizers, R is an achromatic λ/4 retarder. PEM is a photoelastic modulator, and PMT1 and PMT2 are photomultiplier tubes.

achromatic retarder (R) to get circularly polarized excitation light. For an experiment which requires linear polarization, the original laser beam and/or a $\lambda/2$ achromatic retarder can be used. If the excitation light is from a lamp, a monochromator and a linear polarizer (P1) are to be used in front of the quarter wave achromatic retarder (R). For a linearly polarized excitation light, the quarter wave retarder is removed and a half wave achromatic retarder is used to rotate the polarization plane. The samples are mounted in a closed cycle cold finger cryostat. Small angles between the excitation beam and the quantization axis of the sample, and between this latter and the direction of observation (detection) are preferred for circularly polarized optical pumping studies [92]. Different arrangement of the excitation beam and the sample's orientation have been used for linear polarization studies [93,94]. The emission (or optical signal such as transmission, reflection, etc.) from the sample is modulated by a photo-elastic modulator (PEM) whose modulation depth (retardance) is electronically controlled to follow the wavelength of the signal being measured. A second polarizer (P2) is used to analyze the modulated light. The light emerging from P2 is then dispersed by a monochromator and detected by a photomultiplier (PMT1). The electric signal from PMT1 is amplified by a fast preamplifier and then fed into a dual-channel gated photon counter which is capable of compensating the fluctuation of excitation intensity. To sense the variation of excitation intensity, the incident beam is split and coupled into a second photomultiplier (PMT2) through the optical fiber. The output of PMT2 is preamplified and then fed into photon counter to determine the counting period. The data acquisition and the scanning of (either excitation or detection) wavelength are synchronized and controlled by a PC computer.

The recorded spectra from both channels of the counter are stored as numerical files in computer for later processing.

2. *Components*

Excitation Source: A 10 Watt Laser Ionic, Model 553A Ar+ ion laser is used as an excitation source and to pump a Spectra Physics, Model 3900 CW Ti:Sapphire laser which has a tunable range of 675 nm - 1000 nm.

Polarizers: The linear polarizers used were Glan-Thompson polarizing prisms transmitting to the limit of the calcite λ=214nm to λ=2300nm and a maximum beam deviation of 2'30".

Quarter and half wave retarders: The Fresnel rhombs used here are Oriel products 25903 and 25907 respectively which are achromatic over the range of 450nm - 2000nm.

Cryostat: Samples are cooled by a closed cycle cold finger cryostat (RMC-Cryo-systems) controlled by a Cryogenic thermometer/controller (Palm Beach Cryophysics Inc., Model 4075).

Modulator: The photoelastic modulator used in this setup is a HIND's International Inc. product PEM-80/FS5 which has an effective aperture of 176 mm in diameter. The natural oscillation frequency of the modulator head (and hence the modulation frequency) is 50 KHz. The accuracy and stability of modulation frequency are $\pm 0.5\%$ and 0.1% respectively. The $\lambda/4$ retardation range is 180 - 2000 nm. The accuracy of peak-to-peak retardation is $\pm 2\%$. The modulator-analyzer train has an acceptance angle of $\approx 40°$ full-cone.

Monochromator: The monochromator in Figure 14 is a Jarrel-Ash 0.75m monochromator equipped with a 1180 groove/mm grating. A programmable spectrometer-driving system is used to control and scan the wavelength.

PMT and Amplifiers: The photomultipliers used are Hamamatsu PMT R928 ($185nm < \lambda < 950nm$) and R936 ($400nm < \lambda < 1200nm$). The PMTs are thermoelectrically cooled to $\approx$ -30°C to minimize the dark counts. The signal from PMTs is amplified by EG&G made fast preamplifier (Ortec 9301S) before being fed into photon counter.

Photon counting system: In SR-400 system, there are three fast counters: A, B, and T , all of which operate at rates up to 200 MHz. Counter T is presetable and determines the counting period for counters A and B which may be synchronized to external events via two independent gate generators. The gate generators provide gates from 5ns to 1s in duration with a delay from external trigger ranging from 25 ns to 1s. The counting

period is the time it takes the counter T to reach its preset count. If N_t is the preset count in counter T, and R_a, R_b, and R_t are the mean pulse rates of the inputs to counters A, B, and T, then the counting period is

$$\tau = \frac{N_t}{R_t} \tag{146}$$

The numbers of count in counters A and B will be

$$A = R_a \frac{N_t}{R_a} \tag{147}$$

$$B = R_b \frac{N_t}{R_t} \tag{148}$$

Since N_t is a constant in the above equations, the numbers of counts in counters A and B are proportional to the ration of the rates R_a/R_t and R_b/R_t respectively. If the input of counter T monitors the excitation intensity, the counting period will compensate the fluctuation in the excitation source.

Once counter T reaches its preset count, all the counters are "dwelled" and the computer is instructed to read the data and adjust the driving voltage of PEM as well as wavelength (depending on the application other parameters may be adjusted during the dwell time). When everything is stabilized, all counters are reset and the next counting period is initiated.

3. *Performance*

Figure 15 illustrates the test setup. The spectropolarimeter was tested using the 632.8nm He-Ne laser line which was 100% circularly polarized by the linear polarizer and the achromatic Fresnel rhomb. The plots in Figure 16 were recorded when the linear polarizer was set at +45° and -45° from the fast axis of the retarder (σ^+ and σ^-) and the gate of counter A is scanned with 0.2μs in gate width and delay increment. The solid (dashed) line shows the intensity of σ^+ (σ^-) circularly polarized beam versus the phase angle of the driving voltage. Similar test was also done for linearly polarized light and the results are plotted in Figure 17. It is clear that the experimental results in Figures 16 and 17 match the theoretical results shown in Figures 12 and 13.

As shown in Figure 18, the partially polarized light can be simulated by rotating the linear polarizer away from 45° to the fast axis of the retarder. The degree of polarization with a rotated angle ϕ can be written as

$$\rho=\frac{I^+-I^-}{I^++I^-}=\frac{\cos^2\phi-\sin^2\phi}{\cos^2\phi+\sin^2\phi} \qquad (-45°<\theta<+45°) \qquad \textbf{(149)}$$
$$=\cos 2\phi=\sin 2\theta$$

Equation (149) is valid for both circular and linear polarization. Partial linear polarization was tested with $\delta=\pi/5$ (and hence $\alpha=0.3120$, $\beta=-0.6056$) in equation (143)

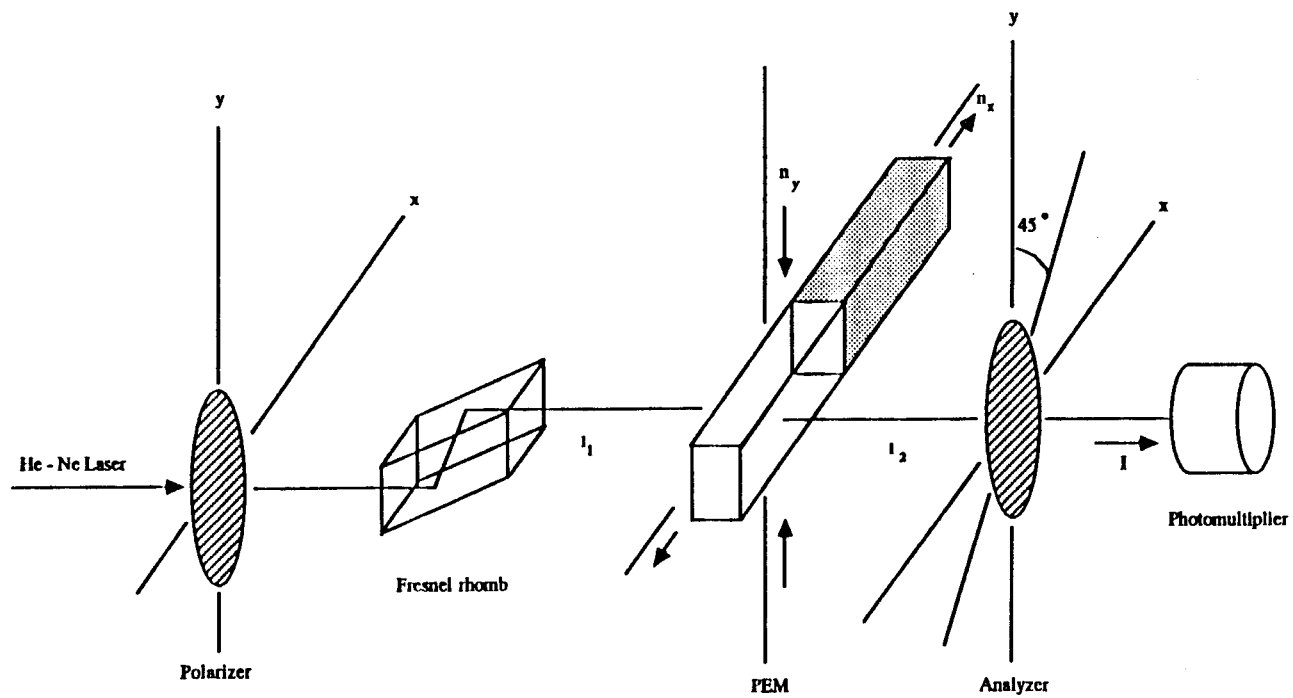

Figure. 15. Setup used to test the performance of the PEM modulator-analyzer system. The polarization state of the incident beam is defined by the orientation axis of the polarizer and Fresnel rhomb.

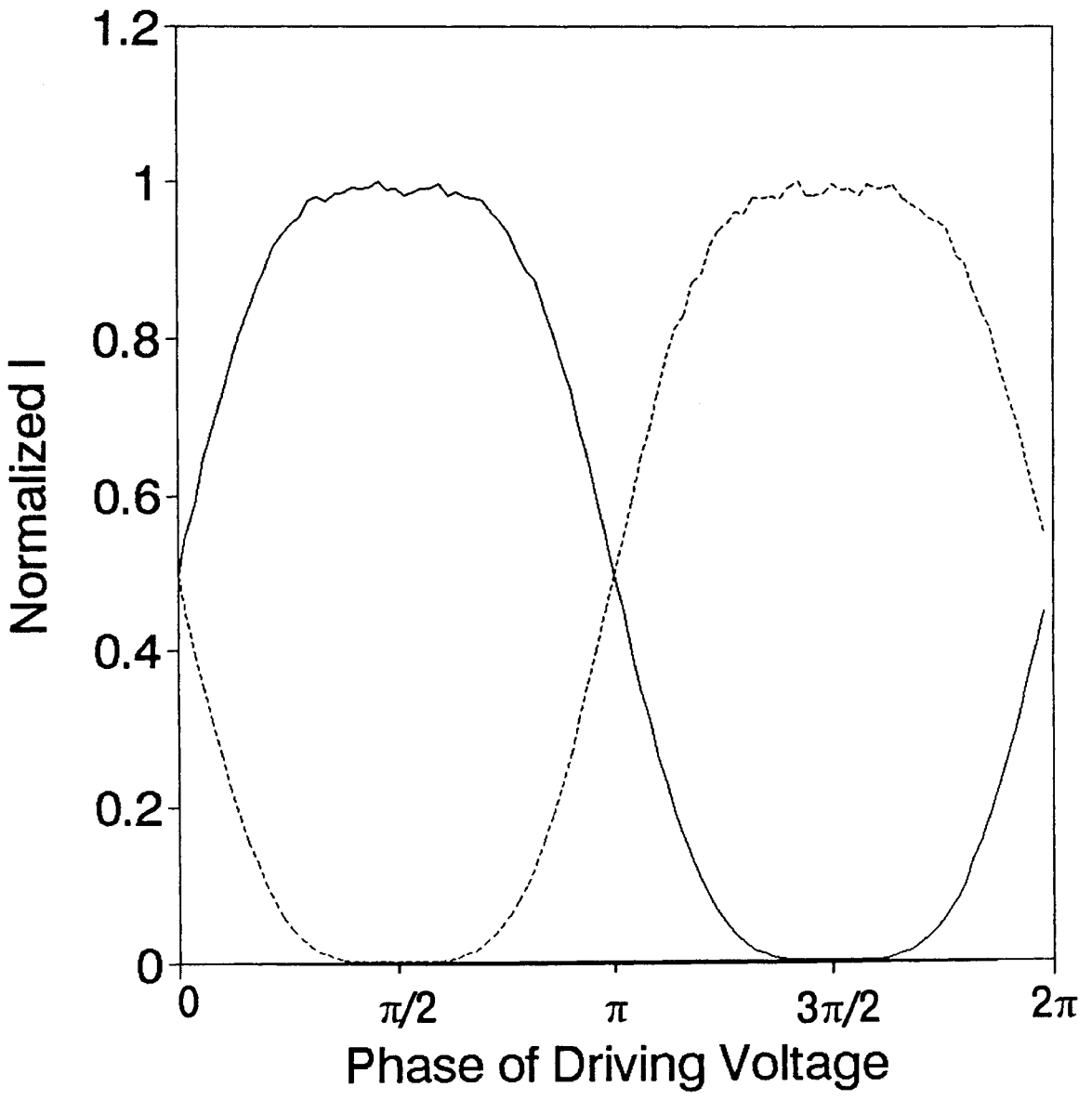

Figure. 16. Measured response the spectropolarimeter to two input monochromatic beams (λ=632.8 nm) circularly polarized σ^+ and σ^-. The solid line is the response to σ^+ and the dashed line to σ^- circular polarization. The gate width and the step size are set to 0.2μs.

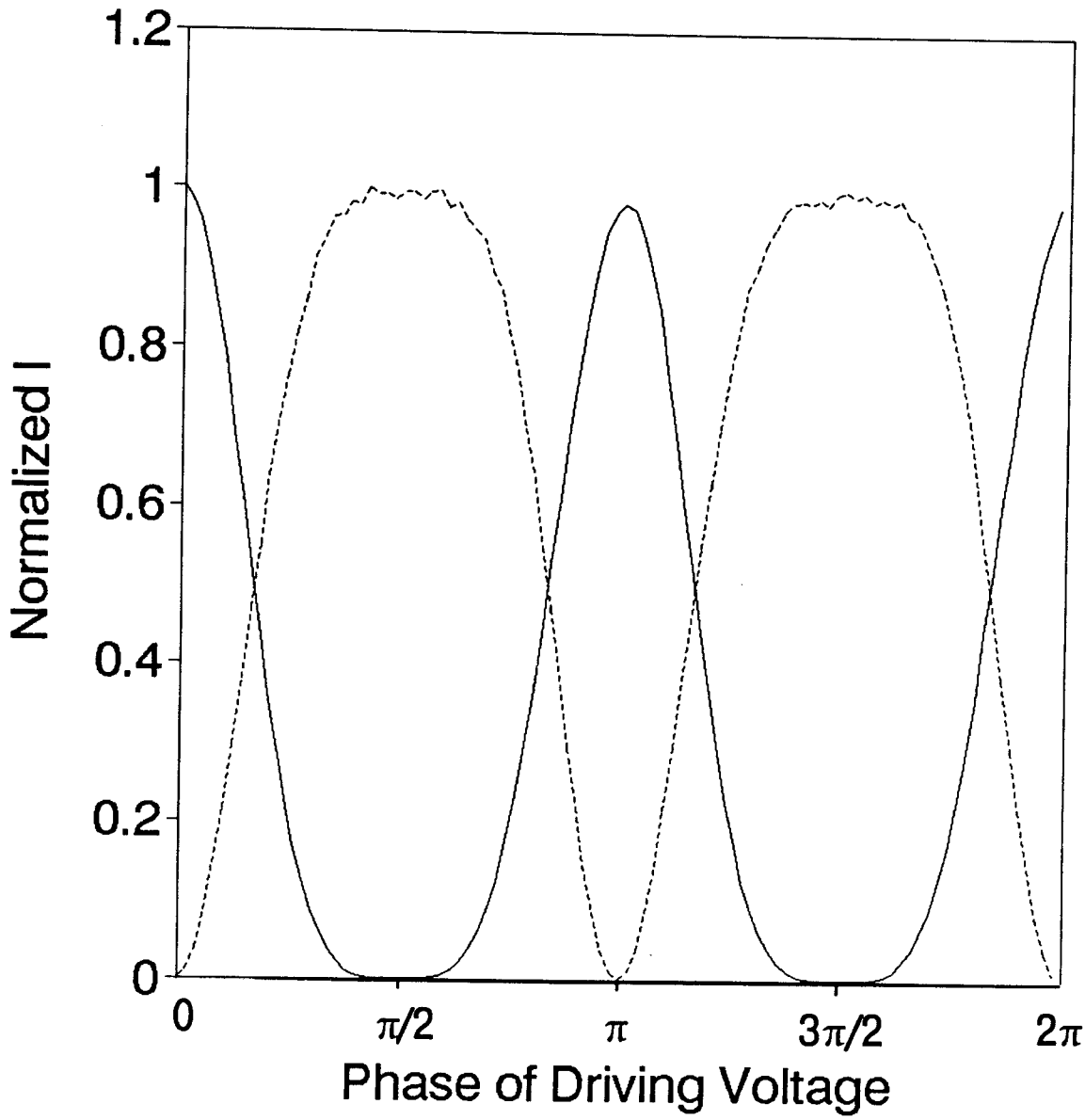

Figure. 17. Measured response the spectropolarimeter to two input monochromatic beams (λ=632.8 nm) linearly polarized I(+45°) and I(-45°). The solid line is the response to I(+45°) and the dashed line to I(-45°) linear polarization. The gate width and the step size are set to 0.2μs.

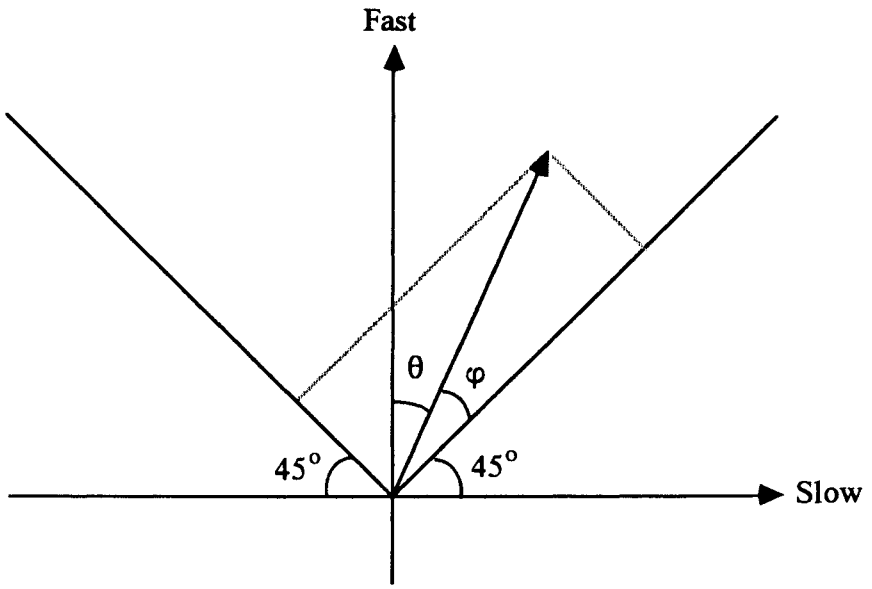

Figure. 18. Geometry used to simulate the partially polarized light. The linear polarizer is rotated $\varphi°$ away from 45° to the fast axis of the retarder.

and partial circular polarization was tested with $\delta = \pi/4$ (and hence $\gamma=0.7684$) in equation (144). The results are compared with equation (149) in Figure 19 where the solid line is the theoretical curve given by equation (149). The superimposed symbols (*) and (▲) are the experimental data for linear and circular polarization respectively.

The accuracy of measured degree of polarization ρ is affected by the statistical fluctuation in the number of counts in counters A and B. In the case of Poisson distribution (for PMT), the standard deviation in ρ is proportional to $(N_{A,B})^{-1/2}$. So N_t should be set according to the signal intensity and the accuracy required.

The apparatus setup described here has proved to be very stable and accurate due to the capability of compensating the fluctuation in excitation source and the capability of electronically tracing the modulation wavelength. The main advantages of this setup over the previously published ones are that it retains the normal PL and PLE (or transmission, scattering, etc.) spectroscopic information while measuring the degree of polarization for either circularly or linearly polarized cases. In addition, the asymmetric and curvy response of PEM-analyzer train to a linearly polarized light is corrected by software. The matching of A and B counters should not cause any big concern. Electronically, by setting same discriminator threshold level, the two counters can be easily matched as close as $|(\eta_A-\eta_B)/(\eta_A+\eta_B)| < 10^{-3}$. In fact, even if the counters A and B are mismatched, in other words, without assuming $\eta_A=\eta_B$ in equations (134) and (135), the counts A and B in final results [equations (143) and (144)] are simply replaced

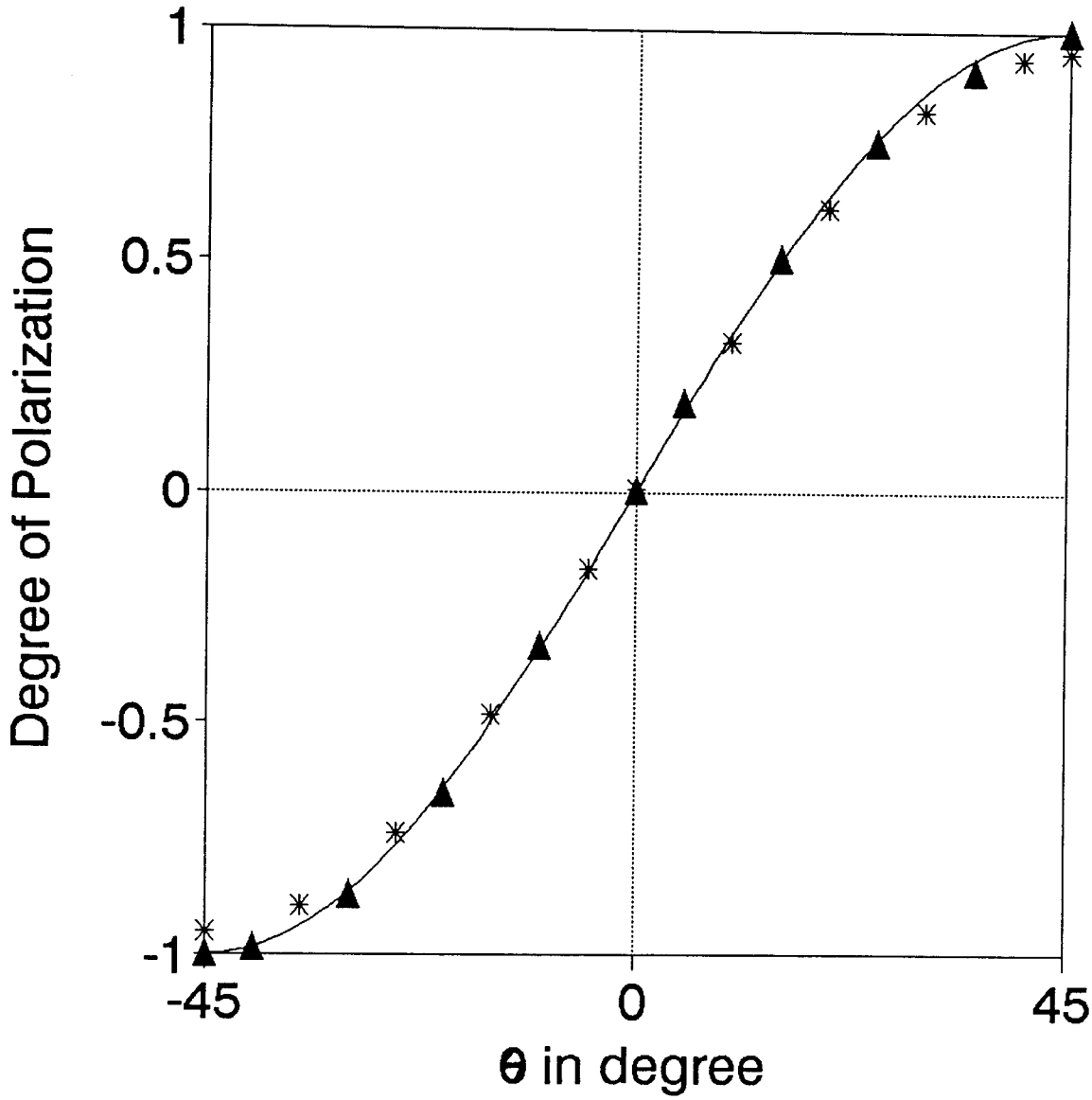

Figure. 19. Comparison of the theoretical curve calculated from equation (149) (solid line) and the experimental measurements for the partially polarized light. (*) is for linear polarization and (▲) for circular polarization.

by A/η_A and B/η_B respectively. The difference between η_A and η_B can be very easily determined experimentally.

§ 5-3 Results and Discussion

1. *PL at Different Temperatures:*

Figure 20 shows the PL spectra of the samples with well width 25Å, 50Å, 75Å respectively. The spectra were measured at 9.0K using the 488nm Ar^+ laser line for excitation. The excitation is indirect (i.e. free carriers are photogenerated in $Cd_{0.79}Zn_{0.21}Te$ barriers and then transferred into CdTe wells.) As expected, the sharp emission peak was shifted to lower energy and become narrower as the well width is increased. The main emission peak can not be explained by a single line (it is neither Gaussian nor Lorentzian). Instead, it can be fitted gracefully to a combination of two lines, one Gaussian and one Lorentzian as shown in Figure 21. The least square fit of QW3 (L_w=75Å)'s spectrum yields line widths of 7.553 meV and 6.65 meV, centered at 1.6049 eV and 1.6005 eV respectively. In the bulk binary II-VI semiconductors, the line width of the bound exciton is smaller than kT since the bound exciton has no kinetic energy. The line shape is described by the Lorentzian function. The free exciton line shape is described by Gaussian function. I believe that the Gaussian peak at 1.6049 eV originates from the confined n=1 electron and n=1 heavy hole free exciton transition and the Loranzian peak at 1.6005 meV is attributed to the excitons bound to neutral

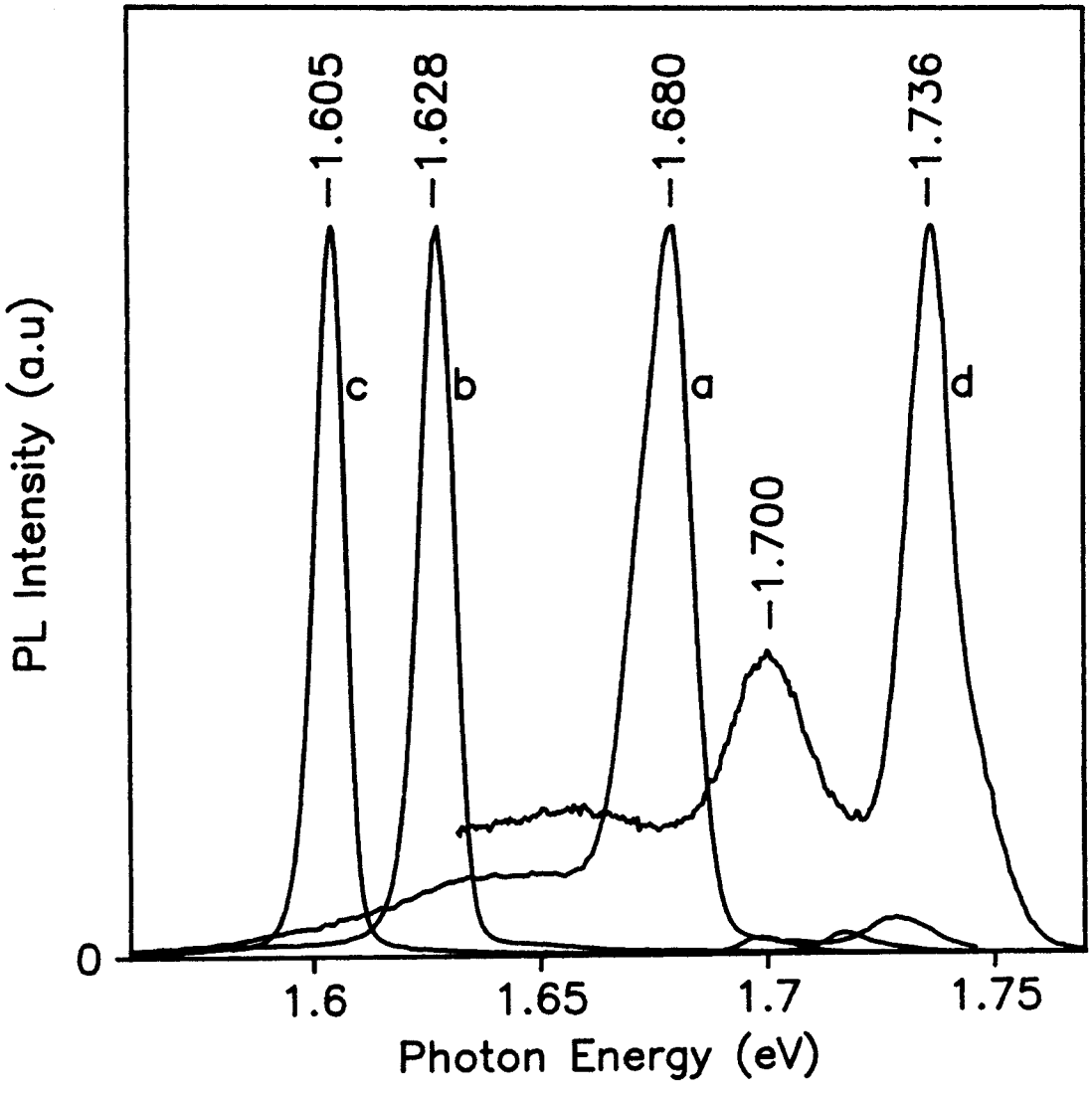

Figure. 20. Photoluminescence spectra (T=9.0K) of CdTe/$Cd_{0.79}Zn_{0.21}Te$ strained-layer single quantum well samples with well widths (a) 25Å, (b) 50Å, and (c) 75Å respectively. Spectrum (d) is the photoluminescence of a $Cd_{0.79}Zn_{0.21}Te$ epitaxial layer sample.

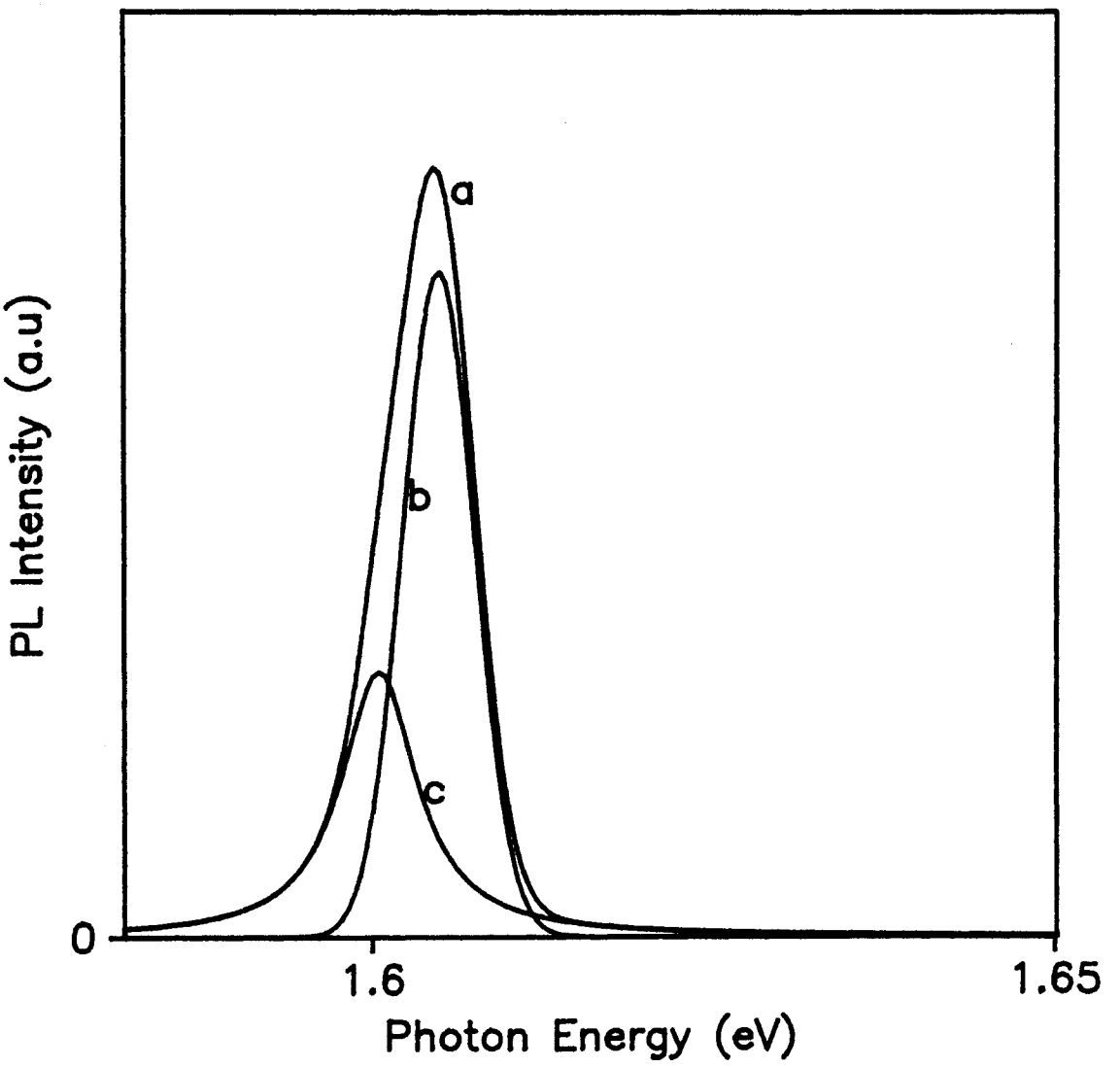

Figure. 21. Decomposition of the PL spectrum for 75Å $CdTe/Cd_{0.79}Zn_{0.21}Te$ strained-layer single quantum well (a) into two components, (b) a Gaussian shape free-exciton line and (c) a Lorentzian shape bond exciton line.

acceptors (E_{1h} - A°) in CdTe quantum well. Similar high quality fittings were also obtained for the other two samples except that sample QW1 (L_w=25Å) exhibits one additional peak on the lower energy side of the main emission peak, which, by comparison with the PL spectra of 3μm $Cd_{0.79}Zn_{0.21}Te$ epitaxy layer grown at same conditions as the buffer layer in our quantum wells samples (Figure 20d), is attributed to an unidentified band at buffer-substrate interface. This band also exists at the buffer-substrate interface of the other two samples (Lw=50Å, 75Å). However, we can not see it because the optical gap (window) in these two samples are too narrow to let this emission come out. Figure 22 shows the PL spectra of QW1 (Lw=25Å) at different excitation intensities. The spectrum a was recorded at the excitation intensity 0.64 W/cm^2 and spectrum b at 1.6 W/cm^2 using Ar^+ ion laser line 488nm. The spectra are normalized at maximum. The additional low energy band gets saturated at higher excitation intensity. Such behavior suggests that the additional band may be determined by defects [95].

The temperature dependence of PL spectra of QW3 (Lw=75Å) is shown in Figure 23. The photoluminescence is quenched mainly due to the thermally activated nonradiative recombination channel in the well and the temperature dependence transfer mechanism of photogenerated carriers from barrier to well. The inset shows the activation energies obtained from the quenching data of the decomposed free exciton emission peak. Figure 24 shows the temperature dependence of line width of the free exciton emission. The half width (FWHM) of the n=1 electron-heavy hole excitonic

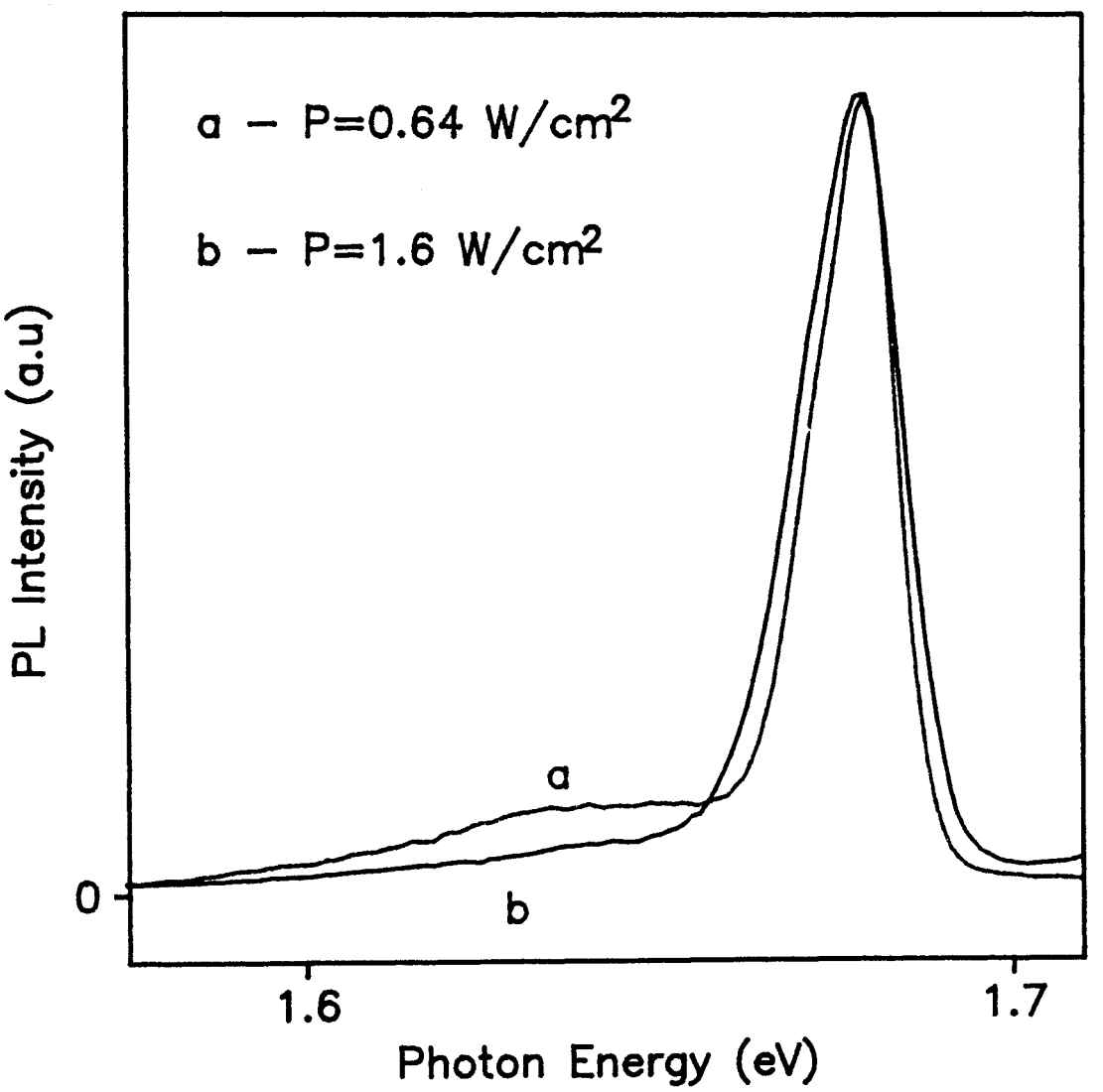

Figure. 22. Photoluminescence spectra of the 25Å $CdTe/Cd_{0.79}Zn_{0.21}Te$ strained-layer single quantum well sample under different excitation intensities.

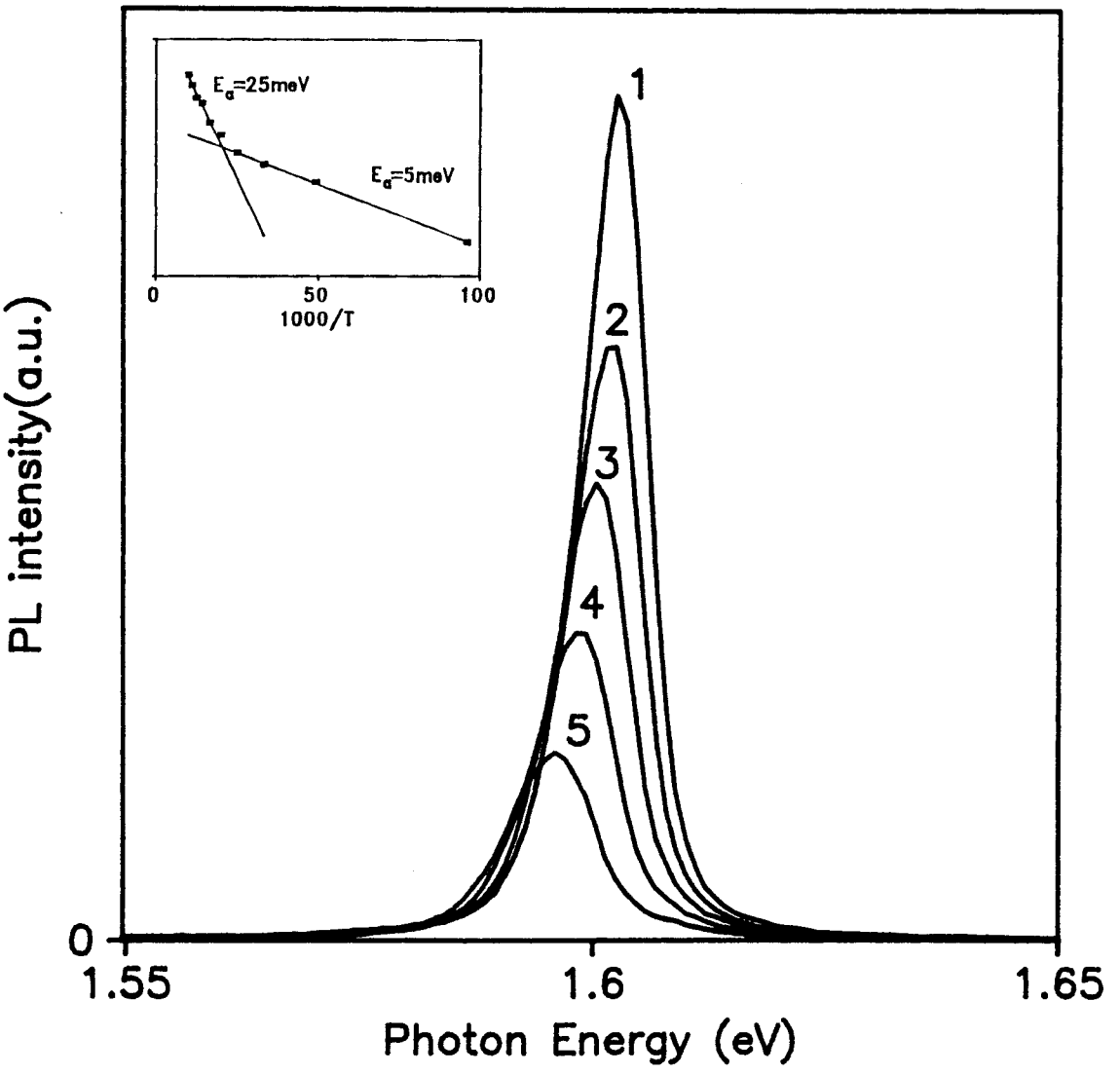

Figure. 23A. Photoluminescence spectra of the 75Å $CdTe/Cd_{0.79}Zn_{0.21}Te$ strained-layer single quantum well sample measured at different temperatures between 10 K and 50 K (step 10 K). The inset shows the Arrhenius plots of integrated PL intensity versus 1/T which reveals two activation energies of 25meV and 5meV.

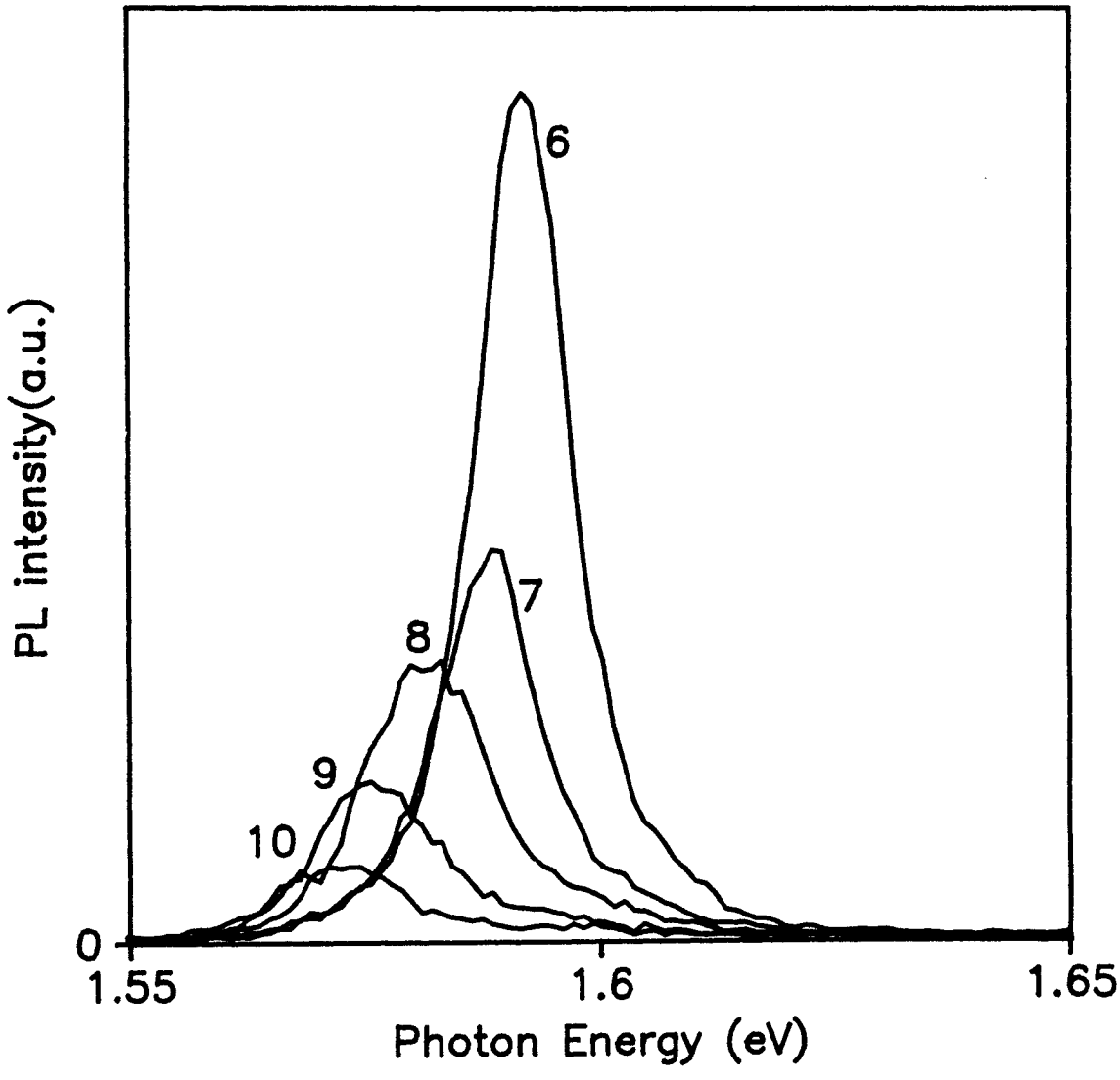

Figure. 23B. Photoluminescence spectra of the 75Å $CdTe/Cd_{0.79}Zn_{0.21}Te$ strained-layer single quantum well sample measured at different temperatures between 60K and 100K (step 10 K).

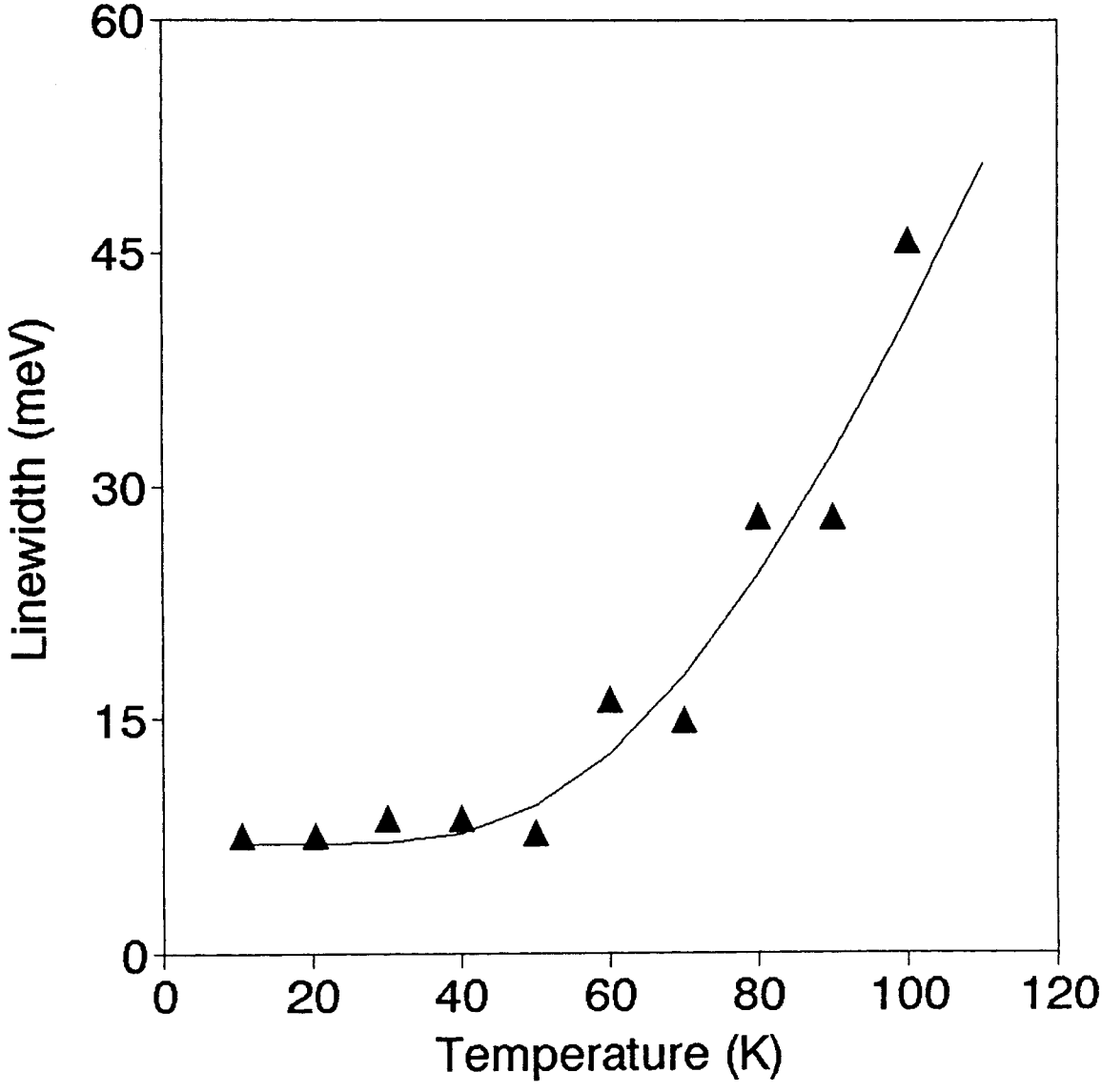

Figure. 24. Temperature dependence of linewidth (FWHM) of free exciton emission. The solid line is the theoretical curve given by equation (150). Experimental data are indicated by ▲.

emission increases slowly in the temperature range of 9-50K but increases rapidly with temperature above 50K. This behavior is described by the equation [96]

$$\Gamma_{tot} = \Gamma_0^+ + \Gamma_{ph}\left[\exp\left(\frac{E_{LO}}{kT}\right)-1\right]^{-1} + \Gamma_{imp}\exp\left(\frac{-<E>}{kT}\right) \qquad (150)$$

where the first term Γ_0^+ is the linewidth due to the inhomogeneous fluctuation of the well thickness. Second term Γ_{ph} describes the interactions between exciton and longitudinal optical (LO) phonon and the last term Γ_{imp} is the line width due to the ionized-impurity scattering. <E> is the average binding energy of impurities. Fitting the above equation to thermal quenching data yields the solid line in Figure 24 with the parameters: Γ_0^+ = 75 meV, Γ_{ph}=400 meV, E_{LO}= 22 meV, Γ_{imp}= 500 meV and <E> = 92 meV.

2. *Circularly Polarized Excitation Spectra:*

Since the calculation has shown that the band line up is type I for heavy holes and type II for light holes, the main emission peak is expected to be characterized predominantly by heavy hole feature, which is clearly shown in circular polarization optical pumping spectra (Figure 25). The degree of circular polarization ρ is defined as [97]

$$\rho = \frac{I^+ - I^-}{I^+ + I^-} \qquad (151)$$

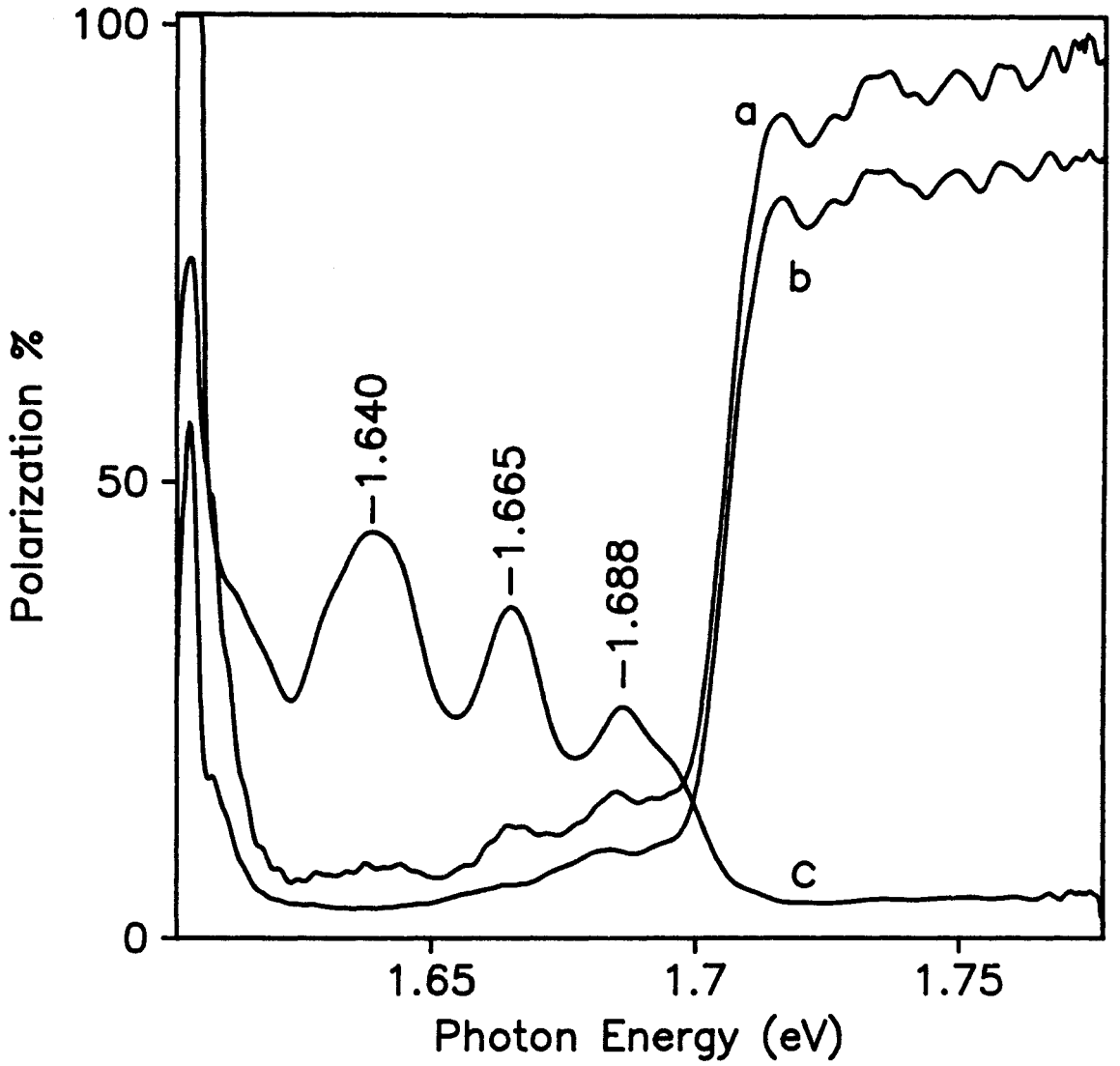

Figure. 25A. The polarized excitation spectra excited by circularly polarized (σ^-) Ti:Sapphire laser beam. The polarized spectra (a) σ^+ and (b) σ^- are obtained when detecting at longer wavelength side of free exciton transition 1*e*-1*h*. Curve (c) is the degree of polarization.

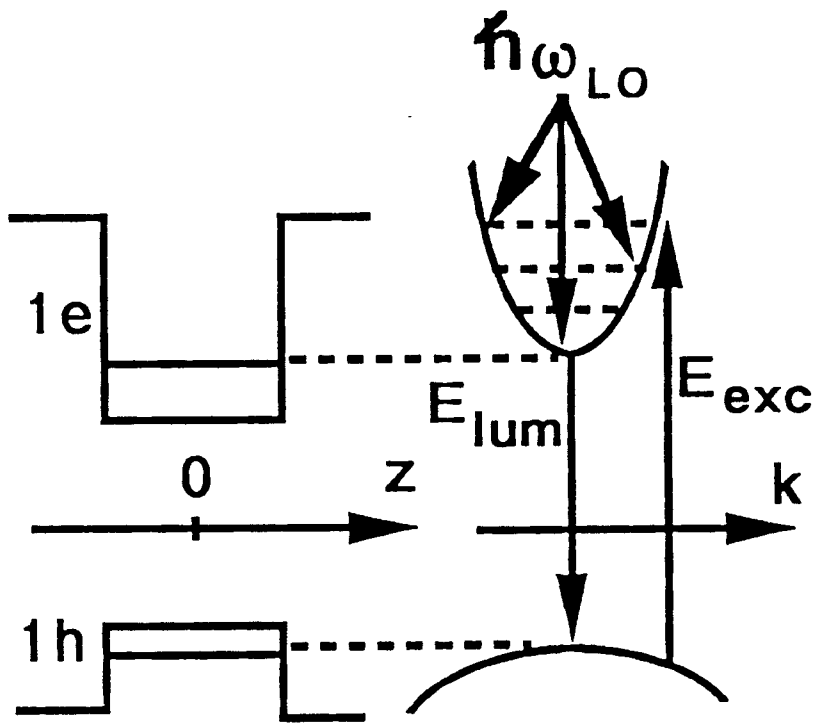

Figure. 25B. Phonon-assisted cooling process of hot electrons.

where I^+ and I^- are the intensities of right and left circularly polarized (σ^+ and σ^-) radiation.

In bulk materials, according to the selection rule shown in Figure 10, the maximum degree of circular polarization that can be expected is only 25% because of the degeneracy at the top of the valence band.

In the case of SL SQWs or SL SLs, on one hand, the removal of the degeneracy by strain and confinement effects suggests that degree of circular polarization as high as 100% could be observed. On the other hand, however, the mixing of the states due to the in-plane dispersion lowers the degree of polarization. Furthermore, the spin relaxation of the photogenerated carrier also reduces the degree of polarization. And finally, the sample's orientation relative to the direction of excitation beam and observation direction also affects the observed degree of polarization [86,97]

$$\rho \propto \frac{2(\boldsymbol{\nu}\cdot\boldsymbol{n}_1)(\boldsymbol{\nu}\cdot\boldsymbol{n})}{1+(\boldsymbol{\nu}\cdot\boldsymbol{n})^2} = -\frac{2\cos\alpha\cos\beta}{1+\cos^2\alpha} \qquad (152)$$

where $\mathbf{n}$, $\mathbf{n}_1$ and $\boldsymbol{\nu}$ are unit vectors in the direction of excitation beam, observation and sample growth respectively (see Figure 26).

The circularly polarized excitation spectrum of QW3 (Lw=75Å) is shown in Figure 25a. The transition monitored is the long wavelength side of the free exciton

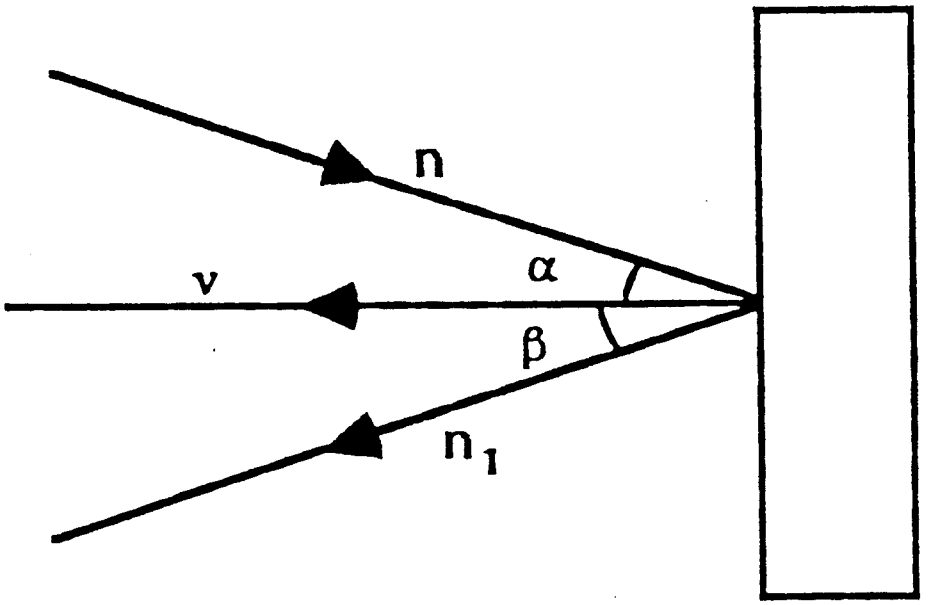

Figure. 26. The excitation and observation geometry in relation to sample orientation.

(1e-1h) at 1.605 eV. The excitation source was CW Ti:Sapphire tunable laser. The linearly polarized laser beam was circularly polarized (σ^-) by achromatic quarter wave retarder. The detecting system record simultaneously in two gated photon counters the σ^+ and σ^- components of the luminescence light which are curves a and b, respectively. Curve c is the circularly polarized excitation spectrum calculated using equation (119). Similar spectra were obtained for all the SQW samples studied. The forbidden transition (1e-2h, 1e-3h, etc.) energies, according to calculations, happen to be in the valleys of the excitation spectra shown in Figure 25a. Therefore, the peaks in Figure 25a at 1.683, 1.663, and 1.639 eV are related to the LO phonon replicas (bulk CdTe's LO phonon energy is 21 meV) as indicated in Figure 25b.

As one can see in Figure 25a, when the excitation energy $h\nu$ is larger than barrier band gap (but smaller than $E_g + \Delta$ of the barrier), most of the spin orientation of photogenerated carriers created by σ^- excitation are relaxed in the process of transferring to the quantum well and subsequent thermalization (or cooling) in the quantum well before recombination, and hence very low degree of polarization is observed. When the excitation energy $h\nu$ is below the barrier such that $[h\nu-(E_{1e}+E_g+E_{1hh})]m^*_{hh}/(m^*_{hh}+m^*_e)$ is a multiple of LO phonon energy $\hbar\omega$, the excited hot electrons emit LO phonons and fall directly to the bottom of the subband retaining most of their spin orientation [98]. The gradual decrease of the degree of luminescence polarization with increasing number of emitted LO phonons indicates noticeable spin relaxation at each stage of the cascade. When the condition $[h\nu-(E_{1e}+E_g+E_{1hh})]m^*_{hh}/ (m^*_{hh}+m^*_e) = n\hbar\omega_{LO}$ is not fulfilled, the

cooling process always involves emission of a great number of acoustic phonons and spin orientation of the hot electrons is significantly relaxed. When the excitation photon (σ^-) energy $h\nu$ is resonant with the emission peak, the degree of circular polarization as high as 73% is observed.

3. *Collection of Photogenerated Carriers into the Wells*

Assuming a uniform absorption coefficient of $5x10^{-4}$/cm for $Cd_{0.79}Zn_{0.21}Te$ at 10K at 488 nm, 99% of the incident photons during a PL experiment are absorbed within the 0.5μm thick cap [barrier] layer, though thin quantum wells give very intense PL (I_w is 50 times stronger than I_b.) Evidently, most of the carriers generated in the barrier are transferred into the well before recombination occurs. The carrier collection dynamics of SQWs have been studied by many groups [99,100]. The simple lumped continuity equations are written

$$\begin{aligned} g_b d_b &= \frac{n_b}{\tau_{rb}} + \frac{n_b}{\tau_{nrb}} + \frac{n_b}{\tau_{tr}} \\ g_w d_w &+ \frac{n_b}{\tau_{tr}} = \frac{n_w}{\tau_{rw}} + \frac{n_w}{\tau_{nrw}} \end{aligned} \qquad \textbf{(153)}$$

where the subscript r, nr and tr denote radiative, nonradiative and transfer; b and w denote the barrier and well respectively; n_b and n_w are the two-dimensional minority-carrier concentrations; g_bd_b and g_wd_w are the two-dimensional generation rate in the barrier and the well; and τ's are the associated minority-carrier life times. The t_{tr} is the

time needed to transfer photogenerated carriers from 5000Å barrier into the well. The internal radiative recombination rate per unit area I_b and I_w are given

$$I_b = \frac{n_b}{\tau_{rb}}$$
$$I_b = \frac{n_w}{\tau_{rw}} \qquad (154)$$

Equations (153) - (154) may be written in matrix form

$$\begin{bmatrix} 1+\frac{\tau_{rb}}{\tau_{tr}}+\frac{\tau_{rb}}{\tau_{nrb}} & 0 \\ -\frac{\tau_{rb}}{\tau_{tr}} & 1+\frac{\tau_{rw}}{\tau_{nrw}} \end{bmatrix} \begin{bmatrix} I_b \\ I_w \end{bmatrix} = \begin{bmatrix} g_b d_b \\ g_w d_w \end{bmatrix} \qquad (155)$$

which has the solution

$$\begin{bmatrix} I_b \\ I_w \end{bmatrix} = \left(\left(1+\frac{\tau_{rb}}{\tau_{tr}}+\frac{\tau_{rb}}{\tau_{nrb}} \right) \left(1+\frac{\tau_{rw}}{\tau_{nrw}} \right) \right)^{-1} \begin{bmatrix} 1+\frac{\tau_{rw}}{\tau_{nrw}} & 0 \\ \frac{\tau_{rb}}{\tau_{tr}} & 1+\frac{\tau_{rb}}{\tau_{tr}}+\frac{\tau_{rb}}{\tau_{nrb}} \end{bmatrix} \begin{bmatrix} g_b d_b \\ g_w d_w \end{bmatrix} \qquad (156)$$

hence

$$\frac{I_w}{I_b} = \frac{\frac{\tau_{rb}}{\tau_{tr}}+\left(1+\frac{\tau_{rb}}{\tau_{tr}}+\frac{\tau_{rb}}{\tau_{nrb}} \right) \frac{g_w d_w}{g_b d_b}}{1+\frac{\tau_{rw}}{\tau_{nrw}}} = \eta_w \frac{\tau_{rb}}{\tau_{tr}} \left[1+\left(1+\frac{\tau_{tr}}{\tau_{rb}}+\frac{\tau_{tr}}{\tau_{nrb}} \right) \frac{g_w d_w}{g_b d_b} \right] \qquad (157)$$

where

$$\eta_w = \frac{\frac{1}{\tau_{rw}}}{\frac{1}{\tau_{rw}} + \frac{1}{\tau_{nrw}}} \tag{158}$$

The ratio I_w/I_b can be approximated by the ratio of integrated PL intensities if we assume identical conversion factors linking the external and internal radiative recombination rates for the well and the barrier. It is quite reasonable to assume $\eta_w = 1$ [100]. Neglecting of carrier generation in the well simplifies equation (158) to

$$\frac{I_w}{I_b} = \frac{\tau_{rb}}{\tau_{tr}} \eta_w \tag{159}$$

Now, the time needed to transfer the photogenerated carriers from 5000Å thick $Cd_{0.79}Zn_{0.21}Te$ barrier to the CdTe well can be estimated if the radiative minority-carrier life time in the barrier is known

$$\tau_{tr} = \frac{I_b}{I_w} \eta_w \tau_{rb} \approx \frac{\tau_{rb}}{50} \eta_w \tag{160}$$

Assuming that the radiative lifetime in the barrier is the same as in bulk ZnTe, about ~ 2ns, and the quantum efficiency in well is $\eta_w = 1$, the estimated transfer time t_{tr} is 40 ps. If quantum efficiency η_w is not equal to unity, the transfer time should be shorter. From a Streak Camera measurement under indirect excitation, the emission from the well reached its peak about 550 ps after excitation pulse. That time is the sum

of the transfer time, the exciton creation time, and radiative life time of exciton in the well (t_{tr}+ t_{cx} + t_{rw}). The radiative life time of exciton in the well is about 510 ps if we ignore the exciton creation time t_{cx}.

Chapter Six

Conclusions and Proposals for Further Work

§ 6-1 Conclusions

The **k·p** method and Kane model description of the Γ-point band structure for zinc-blend structure semiconductors have been reviewed in detail. The envelope function approach has been applied to derive a three-band model for the electronic states in the strained-layer superlattices (SLSL) and strained-layer single quantum wells (SLSQW). Deformation potential theory has been used to calculate the energy band shift and the splitting caused by lattice-mismatch induced biaxial strain, which is equivalent to the combination of a hydrostatic strain and a uniaxial strain. When the coupling (mixing) between light hole band and the spin-orbit split off band by the uniaxial strain component, which is neglected by many earlier publications, is taken into account these two bands exhibit an anti-crossing behavior as functions of the strain. A transition from type II to type I for light hole band line-up has been predicted. An interpolation scheme has been developed for the parameters in ternary semiconductors. In this scheme, not only the band gap bowing effect but also the nonlinearity of each individual band as a function of composition x is considered. Based on the quasi cubic model description of the Γ-point band structure of zinc-blend and wurtzite structure materials, a relation

between the valence band edges in these two different structures (but same compound) has been given. This allows us to calculate the band edge positions in man made zinc-blend structure CdSe epitaxial layer from available experimental data on CdSe in wurtzite structure. An iteration relation derived from Robinson rotation and the minimum strain energy principle has been used to calculate the elastic constant tensor of zinc-blend structure material from the known elastic constant tensor of same compound in wurtzite structure.

From experimental low temperature photoluminescence spectra, a free 1e-1h exciton and a 1e-1h exciton state bound to neutral acceptors (E1h-A) are identified in CdTe/$Cd_{0.79}Zn_{0.21}Te$ strained layer single wells. The exciton binding energies have been estimated from the difference between the calculated 1e-1h energy gap and the experimental free exciton transition energy. The exciton binding energy decreased from 36.5 meV to 12.9 meV when well width is reduced from 75Å to 25Å. The analysis of the free exciton line width as a function of temperature indicates that the broadening mechanism is dominated by interaction between the excitons and the polar optical phonons. The temperature dependence of the integrated intensities of free excitons yields activation energy of 25 meV in high temperature region and 5 meV in low temperature region. In the study of low temperature photoluminescence spectra of 25Å-thick CdTe/ $Cd_{0.79}Zn_{0.21}Te$ single quantum well and those of epitaxy layer grown at same condition as the barrier layer, a broad emission band around 1.63 eV is identified as related to the

defect states at the interface between the buffer layer and the substrate. The exact nature of these defect states is not clear at this point.

For the measurement of optical polarization, a computerized spectropolarimeter and the measuring technique have been presented. Using the set up and the technique described here, the curvature and the asymmetry of the PEM-analyzer response are taken into account exactly. It allows one to use data from all parts of the modulation cycle rather than concentrating only on the photon counts that occur near the peaks. This spectropolarimeter is capable of compensating the variation of the excitation intensity with wavelength and time, and keeping the PEM's retardance constant even when the wavelength of modulated light is scanned over a wide range.

The circularly polarized excitation spectra of CdTe/ $Cd_{0.79}Zn_{0.21}Te$ strained-layer single quantum wells show predominant heavy hole feature. No light transition was observed. This confirms that the band lineup configuration is type I for heavy hole and type II for light hole. LO phonon replicas were observed in the polarized excitation spectra. The estimated LO phonon energy is $23 \sim 25$ meV.

§ 6-2 Suggestions for Further Work

This study has shown that for the CdTe/$Cd_{0.79}Zn_{0.21}Te$ strained-layer single quantum well samples with widths of 25 Å ~ 75 Å, the excitons in the well tend to recover a three-dimensional behavior with decreasing L_w because of the increasing penetration of electron and hole wave function into the barrier layers. When the well width become very large such that the electrons and holes are less confined in the growth direction, the binding energy of the excitons in the well should also decrease. The observation of this trend was limited by the dimension of the available samples. The main difficulty is that, with all that amount of strain taken by the well layer alone, it is hard to grow very thick highly strained well layer without defects. i.e. the larger the strain is, the thinner the critical thickness is. So I propose (to the sample grower) that a additional buffer layer of $Cd_{1-y}Zn_yTe$ be used so that the total strain can be shared between the barrier and well layers. For example, if at the maximum well width the ratio of well width to the barrier thickness is R, the optimum buffer composition would be $y = x \cdot R$, with x being the Zn composition in the well layer.

Another important effect that could have been studied in CdTe/ $Cd_{1-x}Zn_xTe$ strained-layer single quantum wells is the effect of an electric field on the excitons in the well-- the Stark effect. To apply an electric field across the QW structure, it is necessary to remove the semi-insulating GaAs substrate, then a decent facility is needed to make the contact on both sides of the QW structure. The piezoelectric property discussed in

§ 4-2 offers the possibility of building so called intrinsic Stark superlattices or quantum wells. Accordingly, the second proposal (to the sample grower) is the growth of <111> oriented $CdTe/Cd_{1-x}Zn_xTe$ strained-layer quantum well.

Comparison of photoluminescence experiment result on a group of 13Å-thick $CdTe/Cd_{1-x}Zn_xTe$ strained-layer quantum well samples with theoretical calculations shows the obvious incompetence of envelope function approach to calculate the electronic states in very thin-layer heterostructures. Some other more congruous technique such as tight-binding method is to be implemented. The interest of the tight-binding approach lies in the modelling of the microscopic interactions, taking into account the different type of atom, cation or anion and the interatomic coupling between *s* and *p* states. It can therefore reveal features unreachable with envelope function approach, such as interface states and LH-HH mixing.

In this study, the phonon states and their properties in the $CdTe/Cd_{1-x}Zn_xTe$ SLQWs have not been treated as much detail as the electronic ones, though some phonon assisted process were observed. From three-dimensional structure to two-dimensional structure, phonon energy states undergo similar changes to the ones that electronic energy states undergo, i.e. the folding of dispersion curve onto a shrunk Brillouin zone. This folding process results in additional modes at the zone center (Γ-point). The strain has effects on the phonon states energy analogous to the ones on the electronic states energy, i.e. shift and split of lattice vibrational frequency modes. Comparison of the Ramman

spectra of the heterostructure with those of relaxed (unstrained) epitaxial layers which have same compositions as barrier and well layers will help to identify the additional lattice vibrational modes and the amount shifted. Theoretical techniques for treating the phonon states problem in heterostructures at same level as the ones for treating electronic states problem in heterostructures are available in the literature but not applied in this study.

It is clear that many aspect of strained-layer heterostructures have yet to be investigated to complete the picture of our understanding of these structures.

REFERENCES

1. L. Esaki and R. Tsu,IBM Research Note RC-2418 (1969)
2. L. Esaki and R. Tsu, IBM J. Rec. Develop. **14**, 61 (1970)
3. Vav der Ziel et al, Appl. Phys. Lett. **26**, 463 (1975)
4. D.A.B. Miller, D.S. Chemla, and T.C. Damen, Phys. Rev. Lett. **53**, 2173 (1984)
5. D.L. Smith, T.C. McGill, and J.N.Schulman, APPl. Phys. Lett. **43**,180 (1983)
6. L. Esaki and L.L. Chang, Phys. Rev. Lett. **33**, 495 (1974)
7. R. Dingle, W. Wiegmann and C.H. Henry, Phys. Rev. Lett. **33**, 827 (1974)
8. G.H. Döhler, H. Künzel, D. Olego, K. Ploog, P. Ruden, H.J. Stolz, and G. Abstreiter, Phys. Rev. Lett. **47**, 864 (1981)
9. E. Carruthers and P.J. Lin-Chung, Phys.Rev. Lett. **38**, 1543 (1977)
10. E. Carruthers and P.J. Lin-Chung, Phys.Rev. B **17**, 2705 (1978)
11. W. Andreoni, A. Baldereschi and R. Car, Solid State Commun. **27**, 821 (1978)
12. J.N. Schulman and T.C. McGill, Phys. Rev. lett. **39**,1680 (1977)
13. J.N. Schulman and T.C. McGill, Pys. Rev. B **19**, 6341 (1979)
14. R.N.Nucho and A.Madhukar, J. Vac.Sci.Technol. **15**, 1530 (1978)
15. A. Madhukar, N.V. Dandekar and R.N. Nucho, J. Vac. Sci. Technol. **16**, 1507 (1979)
16. A. Madhukar and R.N. Nucho, Solid State Commun. **32**, 331 (1979)
17. J.N. Schulman and T.C. McGill, Appl. Phys. Lett. **34**, 663 (1979)
18. J.N. Schulman and T.C. McGill, J. Vac. Sci. Technol. **16**, 1513 (1979)
19. J.N. Schulman and T.C. McGill, Phys. Rev. B **23**, 4149 (1981)

20. A. Madhukar and J. Delgado, Solid State Commun. **37**,199 (1981)

21. G.C. Osbourn, J. Appl. Phys. **53**, 1586 (1982)

22. G.C. Osbourn, J. Vac. Sci. Technol. **21**, 469 (1982)

23. J.N. Schulman and Y.C. Chang, Phys. Rev. B **24**, 4445 (1981)

24. J.N. Schulman and Y.C. Chang, Phys. Rev. B **27**, 2346 (1983)

25. Y.C. Chang and J.N. Schulman, Phys. Rev. B **25**, 3975 (1982)

26. D.H. Lee and J.D. Joannopoulos, Phys. Rev. B **23**, 4988 (1981)

27. D.H. Lee and J.D. JOannopoulos, Phys. Rev. B **23**, 4997 (1981)

28. Y.C. Chang and J.N. Schulman, Appl. Phys. Lett. **43**,540 (1983)

29. G. Dresselhaus, A.F.Kip and C.Kittel, Phys.Rev. **98**, 368 (1955)

30. E.O. Kane, J. Phys. Chem. Solids **1**, 82 (1956)

31. J.M. Luttinger and W. Kohn, Phys. Rev. **97**, 869 (1955)

32. R. Dingle, A.C. Gossard and W. Weigmann, Phys. Rev. Lett. **34**, 1327 (1975)

33. R. Dingle, W. Weigmann and C.H. Henry, Phys. Rev. Lett. **33**, 827 (1974)

34. D. Mukherji and B.R. Nag, Phys. Rev. B **12**, 4338 (1975)

35. G. Bastard, Phys. Rev. B **24**, 5693 (1981)

36. G. Bastard, Phys. Rev. B **25**, 7584 (1982)

37. S.R. White and L.J. Sham, Phys. Rev. Lett. **47**, 879 (1981)

38. E.O. Kane, J. Phys. Chem. Solids **1**, 249 (1957)

39. P.O. Löwdin, J. Chem. Phys. **19**, 1396 (1951)

40. M. Altareli, J. Lumin. **30**, 472 (1985)

41. M. Altareli, U. Ekenberg and A. Fasolino, Phys. Rev. B **32**, 5138 (1985)

42. Y.C. Chang, J. Appl. Phys. **58**, 499 (1985)

43. Y.C. Chang, Appl. Phys. Lett. **46**, 710 (1985)

44. D.L. Smith and C. Mailhiot, Phys. Rev. B **33**, 8345 (1986)

45. C. Mailhiot and D.L. Smith, Phys. Rev. B **33**, 8360 (1986)

46. D.L. Smith and C. Mailhiot, J. Appl. Phys. **62**, 2545 (1987)

47. D.M. Bylander and L. Kleinman, Phys. Rev. B **36**, 3229 (1987)

48. C.G. Van De Walle and R.M. Martin, Phys.Rev. B **35**, 8154 (1987)

49. I.P. Batra, S. Ciraci and J.S. Nelson, J. Vac. Sci. Technol. B **5**, 1300 (1987)

50. M.S. Hybertsen and M. Schülter, Phys. Rev. B **36**, 9683 (1987)

51. N. Samarth, H. Luo, J. K. Furdyna, S. B. Qadri, Y. R. Lee, A. K. Ramdas, and N. Otsuka, Appl. Phys. Lett. **54**, 2680 (1989)

52. P. Renaud, American Institute of Physics Conference Proceedings No.227, American Vacuum Society Series 10, "Advanced processing and characterization technologies", edited by P.H. Holloway, (AIP, Clearwater, FL 1991)

53. S.E. Ulloa and G. Kirczenow, Phys. Rev. Lett. **57**, 2991 (1986)

54. J. Zhang, Dissertation, Phys. Dept. Ohio Univ. (1990)

55. R.H. Miles, G.Y. Wu, M.B. Johnson and T.C. McGill, Appl. Phys. Lett. **48**, 1383 (1986)

56. Yoichi Kawakami and Tsunimasa Taguchi, J. Vac. Sci. Technol. B **7**, 789 (1989)

57. J. Warnock, A. Petrou, R.N. Bicknell et al, Phys. Rev. B **32**, 8116 (1985)

58. K. Shahzad and D.J. Olego, Phys. Rev. B **38**, 1417 (1988)

59. K. Mohammed, D.J. Olego, P. Newbury, D.A. Cammack, R. Dalby, and

H. Cornelissen, Appl. Phys. Lett. **50**, 1820 (1987)

60. D.K. Blanks, J. Vac. Sci. Technol. **A 4**, 2120 (1986)

61. G. Dresselhaus, A. F. Kip, and C. Kittel, Phys. Rev. **98**, 368 (1955)

62. F. Bloch, Z. Physik, **52**, 555 (1928)

63. R. Shankar, "Principle of Quantum Mehanics", (Plenum Press, New York, 1980)

64. J.M. Luttinger, Phys. Rev. **102**, 1030 (1956)

65. N.W. Ashcroft, N.D. Mermin, "Solid State Physics", (Holt, Rinehart and Winston, New York, 1976)

66. D.J. Ben Daniel and C.B. Duke, Phys. Rev. **152**, 682 (1966)

67. G.L. Bir and G.E. Pikus, "Symmetry and Strain-Induced Effects in Semiconductors", (J. Wiley, New York, 1974)

68. F.H. Pollak in "Semiconductors and Semimetals" Vol.32, Edited by T.P. Pearsall, (Academic Press Inc., San Diego, CA 1990)

69. H. Kroamer in " Molcular Beam Epitaxy and Heterostructures", NATO ASI Series, Edited by L.L. Chang and K. Ploog, (Martinus Nijhoff, Dordrecht 1985)

70. W.F. Cady, "Piezoelectricity", (McGraw-Hill, New York 1946)

71. H.J. Lozykowski and V.K. Shastri, J. Lumin. **48&49**, 740 (1991)

72. H.J. Lozykowski and V.K. Shastri, J. App. Phys. **69**, 3235 (1991)

73. J.L. Birman, Phys. Rev. **114**, 1490 (1959)

74. J.J. Hopfield, J. Phys. Chem. Solids, **15**, 97 (1960)

75. S.L. Adler, Phys. Rev. **126**, 118(1962)

76. B. Segall and D.T.F. Marple in "Physics and Chemistry of II-VI Semiconductors", Edited by M. Auer and J.S. Prener, (North-Holland Publ., Amsterdam, 1967)

77. R.G. Weeler and J.O. Dimmock, Phys. Rev. **125**, 1805 (1962)

78. R.W.G. Wyckoff, "Crystal Structures", (Interscience, New York,1963)

79. F.N.H. Robinson, Phys. Lett. **26A**, 435 (1968)

80. R.M. Martin, Phys. Rev. **B 6**, 4546 (1972)

81. J.L. Reno and E.D. Jones, Abstracts of Materials Research Society fall meeting, 52, November, (1990)

82. V. Shastri, Disertation, ECE Dept. Ohio Univ. (1991)

83. Modern Problems in Condensed Matter Sciences, Vol. 8: "Optical Orientation", edited by F. Meier and B. P. Zakharchenya, (North-Holland, New York 1984).

84. F. S. Richardson and J. P. Riehl, Chem. Rev., **77**, 773 (1977)

85. J. E. Wampler and R. J DeSa, Analytical Chem., **46**, 563 (1974)

86. V. I. Perel and B. P. Zakharchenya in Modern Problems in Condensed Matter Science, Vol. 8, "Optical Orientation", Edited by F. Meier, (North Holland, New York, 1984).

87. I. Z. Steinberg and B. Ehrenberg, J. Chem. Phys., **61**, 3382 (1974)

88. R. R. Parsons, Canadian J. of Phys., **49**, 1850 (1971)

89. W. Bickel and W. Bailey, Am. J. of Phys., **53**, 468 (1985)

90. M. J. Walker, Am. J. of Phys., **22**, 170 (1954)

91. H.C. Chen, "Theory of electromagnetic waves: a coordinate free appraoch", (McGraw-Hill Book Co., New York, 1983)

92. T. Li and H. J. Lozykowski, Phys. Rev. B **46**, (1992)

93. J. Y. Marzin, M. N. Cherasse and B. Sermage, Phys. Rev., **B31**, 8298 (1985)

94. A. J. Wojtowicz and H. J. Lozykowski, ACTA Physica Polynica, **A54**, 867 (1978)

95. G. Ambrazecius, S. Marcinkevicius, T. Lideikis, and K. Nandzius, Semicond. Sci.Technol., **6**, 41 (1991)

96. J. Lee, E. S. Koteles, and M. O. Vassell, Phys. Rev., **B 33**,5512 (1986)

97. C. Weishbuch, R. C. Miller, R. Dingle, A. C. Gossard, and W. Wiegmann, Solid State Comm., **37**, 219 (1987).

98. G. E. Pikus and A. N. Titkov in Modern Problems in Condensed Matter Science, Vol. 8, "Optical Orientation", Edited by F. Meier, (North Holland,New York, 1984).

99. E. H. Reihlen, A. Persson, T. Y. Wang, K. L. Fry and G. B. Stringffellow, J. Appl. Phys., **66**, 5554 (1989).

100. D. Bimberg, J. Christen, A. Steckenborn, G. Weimann, and W. Schlap, J. Lumin., **30**, 562 (1985) .

101. R. L. Green, K. K. Bajaj, and D. E. Phileps, Phys. Rev. B **29**, 1807 (1984)

102. J. A. Brum and G. Bastard, E. E. Mendez, L. L. Chang, and L. Esaki, Phys. Rev. B **26**, 1974 (1982)

103. J. A. Brum and G. Bastard, J. Phys. C **18**, L789 (1985)

104. J. A. Brum and G. Bastard, Pys. Rev. B **31**, 3893 (1985)

105. D. C. Renolds and T. C. Collins, "Excitons: Their Properties and Uses" (Academic, New York, 1981)

106. Y. Merle d'Aubigné, Le Si Dang, F. Dalbo, G. Lentz, N. Magnéa, and H. Mariette, Superlatt. Microstruct. **5**, 367 (1989)

107. H. Mathieu, J. Allegre, A. Chatt, P. Lefebvre, and J. P. Faurie, Phys. Rev. B **38**, 7740 (1988)

108. B. Gill, D. J. Dunstan, J. Calatayud, H. Mathieu, and J. P. Faurie, Phys. Rev. B **40**, 5522 (1988)

109. J. Allegre, J. Calatayud, B. Gill, H. Mathieu, H. Tuffigureo, G. Lentz, N. Magnéa, and H. Mariette, Phys. Rev. B **41**,8195 (1990)

110. H. Mariette, F. Dalbo, N. Magnéa, G. Lentz, and H. Tuffigureo, Phys. Rev. B **38**, 12443 (1988)

111. C. Kittel, "Introduction to solid state physics", (Wiley, New York, 1966)

112. G. Nimtz, in "Numerical Data and Functional Relationships in Science and Technology", edited by O. Madelung, Landolt-Börnstein, New Series, Group III, Vol. 17, Part 6, Chap. 3, p. 247 (Springer-Verlag, Berlin, 1982)

113. Chris G. Van De Walle, Phys. Rev. B **39**, 1871 (1989)

Li, Tiesheng Ph. D. March, 1993 Electric and Computer Engineering

Optical Properties of $CdTe/Cd_{1-x}Zn_xTe$ Strained-Layer Single Quantum Wells (140pp.)

Director of Dissertation: Henryk J. Lozykowski

In this dssertation,the electronic states in a series of molecular-beam-epitaxy-grown $CdTe/Cd_{1-x}Zn_xTe$ strained-layer single quantum wells are studied both theoretically and experimentally. The confined states were calculated using the three-band envelope function model taking into account the strain effect. Calculation based on model solid theory and deformation potential theory shows that, at Zn concentration of 0.21 in the barriers, the band lineup is type I for heavy holes and type II for light holes. An interpolation scheme is developed for the parameters in ternary semiconductors. In this scheme, not only the band gap bowing effect but also the nonlinearity of each individual band as a function of composition x is considered. Based on the quasi cubic model description of the Γ-point band structure of zinc-blend and wurtzite structure materials, a relation between the valence band edges in these two different structures (but same compound) is given. An iteration relation derived from Robinson rotation and the minimum strain energy principle was used to calculate the elastic constant tensor of zinc-blend structure material from the known elastic constant tensor of same compound in wurtzite structure. Photoluminescence measurement at temperatures between 9.0 and 100.0 K indicates that the broadening mechanism is dominated by the polar optical phonon (longitudinal optical) interactions. The circularly polarized excitation spectra show predominant heavy hole feature conforming that the band lineup is type I for heavy holes and type II for light holes. With well width between 25 and 75Å, this study shows that exciton binding energy decrease with increasing well width.